

# Unsteady fluid dynamics around a hovering flat plate wing

THÈSE N° 8055 (2017)

PRÉSENTÉE LE 20 OCTOBRE 2017

À LA FACULTÉ DES SCIENCES ET TECHNIQUES DE L'INGÉNIEUR  
LABORATOIRE DE DIAGNOSTIC DES ÉCOULEMENTS INSTATIONNAIRES  
PROGRAMME DOCTORAL EN MÉCANIQUE

ÉCOLE POLYTECHNIQUE FÉDÉRALE DE LAUSANNE

POUR L'OBTENTION DU GRADE DE DOCTEUR ÈS SCIENCES

PAR

Swathi Badala KRISHNA

acceptée sur proposition du jury:

Prof. F. Gallaire, président du jury  
Prof. K. A. J. Mulleners, Dr M. A. Green, directrices de thèse  
Prof. A. Dillmann, rapporteur  
Prof. F. Noca, rapporteur  
Dr M. Farhat, rapporteur



ÉCOLE POLYTECHNIQUE  
FÉDÉRALE DE LAUSANNE

Suisse  
2017



"What if I fall?  
Oh, but my darling  
What if you fly?"  
– Erin Hanson





# Acknowledgements

This work was conducted in 3 countries, spread over 2 continents. While in the past, I felt that I lost out on stability, I have come to realize that I have gained so much more. I cannot imagine having gotten this far or go further without acknowledging these individuals who played a part in getting me to the finish line.

I would like to thank Karen for taking me in as her first graduate student and for letting me choose my research question. I enjoyed setting up the lab and the first experiments. I sincerely thank Melissa for giving me the opportunity to be a part of her group and for taking on the role of my thesis co-director. I have learnt a great deal from Karen's detail oriented approach combined with Melissa's big picture approach and will strive to strike a balance between the two in the future as well. I am grateful for all the opportunities and guidance over the years that has helped me complete this work and made it a memorable journey.

Thanks to everyone in Green fluids lab (2015-16) for all the engaging discussions on bio-inspired flow experiments and vortex detection methods. It taught me different ways to approach and solve problems. I deeply appreciate all the help during my stay and making Syracuse fun as well. Also, a big shout out to the undergrads at LUH and EPFL who were part of the lab. I enjoyed working with them and learnt a lot by partaking in their projects.

I am extremely grateful to have had the opportunity to walk a few miles in this journey together with the following people.

Esra, for all the great times in the lab and outside. The long hours were never tiring with her around.

Torben and Matt Melius, for being the brightest silver lining around Hannover's clouds.

Matt Rockwood, for the weekly 'Monday at 9 a.m?' that made my life monumentally easier in Syracuse. His kindness, patience, and input on life and research will never be forgotten.

Angie, for the discussions on vortex dynamics methods and for all that we explored together.

Richard, for life and chess strategies.

Outi, for showing me the importance of setting multiple objectives, for the French abstract, and for being such a powerful cheerleader during stressful times.

Guillaume, for being my sounding board, and for the benevolent perspective on Rimsky, Spil, *et al.* He deserves the title of 'Best officemate ever!'

Robert, for driving in a new outlook on research and engineering. His enthusiastic spirit in the

## Acknowledgements

---

office was a fresh breath of air.

Anouk, for the monthly 'wandern' and discussions on aerodynamics ever since Delft.

Raj, for music, discussions, and that one dinner invitation.

Anil and Ajay for being my family away from home, and helping me stand up when I fell.

Snigdha, Supriya, Vignesh, and the Sleaters for being the constants in a sea of variables.

Most importantly, my parents and grandmother deserve my utmost gratitude for giving me the choice and chance at every stage in life, something that continues to be a distant dream for millions of girls in India and around the world. So far, I have lead a life far adventurous and gratifying than imagined, and it is because of their support and sacrifices. I dedicate this work to them.

*Lausanne, 26 September 2017*

S. K.

# Abstract

Insect flight is characterised by complex time-dependent flows in response to the unsteady wing movements. Biological fliers exploit the unsteady flow fields to modulate aerodynamic forces, thereby displaying unmatched flight performance, especially in hover. Naturally, this has inspired the creation of engineering models to replicate the flight behaviour. An in-depth understanding of the flow fields generated during hover and their dependence on the kinematics is paramount to achieve this goal.

The two main kinematic components of a hovering wing are the stroke, which refers to the back-and-forth motion, and wing rotation, which refers to the change in angle of attack. The phase relation between stroke and rotation is quantified in terms of phase-shift and is broadly classified into symmetric, advanced, and delayed rotation. The phase-shift and duration of rotation, together referred to as rotational timing, are investigated in this bio-inspired study. The objective is to characterise the effect of rotational timing on the aerodynamic forces and the flow fields generated by a hovering wing.

The unsteady flow around a hovering flat plate wing that mimics hoverfly kinematics has been investigated experimentally using particle image velocimetry and direct force measurements. The measurements are conducted at a Reynolds number of  $Re = 220$  and a reduced frequency of  $k = 0.32$  in order to dynamically match a hoverfly. The Lagrangian finite-time Lyapunov exponent method is used to analyse the unsteady flow fields by identifying dynamically relevant flow features such as the primary leading edge vortex (LEV), secondary vortices, and topological saddles, and their evolution within a flapping cycle.

Firstly, the flow and force behaviour was characterised for a typical flapping cycle. The flow evolution in a symmetric, fast rotation is divided into four stages that are characterised by the LEV emergence, growth, lift-off, and breakdown and decay. Tracking saddle points is shown to be helpful in defining the LEV lift-off which occurs at the maximum stroke velocity. The flow fields are correlated with the aerodynamic forces revealing that the maximum lift and drag are observed just before LEV lift-off, which corresponds to the maximum stroke velocity.

Secondly, the effect of phase-shift on the formation and evolution of lift-enhancing flow structures are discussed. Two advanced and delayed rotations are compared. The flow development stages and forces are similar for all rotations but the timing of stages varies. The evolution of forces and flow strongly depend on the stroke velocity.

Thirdly, the dependence of the flow and force evolution on the stroke velocity was substantiated by doubling the rotational duration in the symmetric rotation. It was found that the timing of the flow stages altered, whereas the flow and forces mostly evolved similarly to that of

## **Abstract**

---

a fast rotation. The fast rotation, however, produces higher maximum lift and drag compared to the slow rotation.

Lastly, the effect of phase-shift on the aerodynamic characteristics of a slow rotation is further explored. The slow rotation cases exhibit distinct flow patterns for varying phase-shifts unlike the fast rotations, in terms of the formation, evolution and breakdown of the flow structures as well as the timing. The forces also show distinct trends for varying phase-shifts and strongly depend on the angle of attack along with the stroke velocity in the slow rotations.

Key words: Hover, unsteady, wing rotation, aerodynamic forces, Lagrangian saddles, FTLE, PIV

# Résumé

Le vol des insectes est caractérisé par des écoulements complexes et dépendants du temps en réponse aux mouvements d'ailes. Les animaux aériens exploitent les champs d'écoulements instables pour moduler les forces aérodynamiques, atteignant ainsi une performance de vol incomparable, surtout en vol stationnaire. Naturellement, ceci a inspiré la création de modèles d'ingénierie pour répliquer leur comportement de vol. Une compréhension approfondie des champs d'écoulements générés pendant le vol stationnaire et de leur dépendance vis-à-vis de la cinématique est primordiale pour atteindre cet objectif.

Les deux principales composantes cinétiques du vol stationnaire sont le battement (mouvement de va-et-vient) et la rotation de l'aile (changement de l'angle d'attaque). La phase entre le battement et la rotation, ainsi que la durée de la rotation sont examinés dans cette étude bio-inspirée. L'objectif est de caractériser l'effet du déphasage entre le battement et la rotation sur les forces aérodynamiques et sur l'écoulement générés par une aile en vol stationnaire.

L'écoulement instable autour d'une plaque imitant la cinématique du vol stationnaire a été étudié expérimentalement en utilisant la vélocimétrie par images de particules et des mesures de forces directes. Les mesures sont effectuées à un nombre de Reynolds de  $Re = 220$  et à une fréquence réduite de  $k = 0.32$  afin de correspondre dynamiquement au vol stationnaire. La méthode Lagrangienne de l'exposant de Lyapunov à temps fini est utilisée pour analyser les écoulements instables en identifiant les caractéristiques de l'écoulement dynamiquement pertinents, tel que le principal tourbillon du bord d'attaque (LEV), les tourbillons secondaires, les selles topologiques et leur évolution au cours d'un cycle de battement.

Tout d'abord, les comportements de l'écoulement et des forces ont été caractérisés pour un cycle de battement typique. L'évolution des écoulements lors d'une rotation symétrique avec une durée de rotation courte est divisée en quatre étapes qui sont caractérisées par l'apparition du LEV, sa croissance, sa séparation, et sa rupture et décadence. Le suivi des points de selle s'avère utile pour définir la séparation du LEV qui a lieu à la vitesse maximale du battement. L'écoulement est corrélé avec les forces aérodynamiques en révélant que la portance et la trainée maximales sont observées juste avant la séparation du LEV, ce qui correspond à la vitesse maximale du battement.

Deuxièmement, l'effet du déphasage entre les deux mouvements de l'aile, le battement et la rotation, sur la formation et l'évolution des structures de l'écoulement renforçant la portance est discuté. Deux rotations avancées et retardées avec une durée de rotation courte sont comparées. Les étapes du développement de l'écoulement et les forces sont similaires pour toutes les rotations mais leur apparition dans le temps varie. L'évolution des forces et de

## Résumé

---

l'écoulement dépend fortement de la vitesse du battement.

Troisièmement, la dépendance de l'évolution de l'écoulement et des forces sur la vitesse de battement a été établie en doublant la durée rotationnelle de la rotation symétrique. Il s'est avéré que l'apparition des étapes de l'écoulement dans le temps changeait, tandis que l'écoulement et les forces évoluaient généralement d'une manière similaire au cas de rotation rapide. La rotation rapide, cependant, produit une portance et trainée maximales plus élevées par rapport à la rotation lente.

Enfin, l'effet du déphasage sur les caractéristiques aérodynamiques de la rotation lente est exploré plus en détail. Les cas de rotation lente présentent des schémas d'écoulement distinctifs pour des déphasages variables, contrairement aux rotations rapides en termes de formation, évolution et rupture des structures de l'écoulement, ainsi que leur apparition dans le temps. Les forces présentent également des tendances distinctives pour un déphasage variable. Les forces dépendent de l'angle d'attaque ainsi que de la vitesse du battement dans les cas de rotation lente.

Mots clefs : vol stationnaire, instable, rotation d'aile, forces aérodynamiques, selles Lagrangiennes, FTLE, PIV

# Contents

<b>Acknowledgements</b>	<b>v</b>
<b>Abstract</b>	<b>vii</b>
<b>Résumé</b>	<b>ix</b>
<b>Contents</b>	<b>xi</b>
<b>List of figures</b>	<b>xiii</b>
<b>List of tables</b>	<b>xxi</b>
<b>1 Introduction</b>	<b>1</b>
1.1 Flapping flight: Background . . . . .	1
1.2 Hovering kinematics . . . . .	3
1.3 Force production and flow physics in hovering flight . . . . .	5
1.4 Vortex identification methods . . . . .	8
1.5 Objectives, approach, and overview . . . . .	9
<b>2 Experimental set-up and analysis</b>	<b>11</b>
2.1 Experimental set-up . . . . .	11
2.1.1 The mechanical flapper . . . . .	11
2.1.2 Particle image velocimetry (PIV) . . . . .	13
2.1.3 Wing kinematics . . . . .	15
2.2 Flowfield analysis . . . . .	18
2.2.1 Eulerian criteria . . . . .	19
2.2.2 Lagrangian analysis . . . . .	21
<b>3 Results and discussions</b>	<b>25</b>
3.1 Roadmap . . . . .	25
3.2 Flow development stages for a symmetric flapping cycle . . . . .	27
3.2.1 LEV emergence . . . . .	28
3.2.2 LEV growth . . . . .	30
3.2.3 LEV lift-off . . . . .	33
3.2.4 LEV breakdown and decay . . . . .	35

## Contents

---

3.2.5	Influence of flow development on forces . . . . .	36
3.3	Influence of rotational phase for fast wing rotation . . . . .	39
3.3.1	Advanced rotation . . . . .	40
3.3.2	Delayed rotation . . . . .	49
3.3.3	Forces during the fast wing rotation . . . . .	57
3.3.4	Summary . . . . .	62
3.4	Influence of rotational timing for slow wing rotation . . . . .	64
3.4.1	Effect of rotational duration for symmetric rotation . . . . .	64
3.4.2	Advanced rotation . . . . .	71
3.4.3	Delayed rotation . . . . .	77
3.4.4	Summary of flow stages in slow rotation . . . . .	83
3.4.5	Circulation . . . . .	87
3.4.6	Effect of rotational timing on the aerodynamic forces . . . . .	90
<b>4</b>	<b>Summary and conclusions</b>	<b>101</b>
4.1	Flow and force characterisation of a flapping cycle . . . . .	102
4.2	Effect of rotational phase on the flow and forces . . . . .	102
4.3	Effect of rotational duration on the flapping cycle . . . . .	103
4.4	Effect of rotational phase during slow wing rotation . . . . .	103
4.5	Potential applications . . . . .	105
<b>A</b>	<b>Force rotation matrix</b>	<b>107</b>
<b>B</b>	<b>Circulation sensitivity analysis</b>	<b>111</b>
	<b>Bibliography</b>	<b>113</b>
	<b>Curriculum Vitae</b>	<b>121</b>



# List of Figures

1.1	Examples of insect like aerial vehicles. (a)Robobee from Harvard university (b) Delfly from Delft University of Technology . . . . .	2
1.2	Flapping wing trajectory (red) of a tethered fruit fly on a horizontal stroke plane ( <i>Drosophila melanogaster</i> ). The black lines indicate the wing. WH refers to the wing hinge point on the insect body. COG refers to the center of body mass. Adapted from Pick et al. [48]. . . . .	3
1.3	General schematic representation of the wing rotation cases for a half-cycle. Wing is represented by the black bars and the circles represent the leading edge . . . . .	4
2.1	A schematic of the wing mechanism. The inlay shows a zoomed in section of the wing apparatus with the three axes of motion. $\phi$ is the position on the stroke plane and $\beta$ is the rotational angle. The axis of rotation is marked by the dashed line on the wing at a distance of $c_{pa}$ from the leading edge. $c$ is the chord length, $R$ is the wing span. . . . .	12
2.2	Schematic of the experimental set-up . . . . .	14
2.3	Triggering mechanism and image acquisition . . . . .	16
2.4	Conceptual representation of the variations in the wing kinematics. The grey area indicates the duration of wing rotation in the flapping cycle. For a single stroke cycle, $t_s$ refers to the start of rotation in the symmetric case, $t_{adv}$ refers to the start of rotation in the advanced rotation case, and $t_{del}$ refers to the start of rotation in the delayed rotation case. In each of these cases, the duration of wing rotation is $T_f = T/3$ in every half-stroke with $T = 4s$ . $\Delta t_s$ refers to the phase shift for advanced and delayed rotation respectively. . . . .	17
2.5	A schematic of Lagrangian calculation. Fluid close to the boundary is stretched alongside the attracting material line (nFTLE ridge) whereas fluid is guided in opposite direction by the repelling material line (pFTLE ridge). Modified from Sadlo et al.[68] . . . . .	22
2.6	Schematic representation of the time intervals between the recorded images in the stroke. The blue dots on the sinusoidal profile indicate the time instants at which the images were recorded. The schematic on the right shows a difference in the time intervals ( $\Delta t_1, \Delta t_2, \dots, \Delta t_n$ ) between consecutive $n$ number of images ( $im_1, im_2, \dots, im_n$ ). . . . .	22

## List of Figures

---

2.7	Various vortex detection methods applied on the current data set. The images show the flow field around the wing at $t/T = 0.73$ of the flapping cycle. . . . .	23
3.1	Characteristic flow development in a typical flapping cycle as the wing (black lines with circles that represent the leading edge) moves to the left. The illustration of the features is based on vorticity. Blue features are indicative of the leading edge vortex and orange are indicative of the trailing edge vortex. . . . .	27
3.2	Flow fields showing the LEV emergence process. Top right: Stroke position (—) and stroke velocity (---) of the half-stroke with the corresponding time instants. . . . .	28
3.3	Example of the chord normal distance ( $h/c$ ) of the outermost point of the LEV. The <b>nFTLE</b> ridges represent the attracting material lines that indicate the boundary of the flow structure and the <b>pFTLE</b> ridges represent the repelling material lines along which flow diverges. . . . .	29
3.4	Chord-normal distance of the outer LEV boundary indicated by the <b>nFTLE</b> ridge (figure 3.3). The gray region indicates the period of wing rotation. The vertical dotted lines denote the stages in the flow development which are represented by the sketches corresponding to LEV ① emergence, ② growth, ③ lift-off, and ④ breakdown(L-R). The top $x$ -axis denotes the convective time scale ( $t^* = U^* t/c$ ). . . . .	29
3.5	Flow fields showing the growth of the bound LEV. <b>nFTLE</b> and <b>pFTLE</b> ridges are overlayed on phase-averaged vorticity fields. The full saddle is indicated by $\oplus$ , and the half-saddle is indicated by $\triangle$ . Top right: Kinematics (gray bars indicate period of rotation in the cycle). . . . .	31
3.6	LEV binding phenomenon during pure translation. The sketch is based on the <b>nFTLE</b> and <b>pFTLE</b> ridges. . . . .	31
3.7	Distance of the full saddle ( $\oplus$ ), half saddle ( $\triangle$ ) from the axis of rotation; LEV circulation ( $\square$ ) during the half-stroke. The gray region indicates the period of wing rotation. Top $x$ -axis shows the convective time scale ( $t^*$ ). The vertical dotted lines separate the LEV ① emergence, ② growth, ③ lift-off, and ④ breakdown stages (L-R). . . . .	32
3.8	Vorticity flux near the leading edge ( $\square$ ) and trailing edge ( $\square$ ). Schematic of the leading and trailing edge line boundaries to calculate the vorticity flux on top. . . . .	33
3.9	Flow fields showing the LEV lift-off. <b>nFTLE</b> and <b>pFTLE</b> ridges are overlayed on phase-averaged vorticity fields. Top right: Kinematics (Gray bars indicate period of rotation in the cycle). . . . .	34
3.10	Tangential velocity on the suction side of the wing through half-stroke. Black arrows represent the direction of flow for warm colors (LE to TE) and cold colors (TE to LE). Dotted lines represent the flow stages . . . . .	35
3.11	Flow fields showing the LEV breakdown process. <b>nFTLE</b> and <b>pFTLE</b> ridges are overlayed on phase-averaged vorticity fields. Top right: Kinematics (Gray bars indicate period of rotation in the cycle). . . . .	36

3.12 Flow fields showing the LEV decay process. <b>nFTLE</b> and <b>pFTLE</b> ridges are overlaid on phase-averaged vorticity fields. Top right: Kinematics (Gray bars indicate period of rotation in the cycle). . . . .	37
3.13 Lift (—■—) and drag (—■—) coefficients over a half-stroke. . . . .	37
3.14 The rotational position of the wing at the beginning of each half stroke at $t/T = 0$ in (a) fully advanced rotation (b) partly advanced rotation (c) symmetric rotation. The wing moves to the left. . . . .	40
3.15 Flow fields showing the end of LEV emergence stage for (a) fully advanced (b) partly advanced (c) symmetric rotations. Top right: Stroke position (—) and stroke velocity (---) of the half-stroke with the corresponding time instants. . . . .	41
3.16 Top row: Flow fields showing the LEV features near the end of the previous half-stroke when the wing begins to rotate. Bottom row: Flow fields showing the LEV features at the end of the previous half-stroke. (a,d) fully advanced (b,d) partly advanced (c,f) symmetric rotations. Top right: Stroke position (—) and stroke velocity (---) of the half-stroke with the corresponding time instants. . . . .	42
3.17 Chord-normal height of the leading edge vortex for fully advanced (—■—), partly advanced (—■—), and symmetric rotation(—■—). Top x-axis shows the convective time scale ( $t^*$ ). . . . .	43
3.18 LEV circulation for fully advanced (—■—), partly advanced (—■—), and symmetric (—■—) rotations. Top x-axis shows the convective time scale ( $t^*$ ). . . . .	43
3.19 Vorticity flux for fully advanced —■—, partly advanced —■—, and symmetric —■— rotations . . . . .	44
3.20 Top row: Saddle distance evolution for (a) fully advanced (b) partly advanced (c) symmetric rotations, including stroke velocity (---). Gray areas indicate rotation. Corresponding flow fields at time instants when, row 1: saddles merge, row 2: saddle, thereby LEV lifts-off, row 3: End of LEV lift-off stage. . . . .	45
3.21 Tangential velocity on the suction side of the wing through half-stroke for (a) fully advanced, (b) partly advanced, and (c) symmetric rotations. Black arrows represent the direction of flow for warm colors (LE to TE) and cold colors (TE to LE). Dotted lines represent the end of flow stages. . . . .	47
3.22 Flow fields showing the LEV breakdown and decay stage for (a) fully advanced, (b) partly advanced, and (c) symmetric rotations. Top right: Stroke position (—) and stroke velocity (---) of the half-stroke with the corresponding time instants. . . . .	48
3.23 The rotational position of the wing at the beginning of the half-stroke at $t/T = 0$ in (a) fully delayed (b) partly delayed (c) symmetric rotations. . . . .	49
3.24 Flow fields showing LEV emergence stage for (a,d) fully delayed, (b,e) partly delayed, and (c,f) symmetric Top row: Start of LEV emergence stage. Bottom row: End of LEV emergence stage. Top right: Stroke position (—) and stroke velocity (---) of the half-stroke with the corresponding time instants. . . . .	50
3.25 Chord-normal height of the leading edge vortex for fully delayed (—■—), partly delayed (—■—) and symmetric (—■—) rotations. Top x-axis shows the convective time scale ( $t^*$ ). . . . .	51

## List of Figures

---

3.26 LEV circulation for fully delayed, $\text{---}\blacksquare\text{---}$ , partly delayed, $\text{---}\blacksquare\text{---}$ , and symmetric $\text{---}\square\text{---}$ rotations. Top x-axis shows the convective time scale ( $t^*$ ). . . . .	51
3.27 Vorticity flux for fully delayed $\text{---}\blacksquare\text{---}$ , partly delayed $\text{---}\blacksquare\text{---}$ , and symmetric $\text{---}\square\text{---}$ rotations. . . . .	52
3.28 Top row: Saddle distance evolution for (a) fully delayed (b) partly delayed (c) symmetric rotations, including stroke velocity ( $\text{---}$ ). Gray areas indicate rotation. Corresponding flow fields at time instants when, row 1: saddles merge, row 2: saddle, thereby LEV lifts-off, row 3: End of LEV lift-off stage. . . . .	53
3.29 Tangential velocity on the suction side of the wing through half-stroke for (a) fully delayed, (b) partly delayed, and (c) symmetric rotations. Black arrows represent the direction of flow for warm colors (LE to TE) and cold colors (TE to LE). . . . .	54
3.30 Flow fields showing the end of LEV break-up for (a) fully delayed rotation (b) partly delayed (c) symmetric rotation. Top right: Stroke position ( $\text{---}$ ) and stroke velocity ( $\text{---}$ ) of the half-stroke with the corresponding time instants. . . . .	54
3.31 Notable non-dimensional times during the life-cycle of the LEV for the fast wing rotation ( $T_f = T/6$ ). . . . .	55
3.32 Left: Rates of the full saddle movement for the fast wing rotation ( $T_f = T/6$ ). Right: Example demonstrating the three segments in the saddle curve with varying growth rate. . . . .	55
3.33 Lift evolution in half-stroke for representative variations of phase-shift $\Delta t_s$ , for the fast rotation. Fully advanced $\text{---}\blacksquare\text{---}$ , symmetric $\text{---}\square\text{---}$ , fully delayed $\text{---}\blacksquare\text{---}$ rotations. . . . .	57
3.34 Maximum (squares) and mean (stars) lift for variations in the phase-shifts for the fast rotation. The black bars on the top represent the angle of attack at the beginning of the half-stroke. . . . .	58
3.35 The time at which maximum lift occurs for the fast rotation in a stroke cycle. . . . .	58
3.36 Flow fields at maximum lift for (a) fully advanced (b) partly advanced (c) symmetric (d) partly delayed (e) fully delayed during a fast rotation. . . . .	59
3.37 Drag evolution in half-stroke for representative variations of phase-shift $\Delta t_s$ , for the fast rotation. Fully advanced $\text{---}\blacksquare\text{---}$ , symmetric $\text{---}\square\text{---}$ , fully delayed $\text{---}\blacksquare\text{---}$ rotations. . . . .	60
3.38 Maximum (squares) and mean (stars) drag variations in the phase-shift for the fast rotation. The black bars on the top represent the angle of attack at the beginning of the half-stroke. . . . .	60
3.39 The time at which maximum drag occurs for the fast rotation in a half-stroke. . . . .	61
3.40 Characteristic flow development in a flapping cycle with advanced, fast wing rotation. The wing moves to the left. The illustration of the features are based on vorticity. Blue features are indicative of the LEV and orange are indicative of the TEV. . . . .	62
3.41 Characteristic flow development in a flapping cycle with delayed, fast wing rotation. The wing moves to the left. The illustration of the features are based on vorticity. Blue features are indicative of the LEV and orange are indicative of the TEV. . . . .	63

3.42	Flow fields at crucial stages in symmetric rotation Top row: Fast flip ( $T_f = T/6$ ). Bottom row: Slow flip ( $T_f = T/3$ ). Column 1: End of LEV emergence, Column 2: End of LEV growth, Column 3: End of LEV lift-off. Top right: Stroke position (—) and stroke velocity (---) of the half-stroke with the corresponding time instants. Gray area indicate period of rotation for fast and slow rotation. . . . .	65
3.43	LEV binding phenomenon during pure translation for the slow rotation. The sketch is based on the <b>nFTLE</b> and <b>pFTLE</b> ridges. . . . .	66
3.44	Tangential velocity on the suction side of the wing through half-stroke. Left: Slow rotation ( $T_f = T/3$ ). Right: Fast rotation ( $T_f = T/6$ ). Black arrows represent the direction of flow for warm colors (LE to TE) and cold colors (TE to LE). . . .	67
3.45	Chord-normal height of the leading edge vortex for symmetric rotation for slow flip (—○—) in comparison with fast flip duration (—□—). Top x-axis shows the convective time scale ( $t^*$ ). . . . .	67
3.46	Full saddle distance (—●—) and half-saddle distance(—▲—) for slow rotation. The saddles in gray denote that of the fast flip. Top x-axis shows the convective time scale ( $t^*$ ). The vertical dotted lines separate the LEV ① emergence, ② growth, ③ lift-off, and ④ breakdown and decay stages of the slow flip. . . . .	68
3.47	Notable non-dimensional times during the life-cycle of the LEV for the symmetric wing rotation with fast and slow rotations. . . . .	68
3.48	Force coefficients for symmetric rotation. Colored symbols represent the slow rotation Row 1: Kinematics for fast and slow rotation. Gray area indicates the period of rotation. Row 2: Lift coefficients for slow rotation (—■—) compared to lift coefficients from fast rotation (—). Row 3: Drag coefficients for slow rotation (—■—) compared to drag coefficients from fast rotation (—) . . . . .	70
3.49	The rotational angle of the wing at the beginning of each half stroke in (a) fully advanced (b) partly advanced (c) least advanced (d) symmetric rotations. The wing moves to the left. . . . .	71
3.50	Flow evolution in fully advanced, slow rotation. Top right: Corresponding time instants at which flow fields are shown. . . . .	72
3.51	Vorticity flux near the leading edge (—●—) and trailing edge (—○—). . . . .	74
3.52	Chord-normal height of the LEV for fully advanced (—●—), partly advanced (—○—), least advanced (—○—) and symmetric rotations (—○—). The dotted lines mark the end of flow development stages in the advanced rotations. Top x-axis shows the convective time scale ( $t^*$ ). . . . .	75
3.53	LEV circulation for fully advanced —●—, partly advanced —○—, least advanced —○—, symmetric —○— rotations. The dotted lines mark the end of flow development stages in the advanced rotations. Top x-axis shows the convective time scale ( $t^*$ ). . . . .	75
3.54	The rotational position of the wing at the beginning of each half stroke in (a) fully delayed (b) partly delayed(c) least delayed (d) symmetric rotations. The wing moves to the left. . . . .	77
3.55	Flow evolution in fully delayed, slow rotation. Top right: Corresponding time instants at which flow fields are shown. . . . .	78

## List of Figures

---

3.56 LEV emergence in the delayed rotation of slow flip. Sketch based on <b>nFTLE</b> ridge. The features are indicative of the remnant LEV through which the wing moves.	79
3.57 LEV growth in the fully delayed, slow rotation. Sketch based on <b>nFTLE</b> and <b>pFTLE</b> ridges. The features are mainly indicative of the LEV.	80
3.58 LEV circulation for fully delayed $\text{---}\bullet\text{---}$ , partly delayed $\text{---}\bullet\text{---}$ , least delayed $\text{---}\circ\text{---}$ , symmetric $\text{---}\circ\text{---}$ rotations. The dotted lines mark the end of flow development stages in the delayed rotations. Top x-axis shows the convective time scale ( $t^*$ ).	81
3.59 Vorticity flux at the leading edge for fully advanced ( $\text{---}\bullet\text{---}$ ), fully delayed ( $\text{---}\bullet\text{---}$ ) and symmetric rotation ( $\text{---}\circ\text{---}$ ).	81
3.60 Characteristic flow development in a flapping cycle with advanced, slow wing rotation. The wing moves to the left. The illustration of the features are based on vorticity. Blue features are indicative of the LEV and orange are indicative of the TEV.	83
3.61 Characteristic flow development in a flapping cycle with delayed, slow wing rotation. The wing moves to the left. The illustration of the features are based on vorticity. Blue features are indicative of the LEV and orange are indicative of the TEV.	84
3.62 Tagential velocity plots for (a) fully advanced , (b) partly advanced (c) least advanced (d) symmetric (e) least delayed, (f) partly delayed (g) fully delayed rotations. Warm colors signify a downward velocity along the chord (LE to TE) and cold colors signify upward velocity (TE to LE).	85
3.63 Maximum LEV circulation (green) and maximum vorticity (purple) at the same time instant as maximum circulation for variations in the phase-shift for slow rotation. The black bars on the top represent the angle of attack at the beginning of the half-stroke.	87
3.64 Flow fields at maximum circulation for (a) fully advanced (b) partly advanced (c) least advanced (d) symmetric (e) least delayed (f) partly delayed (g) fully delayed rotations during slow rotation	88
3.65 Lift evolution in half-stroke for all variations of phase-shift $\Delta t_s$ , for the slow flip duration. Fully advanced $\text{---}\bullet\text{---}$ , Symmetric $\text{---}\circ\text{---}$ , fully delayed $\text{---}\bullet\text{---}$ rotations	90
3.66 Drag evolution in half-stroke for representative variations of phase-shift $\Delta t_s$ , for the slow flip duration. Fully advanced $\text{---}\bullet\text{---}$ , Symmetric $\text{---}\circ\text{---}$ , fully delayed $\text{---}\bullet\text{---}$ rotations	91
3.67 Maximum lift (circles) and mean lift (stars) trends for variations in the phase-shift for the slow rotation. The black bars on the top represent the angle of attack at the beginning of the half-stroke.	91
3.68 The time at which maximum lift occurs for the slow rotation in a half-stroke.	92
3.69 Flow fields at maximum lift for (a) fully advanced (b) partly advanced (c) least advanced (d) symmetric (e) least delayed (f) partly delayed (g) fully delayed. The time instant in the flapping cycle ( $t/T$ ) for the given flow field is included in each panel.	93

3.70	Maximum drag (circles) and mean drag (stars) trends for variations in the phase-shift for the slow rotation. The black bars on the top represent the angle of attack at the beginning of the half-stroke. . . . .	95
3.71	The time at which maximum drag occurs for the slow rotation in a half-stroke. . . . .	96
3.72	Flow fields at maximum drag for (a) fully advanced (b) partly advanced (c) least advanced (d) symmetric (e) least delayed (f) partly delayed (g) fully delayed. The time instant in the flapping cycle represented by the flow field is included in each panel ( $t/T$ ). . . . .	97
3.73	The geometric angle of attack ( $\alpha^\circ$ ) at which maximum lift and maximum drag occurs for the slow rotation . . . . .	98
4.1	Schematic of differences in LEV evolution based on the nFTLE ridges during slow wing rotation . . . . .	104
4.2	General schematic representation of the wing rotation cases for a half-stroke. Maroon arrows indicate the magnitude and timing of the maximum lift in the half-stroke. Blue arrows indicate the magnitude and timing of the maximum drag coefficients for three representative cases. . . . .	105
A.1	Resolution of forces . . . . .	108
B.1	Circulation sensitivity analysis . . . . .	111





## List of Tables

2.1	Wing parameters . . . . .	12
2.2	Fluid mixture parameters . . . . .	13
2.3	Seeding particles properties . . . . .	14



# Nomenclature

$\alpha$	angle of attack, °
$\beta$	rotational angle with respect to the vertical, °
$\Gamma$	circulation, m <sup>2</sup> /s
$\lambda_{max}$	maximum matrix eigenvalue
$\phi$	stroke angle, °
$\dot{\phi}$	stroke velocity, m/s
$\dot{\phi}_{max}$	maximum stroke velocity, m/s
$\sigma_{t_1}$	coefficient of expansion
$\omega$	vorticity, 1/s
$c$	chord length, m
$C_l, C_d$	lift, drag coefficients
$f$	flapping frequency, Hz
$h$	chord normal distance, m
$k$	reduced frequency
$R$	wing span, m
$Re$	Reynolds number
$s$	saddle distance, m
$t$	physical time, s
$t^*$	convective time
$t_1$	integration time, s
$T$	time period of a flapping cycle, s
$T_f$	duration of rotation, s
$U^*$	flapping velocity, m/s
$u_\phi$	induced velocity due to stroke, m/s
$v_t$	tangential velocity, m/s
$(x, y)$	spatial coordinates, m
$\nabla$	gradient function



# 1 Introduction

## 1.1 Flapping flight: Background

How many times have you tried to shake off that bee hovering around you on a quiet, colorful spring afternoon and failed? Or try to grab those annoying mosquitoes that interrupt your sleep only to remain wide awake for the rest of the night? Or not be able to fend off a fruit fly trying to perch on a half-eaten apple?

The answer is most likely, too many.

Trying to surpass a masterpiece of intricate construction and immense aerial capabilities is no easy task. These and many other insects have survived and evolved for over 350 million years mainly due to their flight skills in comparison with the flightless insects. They have adapted and tuned their morphology and kinematics to match the dynamical properties of their surrounding air. Along with being able to pull off quick landings and take-off, the flying insects can maneuver in different directions very quickly, fly sideways and backwards too [56]. Thus, making them experts in predator evasion, securing food sources and finding new habitats. Apart from the pure evolutionary curiosity, the admirable aerial locomotion of insects has inspired the creation of engineering models. The idea of replicating these flight features in small, autonomous aircraft is alluring to many practical applications.

Research groups across the world have embarked on mimicking the flight performance of insects by creating miniature robots (figure 1.1). These flapping wing micro aerial vehicles (MAV) are designed and built in order to leverage their size, agility, ability to remain inconspicuous. From seemingly simple tasks such as finding a friend at a crowded concert to observing disaster areas, aiding medical workers in remote areas, forming communications networks, and spying in indoor spaces, these micromechanical devices are all set to be an integral part of the future. This requires a distinct flight envelope and precise flight control which primarily commands an accurate understanding of insect flight aerodynamics.

In early 20<sup>th</sup> century, the prevailing conventional steady-state aerodynamic theory was used to

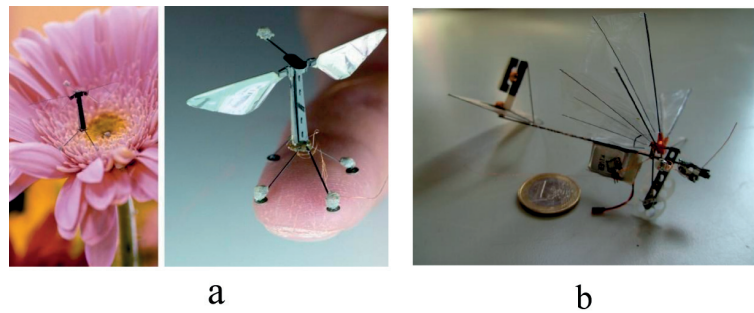


Figure 1.1 – Examples of insect like aerial vehicles. (a) Robobee from Harvard university (b) Delfly from Delft University of Technology

sensationally state that bumblebees cannot fly; unbeknownst to the bees. However, inferences from detailed optical and statistical data solved the now infamous 'bumblebee paradox'. It has been proven that the peculiar to-and-fro (flapping) motion of the wings seen in insects creates complex time-dependent flows, which is the primary reason for better performance than that observed in fixed wing scenarios. By utilising the additional circulation created by the flapping wing kinematics, the insects generate higher lift than during steady motion of the wing at the same velocities and angles of attack [87, 20, 21, 22, 23, 24, 25]. In addition to contributing to the lift required to keep the insect aloft, manipulation of the translational and rotational aerodynamic mechanisms may provide a potent means by which a flying animal can modulate direction and magnitude of flight forces for maneuvering flight control and steering behaviour [47]. The flapping motion is known to comprise a series of complex aerodynamic phenomena that is representative of most unsteady flows observed around helicopter rotors, wind turbines, turbine compressors etc. This intriguing unsteady nature of the flow around the insect wings continues to attract academic researchers who are inquisitive about the physics of the flow itself.

### Rotary wings vs. Flapping wings

Another approach to realise superior flight characteristics in man-made aerial vehicles has manifested in the form of rotary wing vehicles. One might wonder the purpose of studying flapping wings aerodynamics when commercially popular multi-rotor aerial robots are thriving, especially amongst hobbyists, primarily due to the ease of control. The multi-rotors with propellers are configured in a way to achieve flight characteristics like hover and aggressive flip maneuvers. The main disadvantage of the multi-rotor model is the continuous rotation of the actuators which causes high electrical spending, reducing the practical flight time[39]. Also, the high noise levels emitted by multi-rotor configurations are shown to elicit strong, adverse physiological responses[41]. Flapping wings are more beneficial for serious applications which requires small size, high efficiency, and less noise. Recently, studies using hawkmoth wings[91] and fruitfly wings[38] were compared in flapping and rotary configurations. The efficiency, which was taken as the lift to power ratio, for the rotary configuration was found to

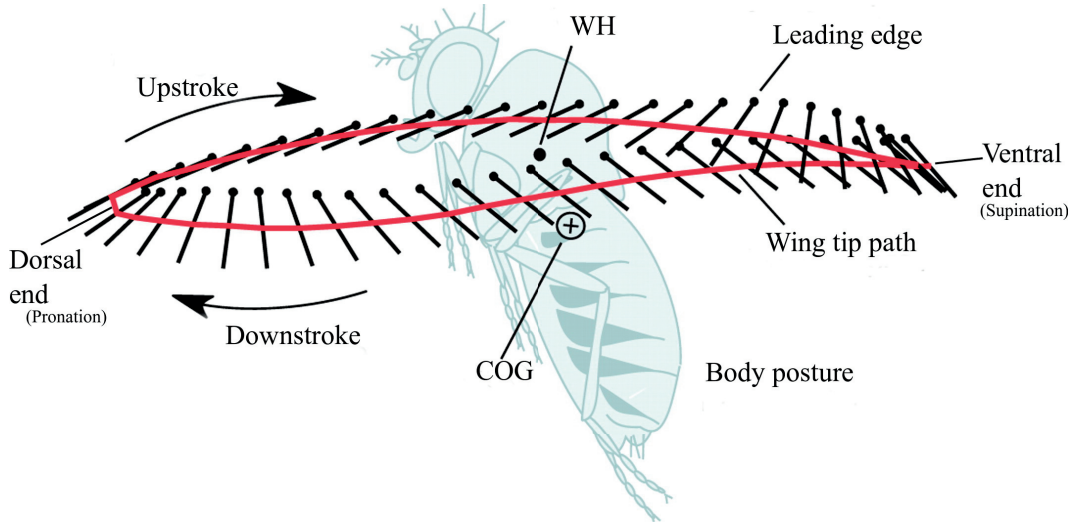


Figure 1.2 – Flapping wing trajectory (red) of a tethered fruit fly on a horizontal stroke plane (*Drosophila melanogaster*). The black lines indicate the wing. WH refers to the wing hinge point on the insect body. COG refers to the center of body mass. Adapted from Pick et al. [48].

be less than that of flapping wing configuration at low Reynolds number ( $\mathcal{O}(10^2)$ ). Published data for several types of MAV concepts were reviewed and compared with entomological fliers[53]. It was found that the rotory systems achieved higher values of efficiency than the existing biomimetic flapping wing systems, but were less efficient compared to the biological fliers. These studies suggest that the inherent potential of flapping wing configurations has not been fully exploited yet. In order to design control strategies to achieve autonomous flight characteristics such as hover or recuperating from control failure, it is first necessary to understand the flow behaviour over the flapping wings.

## 1.2 Hovering kinematics

One of the much coveted flight characteristics that is specific to insects and some birds, is being able to remain airborne at low or negligible air speeds, i.e. to perform hovering flight, which winged insects as a class (Pterygota) have mastered [87]. Hovering flight is a power-demanding act due to the fact that the insect body has no accumulated kinetic energy, relative to the undisturbed air. Hovering flight also sets the fundamental requirement of flapping flight without the complications resulting from forward body motion. The lift enhancing effect of the aerodynamic mechanisms during hover strongly depends on the kinematics of the flapping wing [16, 46, 85, 69].

The main kinematic features of a hovering wing are deviation, stroke, and rotation. The deviation or elevation, is found to have only a marginal effect on the mean lift and mean drag [9]. During hover, the wings produce lift only during the active back-and-forth motion of the wing which is referred to as the stroke. The plane in which the insect wing reciprocates is the

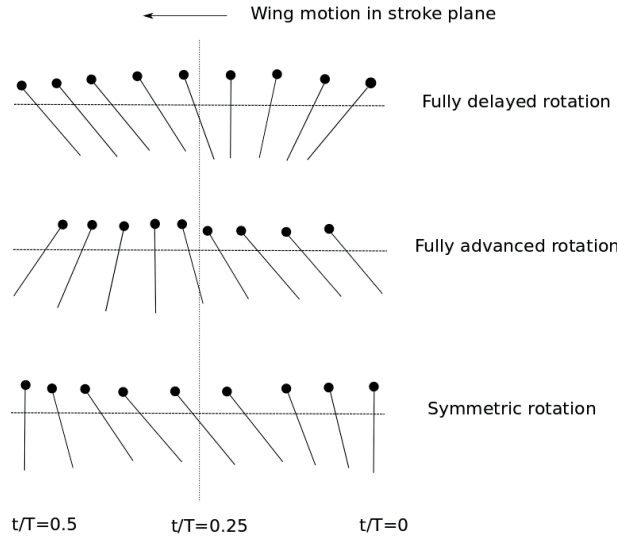


Figure 1.3 – General schematic representation of the wing rotation cases for a half-cycle. Wing is represented by the black bars and the circles represent the leading edge

stroke plane. Conventionally, the movement of the wing from the rearmost position (relative to the body) to its foremost position is called the downstroke, or alternatively front stroke. The return movement of the wing from the front to the back of the insect is referred to as the upstroke or back stroke. Wing motion in each direction with respect to the insect body is referred to as half-stroke. Two half-strokes constitute to a single flapping cycle.

High speed filming and photogrammatic reconstruction of the wing kinematics of real insects in hovering flight have revealed that during both down and upstroke, the angle of attack of the wing remains relatively constant for most of each half-stroke [51, 81]. At either end of the half-stroke, referred to as the stroke reversal, the wings reach a zero linear velocity and rotate about their wing hinge axis such that the pressure side becomes the suction side and the leading edge always leads. This movement constitutes to the rotational phase of the flapping cycle. The rotational phases themselves are referred to as pronation and supination at the dorsal and ventral end of the stroke respectively (figure 1.2). Pronation and supination are mainly confined to the periods of acceleration and decelerations at stroke-reversals and are approximately equal in duration [22]. The reciprocating motion is also generally referred to as the translational phase of the flapping cycle, because the linear motion of the wings dominates over changes in rotation (angle of attack) for a better part of the stroke. The wing rotation is crucial because it helps the wing maintain a positive angle of attack through out the flapping cycle which assists in lift generation in both half-strokes, thus helping the insect remain aloft.

The study of real insects have shown that the timing and duration of wing rotation are actively controlled during visually induced steering maneuvers and even change from one stroke to another [74]. Especially in tethered flights, the flies advanced or delayed wing rotations during a visually elicited turn. Such advancement or delay in the wing rotations are shown to produce a moment to turn the fly in the required direction. Wing rotation can be generally classified



into three categories depending upon the timing of rotation, i.e., the time at which the wing begins to rotate with respect to the wing translation in each half-stroke. In figure 1.3, a general representation of the wing rotation cases is depicted for a half-cycle. The wing are presented as black lines with a circle marking the leading edge. The orientation of the wing is presented for a half cycle starting at the right at the beginning of the cycle moving to the left. The relative inflow is from left to right. When half the wing rotation is conducted near the end of a stroke and half at the beginning of the next stroke, it is known as **symmetric rotation**. If most or all of the rotation occurs before stroke reversal, then the leading edge rotates backward relative to the stroke direction. This is referred to as **advanced rotation**. If most or all of the rotation occurs after the stroke reversal, then the leading edge of the wing rotates forward, relative to the stroke direction. This is referred to as the **delayed rotation**. The advanced and delayed rotations can be noted in the wing's starting angle of attack with respect to the direction of the wing stroke. Another parameter describing the kinematics of a hovering wing is the duration of wing rotation in each half-stroke. The duration and timing of the wing rotation, referred to as **rotational timing** in this work, is known to alter the rotational circulation which in turn affects the forces [16]. However, the coupling of force with the in-depth analysis of the flow fields calls for more attention. Understanding the influence of the rotational timing on the vortex dynamics and the resulting force production could especially be useful in the design of high performance flow control surfaces.

Two distinct styles of hovering are found in nature: ① normal hovering, in which insects employ a symmetric back and forth motion on a horizontal stroke plane, and ② inclined hovering in which insects like dragonflies [57] employ asymmetric movements on an inclined plane [88]. In inclined hovering, the upstroke generates lower lift compared to the downstroke making it less efficient, whereas in normal hovering the downstroke and upstroke are approximately symmetrical and generate similar forces [86]. As with most sophisticated aerialists found in nature such as flies, bees and hummingbirds, this thesis concerns itself only with normal hovering. Known to be one of the best hovering animals, the hoverflies employ a non-linear stroke velocity [81, 83]. The hoverfly kinematics has inspired the current work. It is imperative to study the effect of a varying stroke velocity on the vortex dynamics and the aerodynamic forces.

### 1.3 Force production and flow physics in hovering flight

Early attempts to explain force production in insect flight relied on the quasi-steady state approach, where time dependent characteristics of force generation were ignored [77, 88]. A decade later, a comprehensive review by Ellington [20] showed that the lift generated by the quasi-steady state theory are lower than the measured values in real insects. Further works highlighted the limitations of the quasi-steady approach following Ellington's approach [27, 18]. In the mean time, with advancement of flow visualisation and force measurement techniques, experimental investigations of flapping flight alongside theoretical works came to light [3, 52, 71]. The time-dependent forces generated due to the unsteady behaviour was

studied on zoological specimens and simplified robotic models, which contributed to a deeper understanding of the mechanisms that collectively answer for advanced aerodynamic performance of hovering insect wings. Notably, the clap and fling [88], dynamic stall [26], rotational lift [16], and wake capture [17, 16] were found to be the driving force behind insect flight. A broad overview of the unsteady mechanisms and their dependency on wing kinematics can be found in the comprehensive review by Shyy et al.[73].

Several experimental [17, 26, 6, 2] and computational [50, 82, 62] studies evaluated the aerodynamic forces and flow structures around a flapping wing. Specifically, the effect of wing rotation has been investigated extensively in terms of the forces produced [16, 69, 1]. It was experimentally observed that four important parameters of stroke reversal influence the generation of the force during the subsequent stroke, namely, the position of the rotational axis, the speed of rotation, the angle of attack of the preceding stroke and the length of the preceding stroke [15]. In the same work, it was also shown that for the same reduced frequency, a change in the Reynolds number showed minor differences in the flows visualised.

This was followed by an extensive investigation of the forces around a robotic insect wing that was modeled after a fruit-fly by Dickinson's group and collaborators [16, 69, 5, 1]. The characteristic hover kinematics used in a majority of the experiments has been a linear stroke profile and a trapezoidal profile for wing rotation. It was shown that the flight forces can be controlled by altering the timing of wing rotation, flapping frequency and amplitude of stroke and that the stroke deviation lowered aerodynamic performance relative to no deviation case [69]. The stroke motion with constant velocity was characterised by large peaks in the lift when the wing rapidly accelerated or decelerated in the stroke plane near the stroke reversals. It was theorised that the two peaks were caused by rotational circulation and wake capture. The large positive transient seen in the lift soon after the start of each half-stroke was attributed to the shed vorticity from the previous half-cycle. The wake from one half-cycle can increase the effective fluid velocity at the start of the next stroke and thereby increase force production more than that produced during translational phase. Whereas the wake at the end of each half-stroke, was attributed to the rotational circulation where the wing's own rotation serves as a source of circulation to generate an upward force. It was reported that considerable lift can be generated if the wing rotation precedes stroke reversal as opposed to wing rotation following stroke reversal [70, 75]. Of the different wing rotations, the symmetric rotation showed a mean lift coefficient which was 80% higher than the quasi-steady value. The symmetric rotation produced lower lift than the advanced rotation but higher than the delayed rotation. By changing the timing and duration of the wing rotation, referred to as rotational timing in this study, desired lift coefficients can be produced [70, 80, 75, 4]. Though the forces in different wing rotation were discussed extensively, an in depth analysis of the temporal development of the flow was not provided.

The two-dimensional mechanism in hovering was investigated computationally among others by Wang [82]. In case of hovering, the increase in force production close to the stroke reversal was accompanied by the enlargement of the LEV as the wing begins to supinate prior to stroke

### 1.3. Force production and flow physics in hovering flight

---

reversal, and a starting vortex due to rotation, agreeing with previous experimental study by Dickinson [16]. At stroke reversal, both the LEV and a rotational starting vortex are shed into the wake forming a counter-rotating pair that directs a jet of fluid towards the pressure side of the wing at the start of the next stroke [5, 82].

2D computations and 3D robotic experiments were compared for different kinematic patterns to study the unsteady effects [84]. It was found that the forces are sensitive to the phase between stroke angle and angle of attack. The computed lift in 2D agreed with measurements in the symmetric and advanced rotations whereas lags behind the 3D lift in the delayed rotation. A main difference found between a revolving wing and translating wing was the absence of vortex shedding by a revolving wing over a distance much longer than the length of the stroke.

The reason for the higher lift performance of flapping motion with respect to the steady fixed wing alternative is largely attributed to the prolonged attachment of the leading-edge vortex (LEV) during the majority of each half-stroke [26]. The dynamic stall vortex that forms over the suction side of the wing dominates the flapping cycle and has been proven to enhance lift [26, 17, 16]. As the insect flaps its wing, it creates an effective unsteady change in the angle of attack of the wing in the air yielding a large region of circulation on the suction side of the wing. This creates a pressure dip on the suction side of the wing which leads to a sustained lift production. Except for very low Reynolds numbers ( $Re < 100$ ), the LEV was found to be a sufficient high-lift mechanism for sustained flight in insects [75]. The evident axial flow observed in the LEV's core at  $Re$  of  $\mathcal{O}(10^3)$  is absent at a lower  $Re$  of  $\mathcal{O}(10^2)$ , which makes the flow in this regime largely two-dimensional [6].

It is widely accepted and representative to use flat plates as a simplified substitutes for the study of unsteady flows of similar regimes that are found in a wide range of flying and swimming animals [11, 34, 45, 42]. For the experimental study of flapping flight as well as pitching [10], plunging [63] and rotating plates [58], particle image velocimetry as well as flow visualisation techniques have been extensively employed [7, 13, 79]. The flow structures surrounding a wing moving in a fluid with simplified kinematics has been presented through 2D and more recently 3D quantitative flow fields [43, 59]. In particular, pitching maneuvers over a range of reduced frequencies and pivot point locations were studied by Granlund et al [31]. They were able to correlate lift and drag coefficients as functions of both angle of attack and pivot point location for reduced frequencies greater than 0.1. It was shown that for slower change in the pitch, stall is delayed beyond the steady incidence angle. For higher rates, the LEV also depended on the pivot points.

The LEV circulation growth was expressed as a function of convective time scales for vortex rings and expressed as a non-dimensional parameter referred to as the optimal vortex formation time [29]. This concept of optimal vortex formation time was extended to flapping flight by [14]. It was proposed that the inverse of Strouhal number is essentially equivalent to the concept of vortex formation time. A peak in propulsive efficiency in swimmers and fliers was

found at a Strouhal number range of  $0.2 \leq St \leq 0.3$  [76]. Hence, the non dimensional vortex formation time is close to 4.

The influence of airfoil kinematics on the flow development was studied on sinusoidal, asymmetric, and peak-shifted motion along with the optimal vortex formation time[64]. Asymmetric and peak-shifted motions impact the onset and growth of the LEV. The growth and pinch-off is delayed for peak-shifted case, as compared to the other motions. The vortex pinch-off was universal for all cases and occurred within  $4.4 < \hat{T} < 5$ , where  $\hat{T}$  is the dimensionless vortex formation time. Experiments on LEV growth and detachment from a plunging profile concluded that the chord length of the wing profile is the main characteristic length scale in describing the LEV detachment process.[65].

### 1.4 Vortex identification methods

The flapping cycles in biological fluid locomotion are dominated by the generation and shedding of organized vorticity [49, 14]. The distinct flow-fields and vortex dynamics generated by the unsteady motion of the flapping wing depend on the history effects of the motion as compared to steady wing kinematics. Analysing the dynamics of coherent structures is important to explain the flow physics, improve flow modeling, and predicting the aerodynamic forces, and will eventually lead to a better design of flow control surfaces for unsteady flight cases. Therefore, a crucial part of insect flight studies is to understand the vortex dynamics.

Some bio-inspired studies have focused on the correlation of forces with the presence of lift enhancing vortices through computational methods and flow visualisation. But there is still room for an in-depth analysis of the life-cycle of the LEV, its influence on the circulation, and how it is affected by wing rotation. Understanding the inherent non-linearity in the unsteady vortex dynamics can help exploit the energy of the flapping motion by means of advanced kinematic controls or flow control surfaces. This requires the identification of all the dynamically relevant features in the flow. The existing vortex detection methods can be broadly classified into Eulerian[44, 30] and Lagrangian methods[36].

While the Eulerian methods largely employ velocity gradients for detection and analysis of flow structures, the Lagrangian methods calculate scalar quantities based on particle trajectories of fluid elements. These scalar quantities are calculated using multiple velocity fields over a certain time period to determine regions of the flow which are dynamically distinguishable. They are inherently objective and include information on the history of the flow, unlike Eulerian methods [35]. Some vortex identification algorithms that are Lagrangian in nature have been demonstrated on unsteady flows[32, 19, 55]. The most commonly used Lagrangian approach, is the finite time Lyapunov exponent. Recently, FTLE has been applied to study bioinspired flows like unsteady wakes behind a pitching panel [33], fluid transport of translating and flapping wings [19] and identify the ring wake structure of a jellyfish [72].

Lagrangian coherent structures are shown to identify topological Lagrangian saddle points

which help characterise the flow fields. They can be tracked in time and can be correlated to pressure or velocity on the surface of the structure. This information can be used in the design of control surfaces to simulate topological changes in the flow. Lagrangian saddle points have the potential to provide more precise information about the timing and the location of vortex formation and evolution than the vortex cores identified by Eulerian techniques, which was demonstrated on a flat plate undergoing pitch-up manoeuvre [40]. In case of a cylinder wake, it was observed that the Lagrangian saddle point remains attached to the cylinder surface until the vortex separates, and then consequently accelerates downstream with a similar track in both numerical and experimental results [67]. On a helicopter blade undergoing dynamic stall, the Lagrangian saddle point indicated the detachment of the vortex from the boundary layer, marking the end of the stall development stage [54].

## **1.5 Objectives, approach, and overview**

Accurate information about the dynamics of fluid surrounding a hovering wing is strongly linked to the fundamental understanding of the development and interaction of coherent structures. The current work aims to provide a deeper insight into the formation, evolution, and breakdown of the characteristic flow features generated by a hovering wing. Planar particle image velocimetry (PIV) is carried out along with force measurements over a hovering flat-plate wing at mid-span with simplified hoverfly kinematics. Finite time Lyapunov exponent (FTLE) is used as a tool to identify and track the salient flow features. Lagrangian saddles are identified and tracked to characterise different flow stage in a hovering cycle. The flow-fields are then correlated with the kinematics and the forces. The effect of wing rotation with a lead or lag with respect to the stroke is discussed in terms of extensive analysis of vortex dynamics and correlation with the kinematics and force production. Furthermore, the effect of duration of rotation on the vortex dynamics and forces is analysed. The objective of this study is to characterise the effect of rotational timing on the flow fields and forces generated by a hovering wing.

The remainder of thesis is organised as follows. The experimental methods, parameters, and the different vortex detection methods for flow field analysis applied in this thesis are presented in chapter 2. Results and discussions in chapter 3 start with a roadmap outlining the details of the chapter. The analysis and discussion on a wing undergoing symmetric rotation with a small duration of rotation is presented in section 3.2. The formation, evolution, and breakdown of the characteristic flow features generated by a hovering wing are discussed here. The effect of rotational phase on the flapping cycle is analysed in section 3.3. The rotational duration of the wing in the base case is then doubled to investigate the influence of the duration of rotation on the hover characteristics. The key similarities and differences between a slow and fast rotation are presented in section 3.4.1. The slow wing rotation is then explored further by discussing the effect of varying phase-shift on the flow development in section 3.4.2 and 3.4.3. After a brief summary of the flow stages in section 3.4.4, the comparison for LEV circulation in the slow rotations are presented in section 3.4.5. The flow dynamics and

## **Chapter 1. Introduction**

---

kinematics are correlated with the measured forces in the slow rotation in section 3.4.6. Finally, the summary of the observations and conclusions are presented in chapter 4.

## 2 Experimental set-up and analysis

### 2.1 Experimental set-up

Quantitative velocity fields at the mid-span of a hovering flat plate wing were obtained along with direct force measurements. This section is dedicated to the description of the experimental facility, flow and force measurement techniques, and kinematic parameters used in this thesis.

#### 2.1.1 The mechanical flapper

The main aim of the experiment is to obtain the flow fields and force data for varying kinematics of a flapping wing in hover. For this purpose, a mechanical flapping wing mechanism was built by adapting the design of George et al. [28]. A schematic of the mechanism is shown in figure 2.1. Two maxon motors of type EC32 (80 W, 45 mNm torque) were used to actuate the wing in the pitching plane and a single maxon motor of type EC40 (120 W, 100 mNm torque) was used to control the wing in the stroke plane. The motors were connected via a drive-shaft to a combined worm-gear and bevel-gear system. A six-axis Nano17 IP68 force transducer with a capacity of 12 N and a resolution of 1/320 N was mounted close to the wing root. This transducer employs silicon strain-gauges to measure the loads and can be submerged in glycerin and water. The output of the sensor was passed through a calibration matrix provided by the supplier. The force coefficients were calculated by subtracting the bias values and rotated from the sensor coordinates to the lab coordinates. The rotation matrix accounted for the mounting angle of the sensor and instantaneous local angle-of-attack. More information on this is given in appendix A.

The control of the motors was achieved via a Galil DMC-4060 controller. The required motion was programmed using the firmware commands of the Galil software. A Labview program was developed to feed the motion program to the controller and acquire the forces from the force sensor. Direct force measurements were acquired at a sampling frequency of 10000 Hz through a NI data acquisition card. The signals were digitally filtered with a cut off frequency



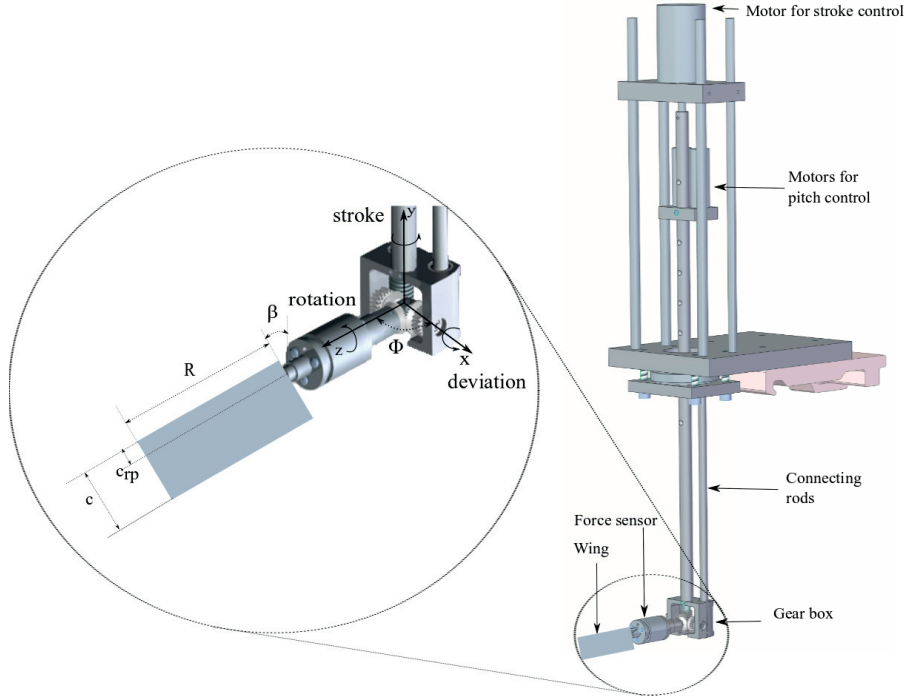


Figure 2.1 – A schematic of the wing mechanism. The inlay shows a zoomed in section of the wing apparatus with the three axes of motion.  $\phi$  is the position on the stroke plane and  $\beta$  is the rotational angle. The axis of rotation is marked by the dashed line on the wing at a distance of  $c_{rp}$  from the leading edge.  $c$  is the chord length,  $R$  is the wing span.

that is 8 times the stroke frequency.

The three axes of motion that the mechanism is capable of are displayed in the inlay of figure 2.1. The stroke (yaw) is defined as the revolving motion about the  $y$ -axis, rotation (pitch) is defined as the wing motion about  $z$ -axis and deviation is defined as the motion about the  $x$ -axis. The wing rotates about the  $z$ -axis at a distance of  $c_{rp} = c/4$  from the leading edge, where  $c$  is the wing chord. In this thesis, only two degrees of motion: stroke and rotation, are considered.

The model wing is dynamically scaled based on real hoverfly parameters indicated in table 2.1. With the wing span,  $R = 0.107$  m and chord length,  $c = 0.034$  m, the aspect ratio of the wing

Parameters	Real wing[51]	Model wing
Wing beat frequency, $f$ (Hz)	166	0.25
Chord length, $c$ (mm)	2.4	34
Wing span, $R$ (mm)	9.03	107
Stroke, $2\hat{\phi}$ , ( $^{\circ}$ )	148.2	180

Table 2.1 – Wing parameters



Parameters	Values
Density, $\rho$ ( $kg/m^3$ )	$1.168 \times 10^3$
Kinematic viscosity, $\nu$ ( $m^2/s$ )	$12.9 \times 10^{-6}$
Refractive index	1.422
Measurement temperature ( $^{\circ}C$ )	21

Table 2.2 – Fluid mixture parameters

is 3.1 which is similar to that of a real hoverfly [51]. For simplicity, a rectangular planform is adopted for the wing shape. The thickness of the wing is 2 mm. The flapping mechanism with the wing is immersed in an octagonal tank of outer diameter 0.75 m and a thickness of 0.04 m, which is filled with a mixture containing a volume percentage of 65% glycerin and 35% water.

### Scaling parameters

The two non-dimensional parameters associated with flapping flight in hover are reduced frequency ( $k$ ) and Reynolds number ( $Re$ ). The reduced frequency,  $k$ , provides a measure of unsteadiness associated with a flapping wing by comparing the spatial wavelength of the flow disturbance with the chord length. The reduced frequency is given by

$$k = \frac{\pi c}{2\hat{\phi}R}. \quad (2.1)$$

The reduced frequency for both the wings in hover are found to be  $k = 0.32$ . The Reynolds number of a wing in flapping flight is defined as

$$Re = \frac{U^* c}{\nu} = \frac{2\hat{\phi}fRc}{\nu} = \frac{\pi fRc}{\nu} \quad (2.2)$$

where  $U^* = 2\hat{\phi}fR$  is the mean flapping velocity for hovering flight[78]. This gives a Reynolds number of 220 for the model wing and 620 for a real hoverfly wing based on the experimental values given in table 2.1 and 2.2. The kinematic viscosity and the refractive index were measured using a viscometer and a refractometer respectively.

### 2.1.2 Particle image velocimetry (PIV)

Standard digital particle image velocimetry (PIV) is used to obtain the velocity fields around a flapping wing owing to its ease, robustness, and non-intrusive nature. The flow is homogeneously seeded with particles that are small enough to follow the fluid. Image pairs are

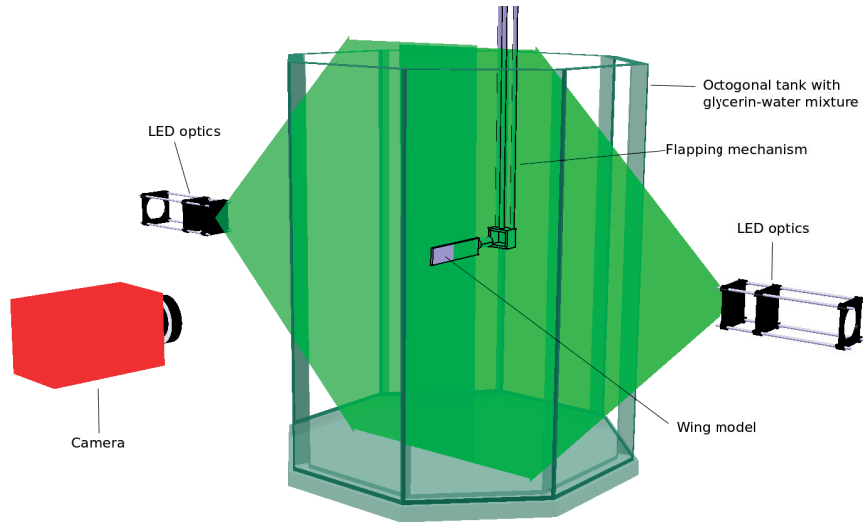


Figure 2.2 – Schematic of the experimental set-up

recorded with an appropriate time delay. The basic algorithm of PIV processing [90] employs the cross-correlation of sub-regions in the image for estimation of local displacement of particles from the image pairs.

The experiments were conducted in a quiescent flow on a mechanical flapping wing model, a schematic of which is shown in figure 2.2. Phase-locked PIV was conducted, i.e. the velocity fields are acquired at a fixed phase of the wing motion [61, 60] and phase averaged flow fields were determined.

### Seeding particles

Commercially available fluorescent dye particles (from Dantec dynamics) were used in the current experiment as the seeding agent. These particles are based on methyl methacrylate of diameter  $50\text{ }\mu\text{m}$ . Fluorescent dye (Rhodamine) is homogeneously distributed over the entire particle volume. The dye particles were found to settle at the bottom of the tank when used in water and required intermittent stirring. Whereas they remained suspended in glycerin-water mixture and followed the flow.

Particles	Polyamide	Hollow glass spheres	Fluorescent dye particles
Size ( $\mu\text{m}$ )	50	10	50
Shape	round	spherical	spherical
Material	Polyamide 12	Borosilicate glass	Methyl methacrylate
Refractive index	1.5	1.52	1.479
Density ( $\text{kg}/\text{m}^3$ )	$1.5 \times 10^3$	$1.52 \times 10^3$	$1.479 \times 10^3$

Table 2.3 – Seeding particles properties

Prior to choosing the fluorescent dye particles, polyamide particles and hollow glass spheres were tested. The polyamide particles of diameter  $50\text{ }\mu\text{m}$  often conglomerated and even dissolved partially over time. And the hollow glass spheres of diameter  $10\text{ }\mu\text{m}$  were too small to scatter light efficiently. The specifications of the particles tested are given in the table 2.3.

### Light source

LED based illumination was chosen over the more popular lasers due to the ease of setting up, safety, and relatively low costs. The light pulses generated by the LED were shown to be sufficient to illuminate and image micron-sized particles in flow velocimetry [89, 12]. The particles in the fluid were illuminated using a LED pulsing system and software (from ILA GmbH). The LEDs emitted a wavelength around  $530\text{ nm}$ . Two LEDs were used to achieve maximum light intensity in the measurement plane and to avoid shadows of the wing. Cylindrical lenses were used to create light sheets of equal intensity and were carefully aligned to illuminate the particles in the flow from opposite directions in the same plane. The two light sheets from opposite ends overlapped at the mid-span of the wing where the images were captured. The thickness of the light sheet was  $5\text{ mm}$ .

### Procedure

In the current experiment, images at different phases of the flapping cycle were acquired by shifting the starting location of the wing stroke, relative to the measurement plane. To conduct the phase-locked measurements, the camera, LED and the flapper were synchronised by means of a voltage trigger signal that was programmed to activate the LED pulse and record images on the camera. With the help of the feedback from the motor encoder, the position of the wing is monitored. When the wing is exactly perpendicular to the measurement plane, the trigger signal is sent to the camera and the LED to capture a single image pair per flapping cycle. This is schematically shown in figure 2.3. Throughout the flapping cycle, a minimum of 50 phases were recorded. For each phase, 30 flapping cycles were carried out. The images were captured only after the first 5 flapping cycles in order to mitigate transients from initialization of the experiments. The camera and light sources were stationary around the tank.

The raw data is processed with a multipass algorithm with a final interrogation window size of  $32\text{ px} \times 32\text{ px}$  and an overlap of 50%. This yields a physical resolution of  $1\text{ mm}$  or  $0.03c$ . Phase-averaged flow fields are presented in this thesis. Direct force measurements are acquired at a sampling frequency of  $10000\text{ Hz}$  through a NI data acquisition card and phase-averaged. The signals are digitally filtered with a cut off frequency that is 8 times the stroke frequency.

### 2.1.3 Wing kinematics

Basic kinematic patterns used in this study are presented in figure 2.4. As mentioned in section 2.1.1, the motion of the wing in stroke and rotation are considered. The **sinusoidal**

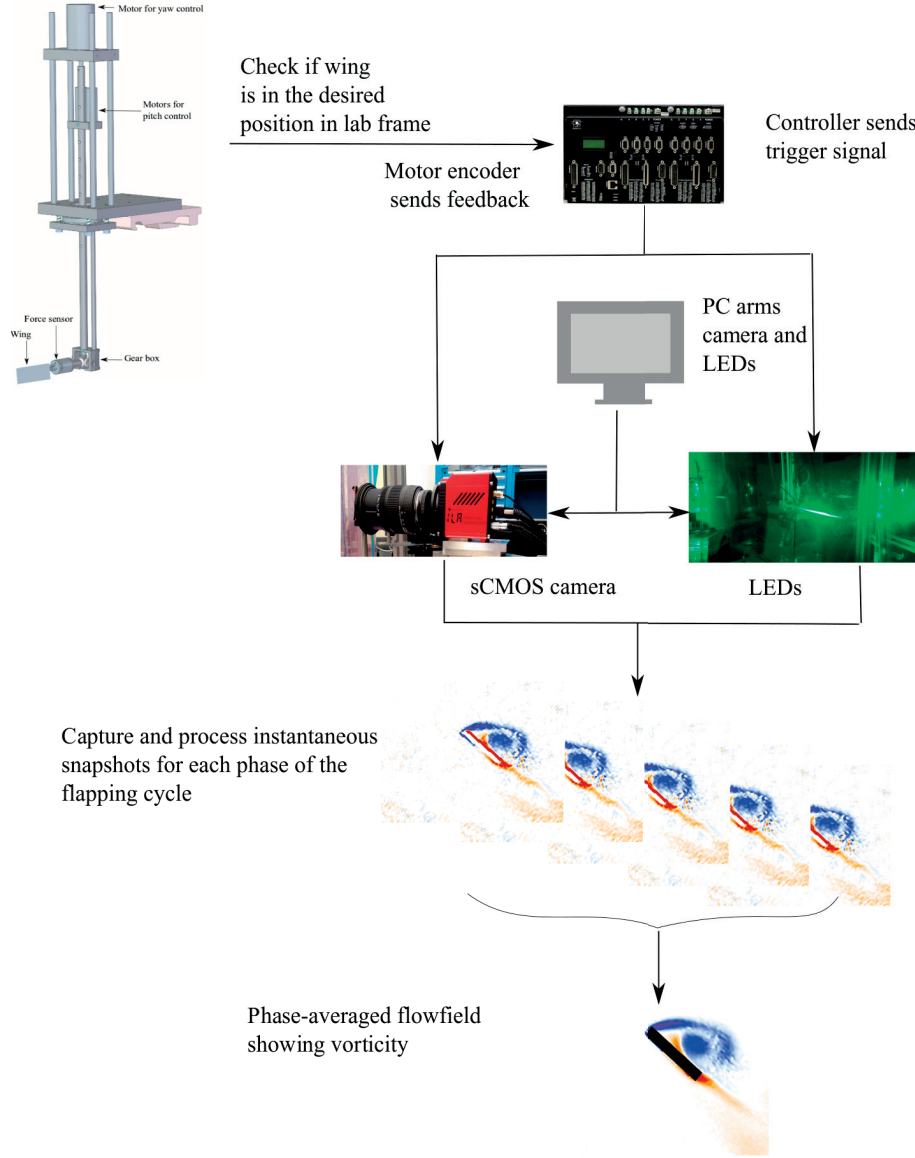


Figure 2.3 – Triggering mechanism and image acquisition

profile represents the **stroke**, also referred to as yaw (figure 2.4). And the **trapezoidal** profile represents the **wing rotation**, also referred to as pitch. The angular and temporal variations in these profiles constitute to the experimental parameter space for evaluation and comparison.

The temporal variation involves the change in the duration of wing rotation in every half-stroke, referred to as **flip duration** or **duration of rotation**. The flow evolution for a fast wing flip,  $T_f = T/6$ , was first investigated, after which the duration of rotation was doubled to get a slow flip :  $T_f = T/3$ ; where  $T = 4$  s is the time period of the flapping cycle.

The angular variation involves the change in the starting rotational angle  $\beta_0$ , while the starting stroke angle remains the same. This corresponds to a phase relationship between the wing

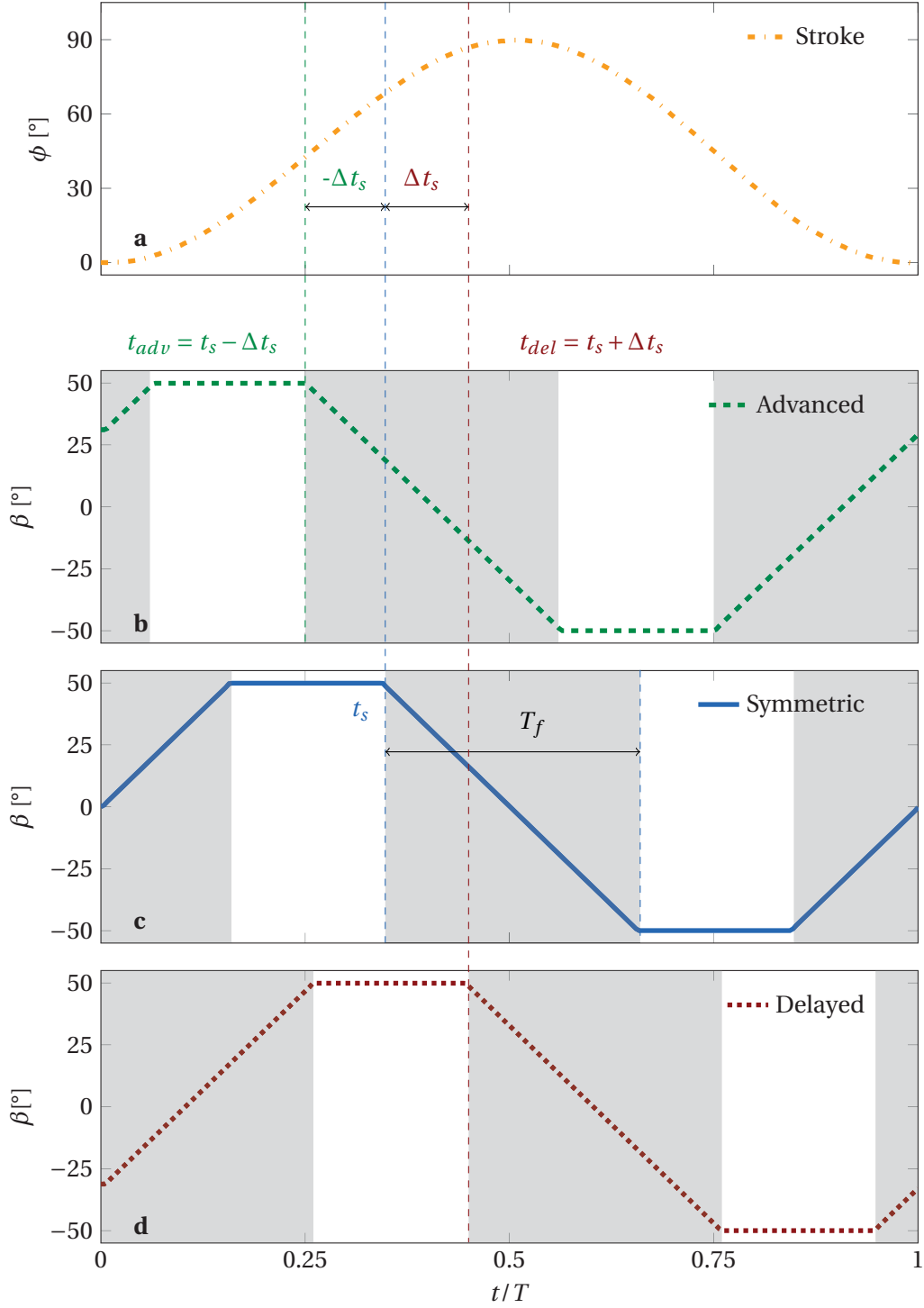


Figure 2.4 – Conceptual representation of the variations in the wing kinematics. The grey area indicates the duration of wing rotation in the flapping cycle. For a single stroke cycle,  $t_s$  refers to the start of rotation in the symmetric case,  $t_{adv}$  refers to the start of rotation in the advanced rotation case, and  $t_{del}$  refers to the start of rotation in the delayed rotation case. In each of these cases, the duration of wing rotation is  $T_f = T/3$  in every half-stroke with  $T = 4s$ .  $\Delta t_s$  refers to the phase shift for advanced and delayed rotation respectively.

rotation and stroke, which is referred to as **phase-shift**,  $\Delta t_s$ . The phase-shift is better quantified as the non dimensionalised time,  $t/T$ , by which the rotation start time,  $t_s$ , is advanced or delayed with respect to the case where both rotation and stroke angles start at  $0^\circ$ .

The phase-shift implies a change in the period of wing rotation at the end of each half-stroke which essentially constitutes the conventional distinction of different types of wing rotation: symmetric, advanced and delayed rotations. For a symmetric rotation case, the rotation start time,  $t_s$  and rotation end time,  $t_e$  are equally spaced about the stroke reversal occurring at  $t/T = 0.5$  and once again at  $t/T = 1$  (figure 2.4). This means that half of the wing's rotation occurs before the stroke reversal and half of it occurs after the stroke reversal. The symmetric case is taken as a base reference case for comparison. For a symmetric rotation case,  $\Delta t_s = 0$ . In the advanced rotation, the wing begins to rotate earlier than in the case of the symmetric rotation. This is represented by a negative  $\Delta t_s$ . In the delayed rotation, the wing begins to rotate later than in the case of the symmetric rotation. The delayed rotation is indicated by a positive  $\Delta t_s$ .

For all measurements the stroke motion and amplitude were kept constant. The stroke position of the wing ( $\phi$ ) follows a sinusoidal waveform with amplitude  $\hat{\phi} = \pi/2$ . The rotational angle ( $\beta$ ) is defined as the angle between the wing and the vertical axis. The rotational position of the wing in a flapping cycle varies as a trapezoidal function as  $-50^\circ \leq \beta \leq 50^\circ$ . The rotational angle is related to the geometric angle of attack as  $\alpha = 90^\circ - \beta$ .

PIV and force measurements were conducted for various phase-shifts for each flip duration. The phase-shifts are varied such that:

$$\Delta t_s = \left[ -\frac{T_f}{2}, -\frac{T_f}{4}, 0, \frac{T_f}{4}, \frac{T_f}{2} \right] \text{ for fast flip } (T_f = T/6)$$

$$\Delta t_s = \left[ -\frac{T_f}{2}, -\frac{T_f}{3.3}, -\frac{T_f}{4}, 0, \frac{T_f}{4}, -\frac{T_f}{3.3}, \frac{T_f}{2} \right] \text{ for slow flip } (T_f = T/3)$$

The variations in the flip duration and phase-shift, together characterises the term: **rotational timing**. The effect of this rotational timing on the aerodynamic forces and flow fields around a hovering wing was investigated.

## 2.2 Flowfield analysis

Vortex dynamics play an important part in characterising the role of the phase relation between the wing translation and rotation in lift generation around a hovering wing [82]. Identifying these canonical structures is important in order to explain the physics of flow, improve flow modeling, and force predictions, which eventually help in better design of flow control surfaces. There is a lack of agreement on the mathematical definition of a vortex which has resulted in a multitude of vortex identification criteria. The existing vortex detection methods can be broadly classified into Eulerian and Lagrangian methods.

### 2.2.1 Eulerian criteria

Study of experimentally obtained flow features around hovering wings has mostly been Eulerian in nature. Eulerian criteria typically concern with quantities derived from instantaneous velocity fields or gradients. Two Eulerian vortex identification criteria such as the  $\lambda_2$  criterion by Jeong and Hussain [44] and the  $\Gamma$  criterion by Graftieaux et al., [30] have been used extensively to locate and extract dominant structures in a flow field and will be described here.

#### $\lambda_2$ criterion

The  $\lambda_2$  criterion is based on the relation between a pressure minimum and the presence of a vortical motion. Neglecting the unsteady irrotational straining and the viscous effects in the gradient of the Navier-Stokes equations can be expressed as

$$S^2 + \Omega^2 = -\frac{1}{\rho} \nabla(\nabla p) \quad (2.3)$$

where  $\nabla(\nabla p)$  is the pressure Hessian and  $S = \frac{1}{2}[\nabla u + (\nabla u)^T]$  and  $\Omega = \frac{1}{2}[\nabla u - (\nabla u)^T]$  are the symmetric and antisymmetric components of the velocity gradient  $\nabla u$  respectively. Only  $S^2 + \Omega^2$  is considered for determining the existence of a local pressure minimum due to vortical motion. The occurrence of a local pressure minimum requires two positive eigenvalues of the pressure Hessian or in other terms, two negative eigenvalues of  $S^2 + \Omega^2$ . The eigen values of  $S^2 + \Omega^2$  can be grouped as  $\lambda_1 \geq \lambda_2 \geq \lambda_3$ . This requires  $\lambda_2$  within the vortex core to be negative. Therefore, the criterion defines the vortex core as

$$\lambda_2(S^2 + \Omega^2) < 0. \quad (2.4)$$

#### $\Gamma$ criterion

Despite their functionality in representing the characteristics of the flow features, methods based on local quantities are prone to small scale turbulence and measurement noise. As a solution to this, a Galilean invariant procedure was introduced by Graftieaux et al. [30] which computes the vortex core based on the topology of the velocity field rather than the local gradient. It can be used for statistical analysis of large sets of instantaneous velocity fields as shown by Mulleners et al., [55], where the vortex dynamics of stall development around an airfoil from time resolved PIV data was discussed by detecting the vortex centres and tracing the trajectories over a time series of flow fields.

Graftieaux et al. defined a scalar function ( $\Gamma_1$ ) by using the topology of the velocity field to obtain the axis of the vortex core [30]. The velocity field is sampled at discrete spatial locations

and the dimensionless scalar function,  $\Gamma_1$ , is defined as-

$$\Gamma(P) = \frac{1}{N} \sum_{i=1}^N \frac{[(PM \times (U_M)) \cdot z]}{\|PM\| \cdot \|U_M\|} dS = \frac{1}{N} \sum_{i=1}^N \sin \theta_M \quad (2.5)$$

where  $S$  is a rectangular domain of fixed size and geometry, centered on a fixed point  $P$ .  $M$  represents  $N$  number of points that lies in the domain  $S$  and  $z$  is the unit vector normal to the measurement plane.  $\theta_M$  is the angle between the velocity vector  $U_M$  and the radius vector  $PM$  between the node on the center of the plane and the points  $M$ . The location of the vortical structures is determined by a local extremum. The function is not Galilean invariant and a function  $\Gamma_2$  was proposed to identify the boundary of the vortical structures which took the local convective velocity  $\tilde{U}_p$  into account. The Galilean invariant  $\Gamma_2$  is defined as

$$\Gamma_2(P) = \frac{1}{N} \sum_{i=1}^N \frac{[(PM \times (U_M - \tilde{U}_p)) \cdot z]}{\|PM\| \cdot \|U_M - \tilde{U}_p\|} dS \quad (2.6)$$

where  $\tilde{U}_p = \frac{1}{N} \sum_{i=1}^N U dS$ .

### Vorticity contour method

Eulerian criteria such as  $\lambda_2$  and  $\Gamma_2$  successfully identify large scale structures but do not detect the coherent vortices within the concentrated vorticity in a shear layer. The identification of the smaller structures within the shear layer could be important when predicting the overall circulatory contribution to the aerodynamic forces produced, in applications such as flapping wing flows. To detect the smaller flow features along with the prominent large scale vortices, an alternative method of vortex identification is proposed in which the flow structures are detected based on the vorticity contours. The largest contour of each local maximum in the flow field is detected as a flow feature. In this method, the vorticity contours of the same levels are selected. The local vorticity maxima are identified. The largest contour lines among consecutive contour lines that share the same peak are identified. These largest contour lines basically represent all the unique parent structures in the frame which consist of smaller contours belonging to the particular peak. The smallest contour line belonging to each of these unique parent structures is taken as the boundary of the flow feature.

Eulerian criteria work well in identifying vortex cores by using the instantaneous local velocity gradients or the topology of the flow field. However, the visualization of these structures depend on a user defined threshold which negates objectivity from analysis. As pointed out by [35], even though criteria like  $\Gamma_2$  are Galilean invariant, they are not invariant to time-dependent rotations. Hence they are not frame-independent. This leads to the introduction



of the Lagrangian technique to analyse flow fields.

### 2.2.2 Lagrangian analysis

In addition to the commonly used Eulerian methods, some coherent structure identification algorithms that are Lagrangian in nature have been in use in the last decade [40, 66, 32, 55]. The Lagrangian approach involves looking at the flow by following the fluid elements as they move through space and time. The trajectories of the fluid elements or fluid particles help in the identification of coherent structures. They are inherently objective and include information on the history of the flow. The most commonly used Lagrangian approach, also used in this thesis, is based on the Lyapunov exponent and is presented in this section.

The Lagrangian analysis in the current study includes a calculation of the finite-time Lyapunov exponent (FTLE), which is a scalar field defined at time  $t_0$  based on the behaviour of particle trajectories initialized at  $t_0$ . The flow map  $F_{t_0}^{t_1}(x_0)$  at each point in space is calculated as the vector location of each trajectory initialized at  $(x_0, t_0)$  at the end of an integration time  $t_1$ . The Cauchy-Green strain tensor is constructed from the local spatial gradient of the flow map  $(\nabla F_{t_0}^{t_1}(x_0))$  [37]. The coefficient of expansion  $\sigma$  is defined as the maximizing eigenvalue of the Cauchy-Green tensor

$$\sigma_{t_1}(x_0, t_0) = \lambda_{\max} \left( \left[ \nabla F_{t_0}^{t_1}(x_0) \right]^* \left[ \nabla F_{t_0}^{t_1}(x_0) \right] \right) \quad (2.7)$$

where  $*$  is the matrix transpose operator. The FTLE field is then defined as

$$\text{FTLE}_{t_1}(x_0, t_0) = \frac{1}{2t_1} \log \sigma_{t_1}(x_0, t_0). \quad (2.8)$$

FTLE is a measure of Lagrangian stretching among nearby trajectories as the flow evolves in space and time. The maximizing ridges of the FTLE field are referred to as the Lagrangian coherent structures (LCS), which are effective at identifying coherent structure boundaries and evolution dynamics in vortex dominated flows. This calculation can also be done in reverse time, because regions where flow undergoes Lagrangian stretching in reverse time correspond to regions where the flow is currently experiencing local attraction. By including ridges from both FTLE calculations, the analysis produces both the repelling lines along which particle trajectories locally will separate from each other (positive-time, pFTLE) or attracting lines along which particle trajectories have locally contracted to each other (negative-time, nFTLE) as shown in figure 2.5. In general, these ridges provide boundaries delineating where particles are entrained into a vortex, and where they continue to convect with the outer flow [33].

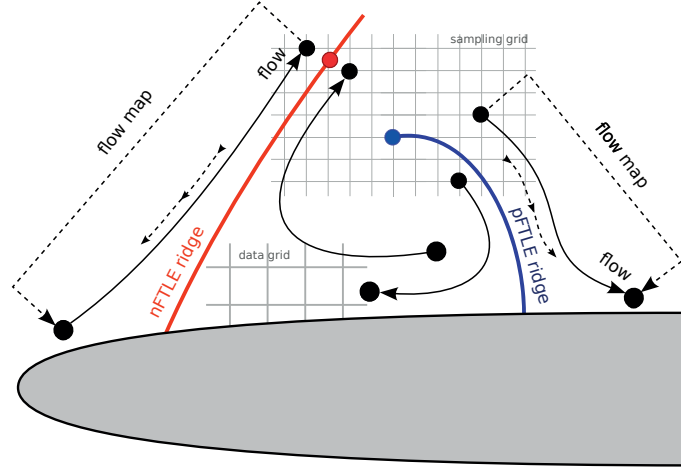


Figure 2.5 – A schematic of Lagrangian calculation. Fluid close to the boundary is stretched alongside the attracting material line (nFTLE ridge) whereas fluid is guided in opposite direction by the repelling material line (pFTLE ridge). Modified from Sadlo et al.[68]

In this study, a non-linear time vector is used for integrating the FTLE fields owing to the fact that the images were captured at regular intervals of the stroke amplitude instead of uniform time intervals.. The phases in the flapping cycle at which images were recorded, were chosen based on the angular spacing of the stroke motion, as depicted by the blue dots on the sinusoidal profile in figure 2.6. The time difference between consecutive images,  $\Delta t_1, \Delta t_2, \dots, \Delta t_{n-1}$ , is schematically represented in the same figure.

FTLE is calculated using an integration time of one-eighth of the time period of the flapping cycle ( $t_1 = 0.125T$ ), with a time step of  $0.0025T$ . The integration time influences the sharpness

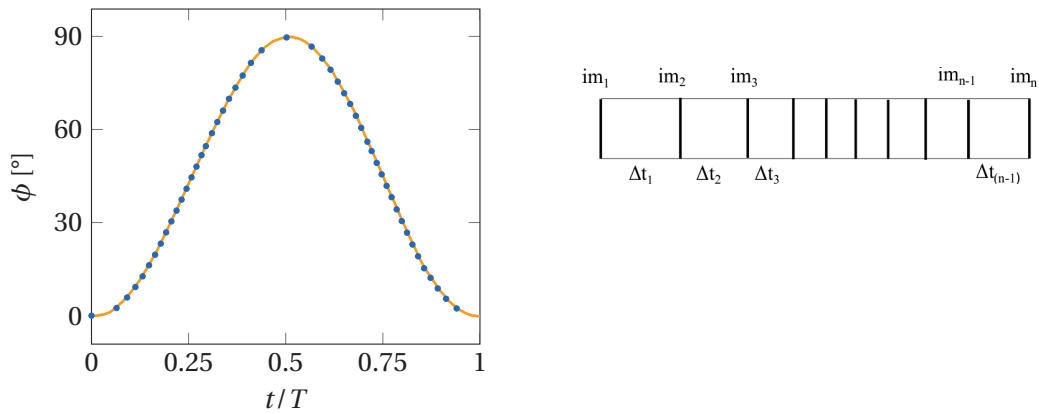


Figure 2.6 – Schematic representation of the time intervals between the recorded images in the stroke. The blue dots on the sinusoidal profile indicate the time instants at which the images were recorded. The schematic on the right shows a difference in the time intervals ( $\Delta t_1, \Delta t_2, \dots, \Delta t_n$ ) between consecutive  $n$  number of images ( $im_1, im_2, \dots, im_n$ ).

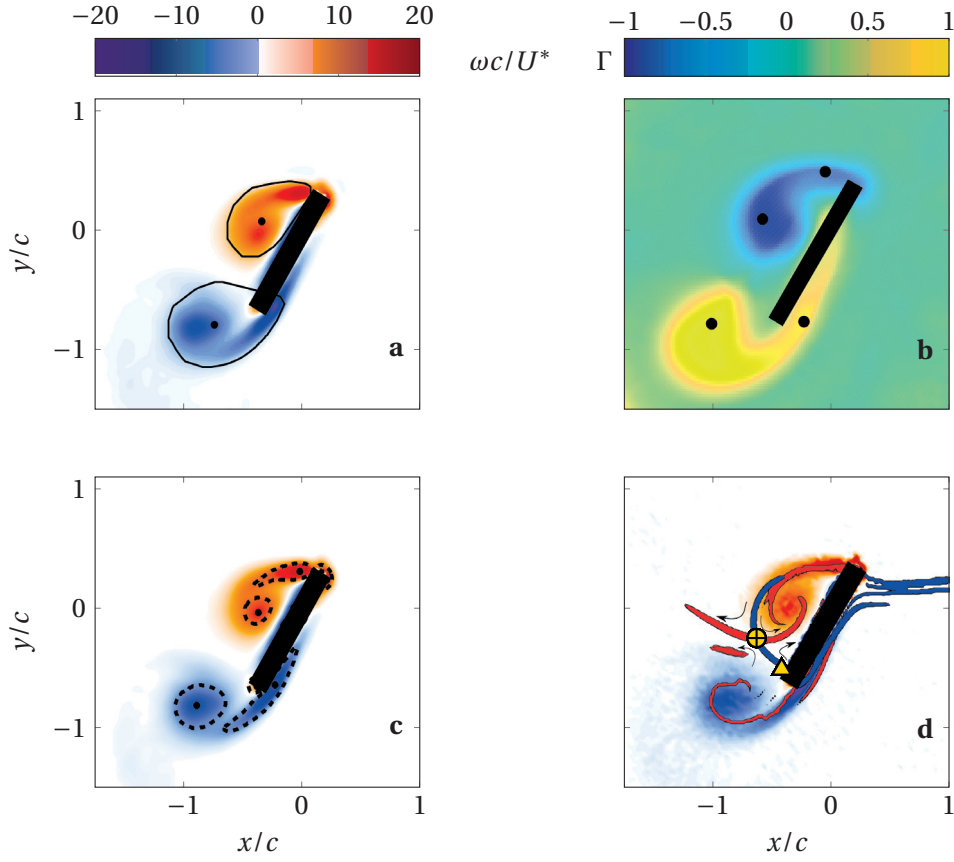


Figure 2.7 – Various vortex detection methods applied on the current data set. The images show the flow field around the wing at  $t/T = 0.73$  of the flapping cycle.

and clarity of the FTLE ridges. The location of the ridges that indicate the boundaries are not affected. FTLE values greater than 60% of the maximum are extracted for visualisation. The analysis is conducted in the wing reference frame. The velocity of wing sweep,  $u_\phi$ , which corresponds to the induced velocity due to the wing's stroke motion at each time frame, is added to the entire velocity field. To avoid boundary effects, the particles that reach the boundaries are given the corresponding velocity of  $u_\phi$ .

An example of all the Eulerian criteria mentioned here and the Lagrangian method is applied on the current experimental data set and is presented in figure 2.7. In figure 2.7(a), vorticity is calculated as the curl of the velocity fields, non-dimensionalised with the chord ( $c$ ) and average wing tip velocity ( $U^*$ ). The positive vorticity in this figure represents the LEV and the negative vorticity represents the TEV. The  $\lambda_2 = 0$  contours are denoted in black. The black dots represent the locations of the vortices, which are calculated as the centroids of the identified structures. Figure 2.7(b) shows the Galilean invariant  $\Gamma_2$  criteria to identify the vortical structures and the peak values give their locations; indicated by the black dots. Figure 2.7(c) shows the vorticity contour method. The dashed black lines represent the vortex boundaries and the black dots represent the locations. The contours are plotted at every 2.5%

of the vorticity limit values in this work. Figure 2.7(d) shows the Lagrangian analysis. The attracting material lines (**nFTLE**) indicate the boundary of the flow structure and the repelling material lines (**pFTLE**) indicate where the flow diverges.

The Eulerian methods in the figure 2.7 indicate the boundaries of the flow structures along with the axis of vortex cores for the particular time instant, but do not give information on the dynamics of the flow. In contrast, the nFTLE ridge which forms the boundary of the LEV shows that the flow experiences an attraction in this region. The pFTLE ridge indicates that the flow in this region is repelled. So the intersection of the nFTLE and pFTLE ridges are topological saddle points. These saddles in general are not always easily identifiable from the Eulerian methods due to chosen frame of reference. The pFTLE ridge at the surface of the wing forms a half-saddle ( $\Delta$ ) and interacts with the nFTLE to form a full-saddle ( $\oplus$ ). This full saddle clearly indicates the local direction of the flow. The Lagrangian approach thus offers more advantages for an in-depth analysis of the flow features and is therefore employed in the current work.

## 3 Results and discussions

### 3.1 Roadmap

The objective of this study is to characterise the effect of rotational timing on the flow fields and forces generated by a hovering wing. The flow fields obtained from the experimental investigation are analysed and explained using phase-averaged vorticity along with the FTLE results. The measured aerodynamic forces are correlated with the kinematics and the flow features to provide a deeper insight into the mechanisms involved in a hovering cycle, specially during wing rotation.

To distinguish the effect of wing rotation on the hovering cycle, it is necessary to first understand the flow and force behaviour in a typical flapping cycle. Therefore, the first section is dedicated to the analysis and discussion of a wing undergoing symmetric rotation with a small flip duration ( $T_f = T/6$ ), which is taken as a base case (section 3.2). The dynamically relevant flow features such as the primary leading edge vortex (LEV), secondary vortices, topological saddles, and their evolution within a flapping cycle are discussed.

With the knowledge of flow features during a typical flapping cycle, the discussion is then geared towards the effect of varying phase-shift on the formation and evolution of lift-enhancing flow structures during a fast wing rotation (section 3.3). Two incremental phase-shifts for each advanced and delayed rotations are investigated. A comparison of the effects of an early or late wing rotation with respect to the base case is provided. Quantitative force comparisons are correlated with the vortex dynamics. The key similarities and differences in different cases are highlighted.

The results obtained from the previous sections motivates the next question: How does the duration of rotation impact the hover characteristics? The influence of the flip duration on flow and force evolution is investigated by doubling the duration of rotation with respect to the base case. The vortex dynamics and forces around a wing undergoing a symmetric rotation with flip durations of  $T_f = T/6$  and  $T_f = T/3$  are compared in section 3.4.1. The findings are correlated with the kinematics and the key similarities and differences with respect to the base

case are presented.

Finally, the slow wing rotation is further explored by investigating the effect of rotational phase on the flapping cycle. The goal is to investigate if and how the variations in phase-shift alter the flow dynamics and forces on a wing rotating slowly and its relation to the history of the motion. This was investigated for three incremental phase-shifts each in advanced and delayed rotations. The results show interesting variations for advanced and delayed rotations. As representative cases, the unsteady flow development in fully advanced and fully delayed rotations of the slow flip are discussed in sections 3.4.2, 3.4.3, respectively. This is complemented with the quantitative comparisons of flow characteristics for all the slow rotations. The most prominent differences in the flow stages of advanced and delayed rotation with respect to the symmetric rotation are compared and summarised in section 3.4.4. The chapter ends with the correlation of the aerodynamic forces and the corresponding flow behaviour with the kinematics for all slow rotations in section 3.4.6.

### 3.2 Flow development stages for a symmetric flapping cycle

The most common type of wing rotation seen in insects is the symmetric rotation where the wing rotates symmetrically about the stroke reversal. In this experiment, the reciprocating motion (stroke) is symmetric about the stroke reversal as is the case for many hovering insects [86], with the wing velocity in the stroke plane varying in a sinusoidal form. This symmetry results in similar flow evolution during front and back strokes. Only the back stroke of a flapping cycle where the wing rotates for a sixth of a period is discussed.

The development of the unsteady flow field around a flapping wing is divided into 4 stages that are outlined in figure 3.1. The first stage commences with the accumulation of vorticity on the wing (figure 3.1 (a)). This **LEV emergence** stage is characterised by an unbound LEV that grows in the chord-normal direction (figure 3.1 (b)) until the end of the first rotation. The flow then transitions into the second stage, **LEV growth**, where the LEV moves towards the wing and binds to the suction side of the wing (figure 3.1 (c)). A translational starting vortex forms at the trailing edge at the beginning of this stage, which is convected away shortly thereafter. The bound LEV grows in the chordwise direction until it reaches the trailing edge which marks the end of this stage (figure 3.1 (d)). The LEV then lifts off from the surface of the wing near the trailing edge, marking the transition into the **LEV lift-off** stage (figure 3.1 (e)). This lift-off from the wing surface allows a reverse flow from the trailing edge to the leading edge, giving rise to a secondary vortex of opposite sign between the wing and the LEV. The secondary vortex pushes

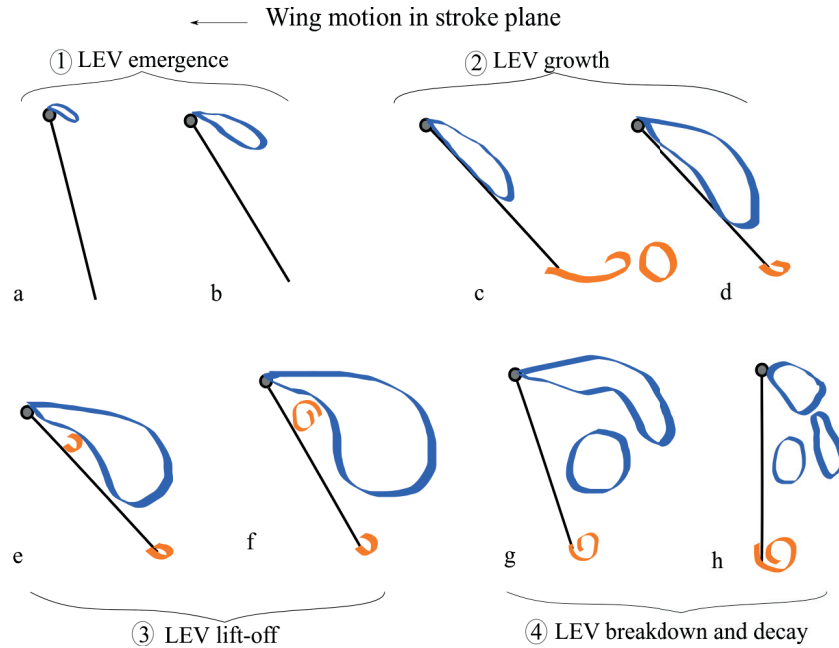


Figure 3.1 – Characteristic flow development in a typical flapping cycle as the wing (black lines with circles that represent the leading edge) moves to the left. The illustration of the features is based on vorticity. Blue features are indicative of the leading edge vortex and orange are indicative of the trailing edge vortex.

the LEV further away marking the end of the third stage (figure 3.1 (f)). The LEV eventually splits into multiple connected vortical concentrations as it approaches the end of the stroke when the wing rotates again (figure 3.1 (g)). This indicates the onset of the **LEV breakdown and decay** stage. The vortical concentrations close to the wing follow the wing, while the concentrations furthest from the wing convect away. This final stage of the half-stroke is also characterised by the formation and shedding of a rotational starting vortex at the trailing edge. The multiple vortical concentrations decay at the end of the half-stroke and spread out around the wing (figure 3.1 (h)). The above outlined stages of unsteady flow development in a flapping cycle will be further explained hereafter with reference to the wing kinematics.

### 3.2.1 LEV emergence

The first stage at the start of a half-stroke is characterised by the accumulation of vorticity at the leading edge. The life-cycle of the new flow features in the half-stroke begins as the wing moves through the remnant vorticity from the previous stroke. Vorticity is first generated at the leading edge and accumulates to form a compact leading edge vortex (figure 3.2(a)). This is due to a continuously rotating wing that moves in the fluid with an increasing stroke velocity (figure 3.2). The wing rotation drives the accumulation of vorticity to follow the trajectory of the leading edge rather than to settle on the suction side of the wing (figure 3.2(b)). The short duration of rotation combined with low stroke velocity inhibits the development of a bound

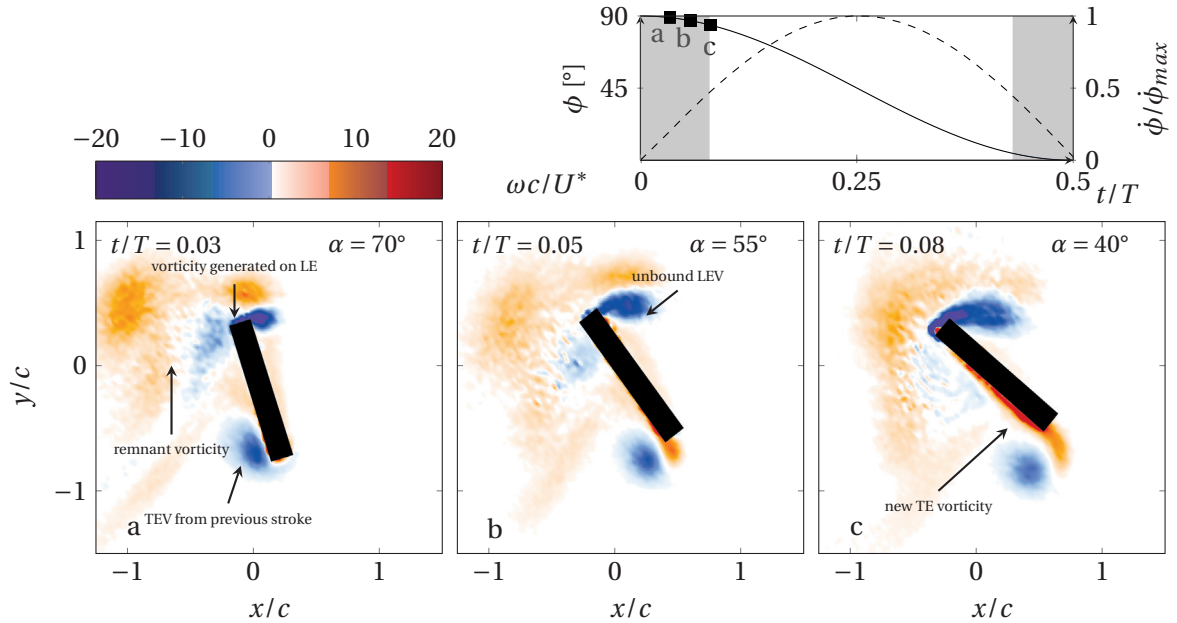


Figure 3.2 – Flow fields showing the LEV emergence process. Top right: Stroke position (—) and stroke velocity (---) of the half-stroke with the corresponding time instants.



### 3.2. Flow development stages for a symmetric flapping cycle

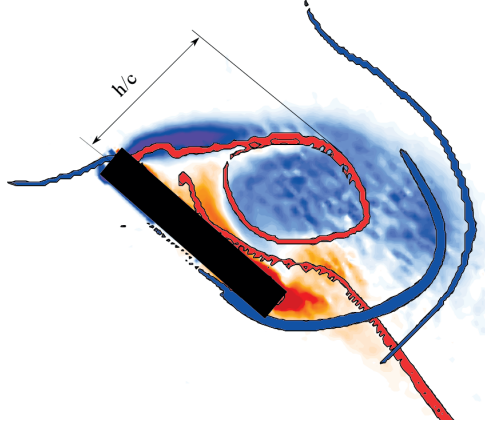


Figure 3.3 – Example of the chord normal distance ( $h/c$ ) of the outermost point of the LEV. The **nFTLE** ridges represent the attracting material lines that indicate the boundary of the flow structure and the **pFTLE** ridges represent the repelling material lines along which flow diverges.

LEV in this stage. This unbound LE vorticity grows in the chord-normal direction until the end of the emergence stage which coincides with the end of the first rotation in the half-stroke (figure 3.2(c)). The end of this stage is marked by the emergence of a pFTLE ridge on the surface of the wing. It is worth noting that in previous studies, the LE vorticity is generally found to be a bound feature on the suction side of the wing at mid-span [75].

The chord-normal development of the LEV can be tracked by quantifying the distance between

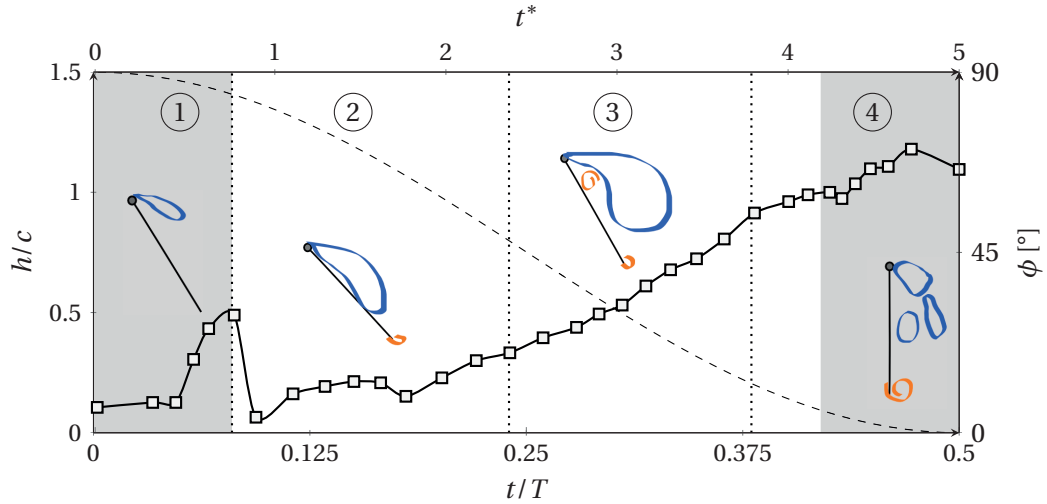


Figure 3.4 – Chord-normal distance of the outer LEV boundary indicated by the **nFTLE** ridge (figure 3.3). The gray region indicates the period of wing rotation. The vertical dotted lines denote the stages in the flow development which are represented by the sketches corresponding to LEV (1) emergence, (2) growth, (3) lift-off, and (4) breakdown(L-R). The top  $x$ -axis denotes the convective time scale ( $t^* = U^* t/c$ ).

the chord and the outermost point of the nFTLE ridge that forms the boundary of the LEV in each frame (figure 3.3). The chord normal distance of the LEV ( $h/c$ ) for the entire half-stroke is presented in figure 3.4 —□— in detail. The top  $x$ -axis of the figure indicates the convective time scale ( $t^* = U^* t/c$ ) where  $t$  is the timescale of the flapping cycle. The chord-normal distance of the outer LEV boundary increases during the first stage indicating that the LEV trails behind without binding to the wing's surface (figure 3.4, region ①). The end of the first stage corresponds with the end of rotation at which point the wing has traveled for less than 1 convective time scale.

During this first stage, a shed trailing edge vortex from the previous stroke stays intact and close to the trailing edge on the pressure side of the wing (figure 3.2(a)-(c)). A thin region of oppositely signed vorticity is generated on the pressure side of the wing as a consequence of the wing motion (figure 3.2(c)). The fast rotation combined with low stroke velocity delays the formation of a translational starting vortex at the trailing edge. The flow field at the end of the formation stage is characterised by an unbound LEV on the wing, which is at an angle of attack,  $\alpha = 40^\circ$  (figure 3.2(c)).

### 3.2.2 LEV growth

The second stage in the flapping wing cycle is dominated by the binding and chord-wise growth of the LEV on the suction side of the wing. The LEV observed at the end of the emergence stage moves towards the wing surface when the pure translation phase begins, binding to the wing (figure 3.5(a)). This is due to a constant pitch angle combined with an increasing stroke velocity. The LEV then grows in the chord-wise direction in size and strength (figure 3.5(b)-(c)). This development of the LEV is characterised by the movement of topological saddles that are identified as the intersection of the FTLE ridges. The movement of these saddles can be observed by tracking the full-saddle (⊕) and half-saddle (△) in figure 3.5.

To describe this phenomenon in detail, the FTLE ridges and the saddles during this stage are isolated in figure 3.6. The nearly horizontal nFTLE ridge (red) connected to the wing at the leading edge at the end of the LEV emergence stage pivots around the leading edge, indicating that the attracted fluid moves towards the wing surface (figure 3.6(a)-(d)). A pFTLE ridge (blue) emerges at the start of the pure translation phase at about quarter-chord of the wing, and define together with the nFTLE ridge a compact region of leading edge vorticity (figure 3.6(b)). The point of intersection of the pFTLE ridge and the wing is the location of a half-saddle (△) on the surface of the wing (figure 3.6(b)). The pFTLE ridge intersects with the nFTLE ridge revealing the location of a full-saddle (⊕). This full-saddle is taken as the outermost point on the boundary of the LEV during this stage since it represents the point near which the flow diverges. The chord-normal distance between the full saddle and the chord-line,  $h/c$ , decreases as the LEV moves towards the wing (figure 3.4, region ②). The chord normal distance thereafter remains approximately constant through this stage, showing

### 3.2. Flow development stages for a symmetric flapping cycle

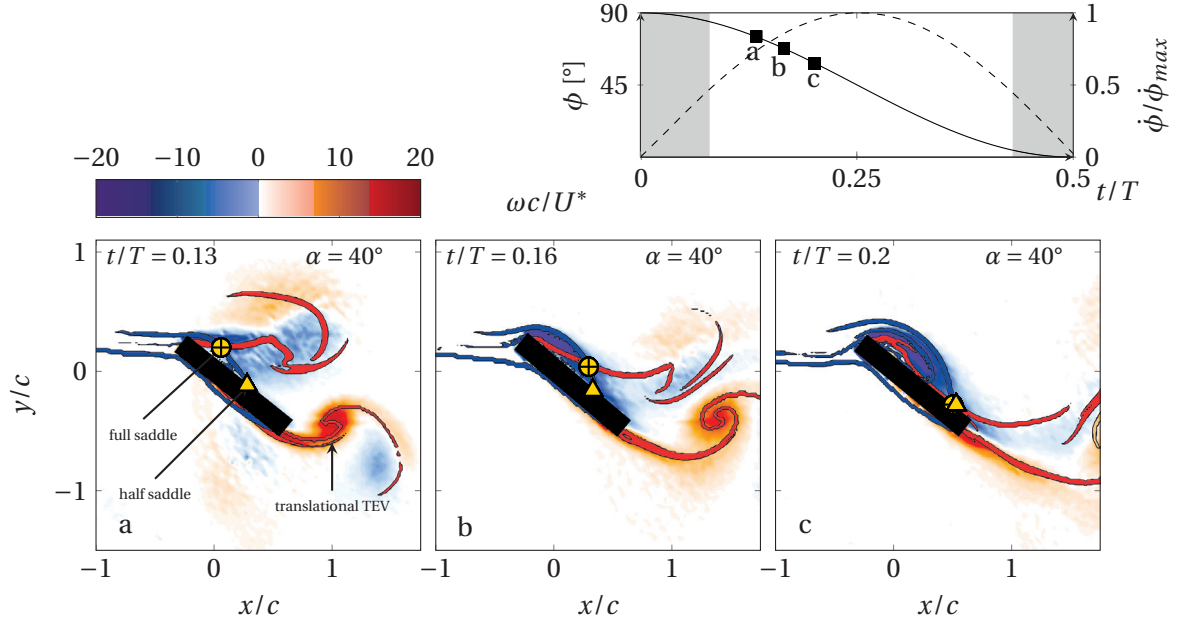


Figure 3.5 – Flow fields showing the growth of the bound LEV. **nFTLE** and **pFTLE** ridges are overlaid on phase-averaged vorticity fields. The full saddle is indicated by  $\oplus$ , and the half-saddle is indicated by  $\triangle$ . Top right: Kinematics (gray bars indicate period of rotation in the cycle).

that the full saddle remains close to the wing.

The movement of the full ( $\oplus$ ) and half ( $\triangle$ ) saddle can be visualised and quantified by the distance between the saddles and the wing's axis of rotation at quarter-chord, henceforth referred to as saddle distance ( $s/c$ ). This saddle distance is tracked for the half-stroke in the rotated wing frame (figure 3.7). Both saddles emerge at the beginning of the pure translation phase as seen in the saddle distance curve. The half-saddle distance increases nearly linearly, at the rate of 1.5 chord-lengths per second, indicating its rearward movement on the surface of the wing ( $\triangle$ ). The full saddle distance ( $\oplus$ ) decreases initially as it moves closer to the axis of rotation from the leading edge at the beginning of the LEV growth stage. A local minimum

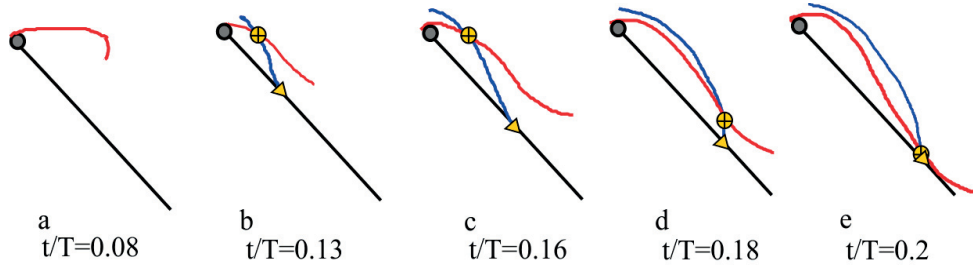


Figure 3.6 – LEV binding phenomenon during pure translation. The sketch is based on the **nFTLE** and **pFTLE** ridges.

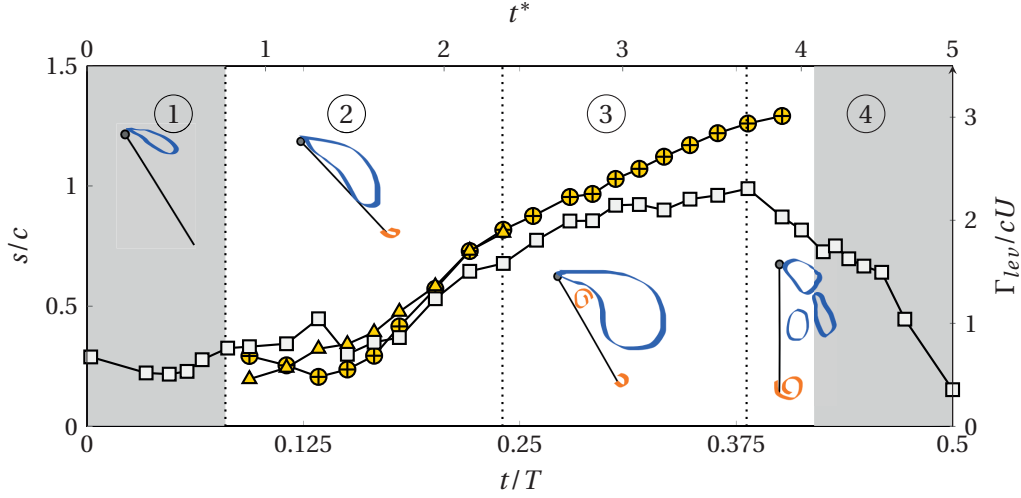


Figure 3.7 – Distance of the full saddle ( $\text{---}\bullet\text{---}$ ), half saddle ( $\text{---}\blacktriangle\text{---}$ ) from the axis of rotation; LEV circulation ( $\text{---}\square\text{---}$ ) during the half-stroke. The gray region indicates the period of wing rotation. Top x-axis shows the convective time scale ( $t^*$ ). The vertical dotted lines separate the LEV (1) emergence, (2) growth, (3) lift-off, and (4) breakdown stages (L-R).

in the saddle distance is observed at  $t/T \approx 0.15$ . At the same instant, a local maximum in the LEV circulation is observed (figure 3.7– $\square$ –). This is due to the large region of dispersed LE vorticity from the emergence stage (figure 3.5(a)-(b)). Most of the leading edge vorticity collects in a thinner region close to the wing surface soon after  $t/T = 0.15$ , which reduces the LEV area briefly and thereby the circulation (figure 3.5(c), figure 3.7– $\square$ –).

The full-saddle distance ( $\text{---}\bullet\text{---}$ ) continues to increase almost linearly after this instant, as it moves away from the axis of rotation along the chord. The full-saddle merges with the half-saddle on the surface of the wing close to the mid-half-stroke at  $t/T = 0.2$  (figure 3.5(c), figure 3.7). The merge occurs when the stroke velocity is three-fourths of its maximum in the half-stroke. The merged half-saddle continues to move rearwards and reaches the trailing edge at 2.4 convective time scales. At this instant, the LEV covers the entire chord length of the wing and this marks the end of the second stage.

The LEV growth stage is marked by continuous feeding of vorticity into the LEV. This is observed by the vorticity flux (figure 3.8). The flux is calculated as the vorticity convected through a line close to the leading and trailing edge. It is given by

$$\omega_{\text{flux}} = \int_L \omega \cdot \vec{u} \cdot \vec{n} dl \quad (3.1)$$

with  $\vec{n}$  being the unit vector normal to the line along which the flux is integrated. The line boundaries chosen at the leading and trailing edge are shown in the rotated wing frame in

### 3.2. Flow development stages for a symmetric flapping cycle

figure 3.8. The LEV growth stage is characterised by a steep rise in leading edge vorticity flux.

The LEV growth stage is also characterised by the formation of a translational starting vortex (TSV) at the trailing edge (figure 3.5 (a)-(c)). The translational starting vortex (TSV) is formed when the wing maintains a constant pitch angle and moves with an increasing stroke velocity. The TSV is fed by positive vorticity here and a maximum flux is observed just after the beginning of the growth (figure 3.8). The TSV is convected away at the end of the growth stage (figure 3.5(c)).

#### 3.2.3 LEV lift-off

The lift-off of the saddle point that binds the LEV to the wing marks the transition into the third stage of the flow development. At the end of the growth stage, the merged half-saddle has traveled to the trailing edge ( $s/c = 0.75$ ). At the beginning of this third stage, it lifts off of the wing at  $t/T = 0.25$ , when the maximum stroke velocity is reached (figure 3.9(a)). The rate at which the saddle moves away from the wing decreases by half in the lift-off stage. The LEV lifts off of the wing near the trailing edge as the half-saddle no longer binds it to the wing. This LEV lift-off opens up space between the wing and the LEV, allowing backflow along the surface. This is visualised in figure 3.10. The figure shows a time-wise variation of the

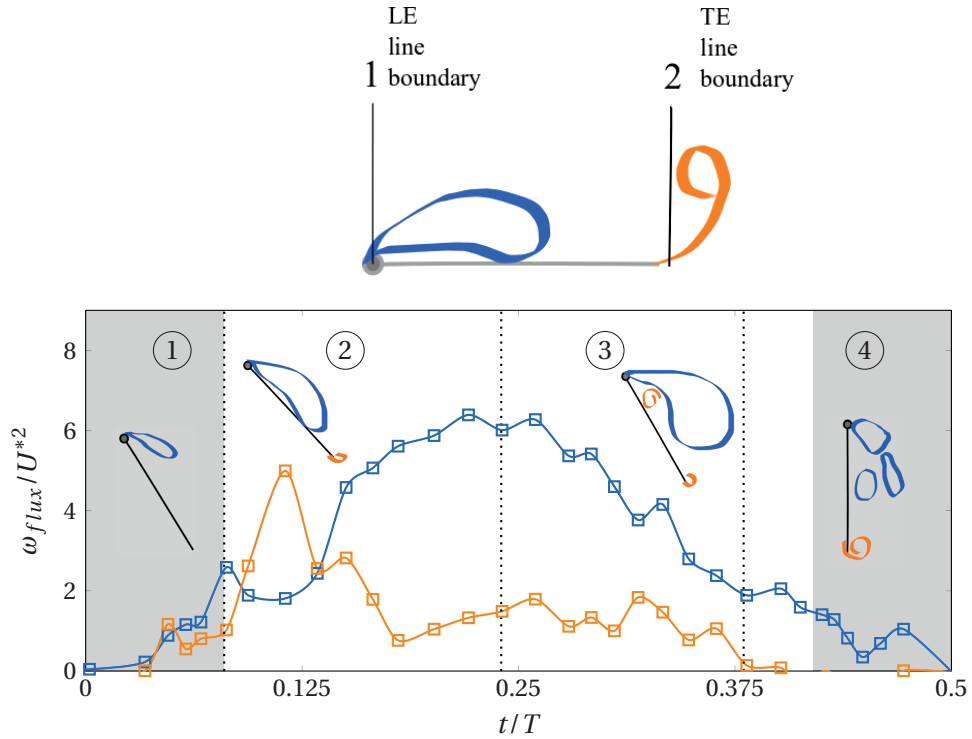


Figure 3.8 – Vorticity flux near the leading edge (—□—) and trailing edge (—□—). Schematic of the leading and trailing edge line boundaries to calculate the vorticity flux on top.

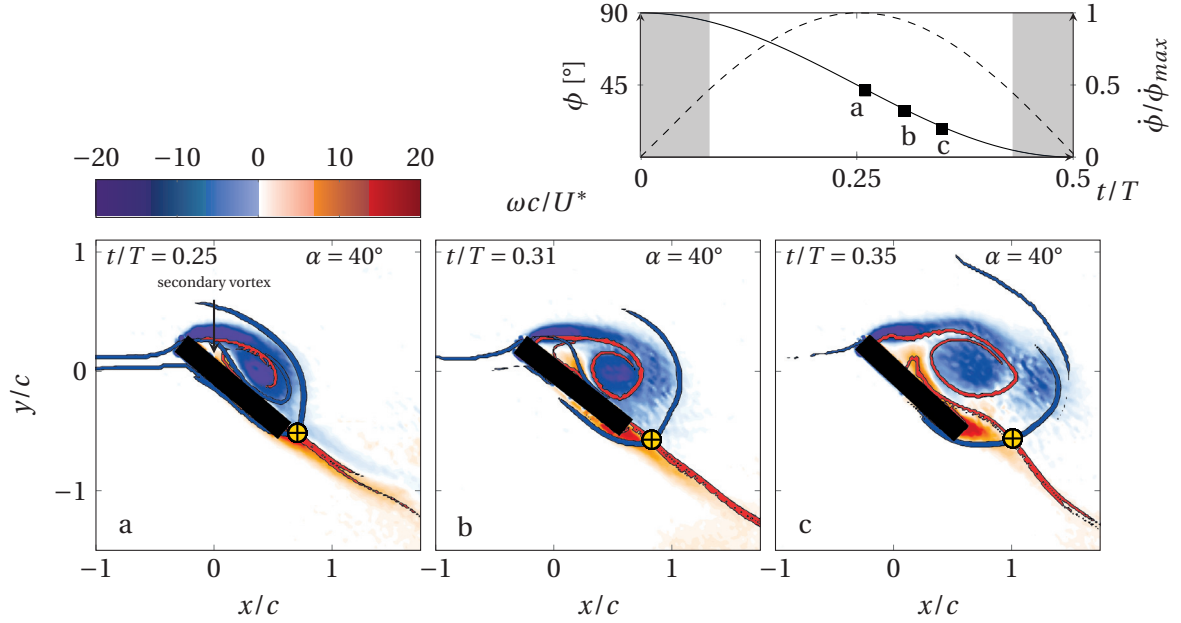


Figure 3.9 – Flow fields showing the LEV lift-off. **nFTLE** and **pFTLE** ridges are overlaid on phase-averaged vorticity fields. Top right: Kinematics (Gray bars indicate period of rotation in the cycle).

tangential velocity along the chord. The velocity on the suction side of the wing is color coded such that the warm colors represent flow from LE to TE and the cold colors represent flow from TE to LE. The velocity moving from the trailing edge to the leading edge increases significantly between  $t/T = 0.25$  and  $t/T = 0.3$  which corresponds to the first half of the lift-off stage. At  $t/T = 0.3$ , a fully reversed surface flow is established that lasts for the rest of the half-stroke. The upward movement of the flow can be observed beginning from quarter-stroke ( $t/T = 0.25$ ) which corresponds to the saddle lift-off from the wing. This finding is consistent with the previous work of Rival et al. [65], where the detachment process of the LEV from the surface of the wing was related to saddle lift-off from the trailing edge. This upward fluid movement results in the formation of a secondary vortex with oppositely signed vorticity (figure 3.9(a)). The secondary vortex pushes the main LEV in the chord-normal direction (figure 3.9(b)-(c)). The presence of the pFTLE ridge between the wing and the LEV signifies that the flow diverges at the ridge and indicates the persistence of the secondary vortex. This secondary vortex also grows normal to the chord in this stage, further pushing the LEV outward (figure 3.9(b)-(c)). A linear increase in the chord normal distance ( $h/c$ ) is observed in this stage (figure 3.4, region ③). The LEV circulation also increases linearly in the LEV lift-off stage at approximately the same rate as the saddle point displacement (figure 3.7—□—).

The vorticity flux at the leading edge decreases after the maximum stroke velocity is reached because the generation of vorticity is dominated by the stroke velocity (figure 3.8). The area of the LEV increases during this stage, exhibiting a recognisable circular shape (figure 3.9(b)-(c)). The lift-off stage ends when maximum circulation is reached. This corresponds to a stroke

### 3.2. Flow development stages for a symmetric flapping cycle

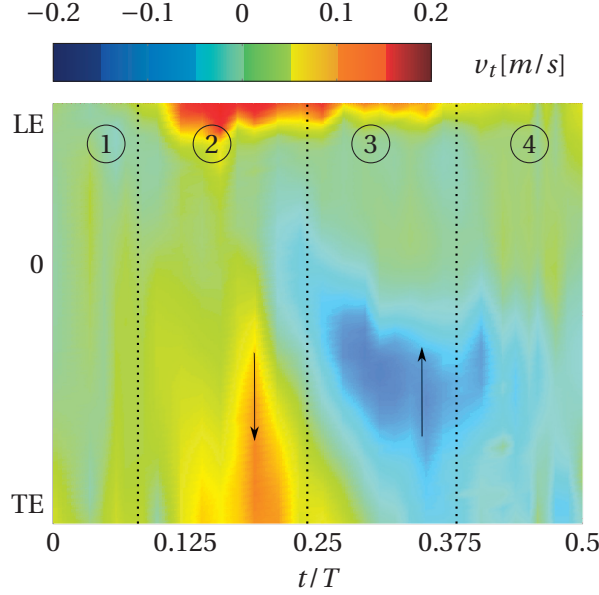


Figure 3.10 – Tangential velocity on the suction side of the wing through half-stroke. Black arrows represent the direction of flow for warm colors (LE to TE) and cold colors (TE to LE). Dotted lines represent the flow stages

velocity that is three-fourths of its maximum value and the wing has travelled for nearly 3.8 convective time scales in the half stroke.

#### 3.2.4 LEV breakdown and decay

The nearly perfect circular structure observed at the end of the lift-off stage undergoes changes due to the decreasing stroke velocity figure 3.11(a) in the fourth and final stage of the flow evolution. As the wing slows down, the LEV spreads in the stroke plane. This corresponds to a convective time scale of 3.8, which is in the range of optimal vortex formation time put forth by Gharib et al.[29]. This is clearly observed in the nFTLE ridge that transforms from a circular boundary to an oval boundary (figure 3.11(b)). The elongated structure then splits when the wing is at about half the maximum stroke velocity, which also corresponds to the end of the pure translation phase in the half-stroke (figure 3.11(c)). As the wing further slows down, the LEV is no longer recognisable as a single, coherent, homogeneous structure. Instead, multiple vorticity concentrations are observed in the flow.

The vorticity concentrations begin to move in different directions and decay as the wing begins its end rotation after traveling over a period of 4 convective time scales. The vorticity concentration closer to the wing moves towards the wing while the outer concentrations move away (figure 3.12(b)-(c)). Even though the area covered by multiple vorticity concentrations is large



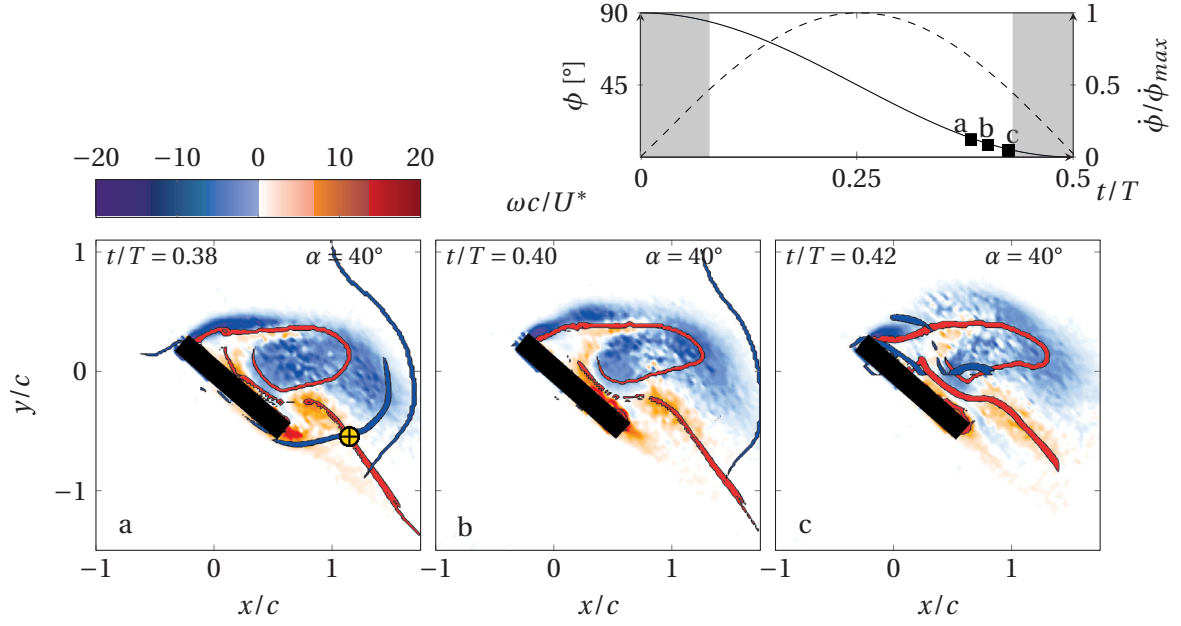


Figure 3.11 – Flow fields showing the LEV breakdown process. **nFTLE** and **pFTLE** ridges are overlayed on phase-averaged vorticity fields. Top right: Kinematics (Gray bars indicate period of rotation in the cycle).

at the end of the half-stroke, the vorticity magnitude is very low, resulting in a decrease in the circulation (figure 3.7  $\square$ ). The flow field near the trailing edge is characterised by a rotational starting vortex due to the combined velocity of the stroke and rotation (figure 3.12(c)). The trailing edge moves in the same direction as the stroke, increasing the local velocity while continuously changing the pitch angle. This results in the generation of vorticity which forms a compact rotational vortex around the trailing edge when the wing has traversed for 4.5 convective time scales in the half-stroke. The shed LE and TE vorticity decays and disintegrates in the flow field at the end of the stroke (figure 3.12). The end of this stage is marked by the complete breakdown of the LEV. The life cycle of the flow features lasts up to nearly 5 convective time scales.

### 3.2.5 Influence of flow development on forces

Forces obtained from direct measurements are normalised with  $\frac{1}{2}\rho U^{*2}S$ , where  $S$  is the area of the wing, to obtain the lift and drag coefficients. The evolution of aerodynamic force coefficients during the half-stroke shows a strong dependence on the stroke velocity (figure 3.13). The LEV emergence stage (region ①), is characterised by a near linear increase in the lift coefficient. A change in the gradient is observed at  $t/T = 0.08$ , which corresponds to the end of the wing rotation, marking the onset of the LEV growth stage (region ②). The lift continues to increase sinusoidally in the second stage, which can be associated with the



### 3.2. Flow development stages for a symmetric flapping cycle

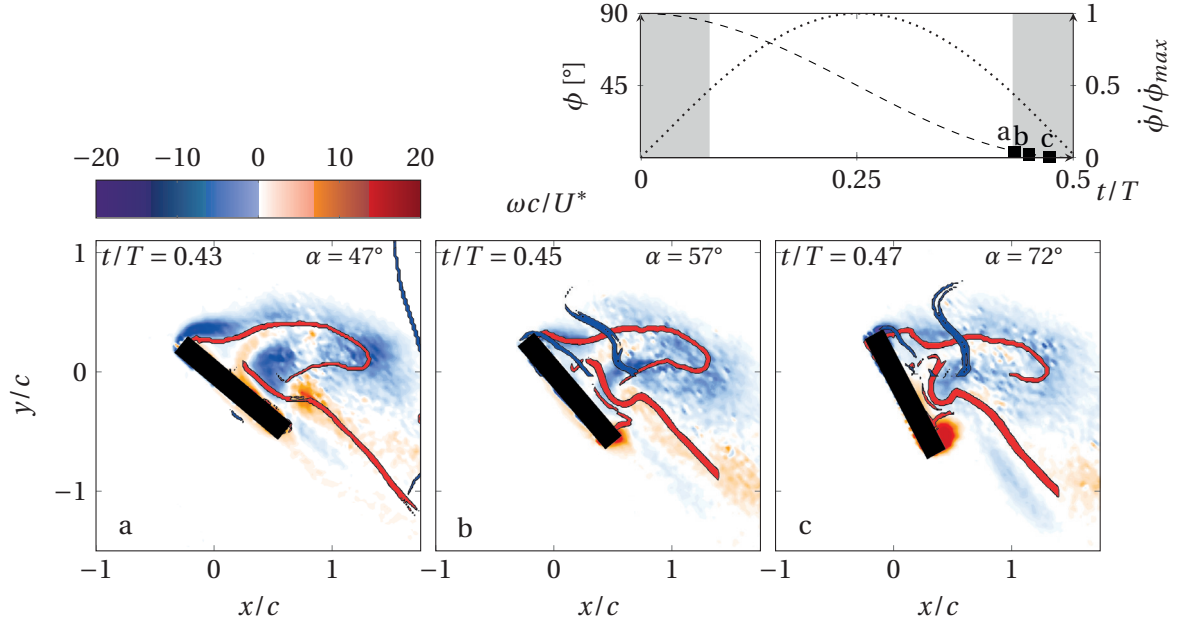


Figure 3.12 – Flow fields showing the LEV decay process. nFTLE and pFTLE ridges are overlaid on phase-averaged vorticity fields. Top right: Kinematics (Gray bars indicate period of rotation in the cycle).

increasing leading edge vorticity flux (figure 3.8). The maximum lift coefficient is reached at  $t/T = 0.24$ , which indicates that the prominent contribution to the lift comes from the bound LEV in the growth stage. The LEV lifts off of the surface soon thereafter at maximum stroke velocity allowing reverse surface flow (region ③). As the vorticity flux decreases (figure 3.8), less lift is generated. The lift decreases sinusoidally in the third and fourth stage of the flow cycle until the wing rotates ( $t/T = 0.42$ ). A change in the gradient similar to the one at the end of the first stage is observed when rotation begins (region ④).

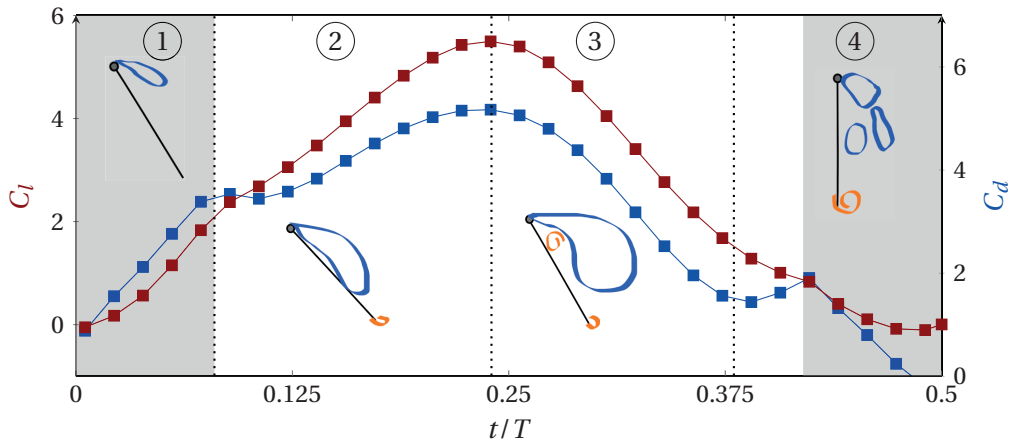


Figure 3.13 – Lift (—■—) and drag (—■—) coefficients over a half-stroke.

The drag also reaches a maximum at maximum stroke velocity at  $t/T = 0.24$ , just before LEV lift-off. While the effect of rotation is less prominent in the lift production, the drag is affected noticeably at the end of the first rotation (region ①) and at the start of the second rotation (region ④). The first stage of the cycle shows a steep linear rise in the drag whereas the pure translation part of the cycle shows a sinusoidal pattern that is mostly the second and third stage of the flow cycle (region ②, ③). During the LEV emergence stage (region ①), the drag increases at a rate approximately 3 times faster than that of the growth and lift-off stages. The large slope of the drag during rotation can be attributed to the large angles of attack of the wing which behaves like a bluff body. The drag during the first stage is larger than the drag during the final stage due to the fact that the wing is accelerating in the stroke plane during first rotation and decelerating at the end of the half-stroke. The bluff-body-like dynamics during acceleration in a quiescent fluid results in higher drag.

### 3.3 Influence of rotational phase for fast wing rotation

The flow development stages in the case of a hovering wing where the wing rotated symmetrically about the stroke reversal for one-sixth of the period in each half-stroke has been discussed in section 3.2. The flow fields exhibited a single large lift enhancing LEV, a translational starting vortex and a rotational starting vortex. Although the evolution of the LEV is predominantly dependent on the stroke velocity, the wing rotation at the beginning and the end of the half-stroke contribute to the change in the vortex dynamics. This motivates the next question : What is the influence of the rotational phase on the vortex dynamics of hovering flight?

The timing of wing rotation is the phase relationship between the wing rotation and the stroke, denoted by the phase-shift,  $\Delta t_s$ . The changes in phase with respect to the zero phase-shift during symmetric rotation are distinguished as advanced and delayed rotation. In the current chapter, two incremental phase-shifts for each advanced and delayed rotations are investigated, for a rotational duration of  $T_f = T/6$ . A comparison of the effects of an early or late wing rotation with respect to the symmetric rotation is provided. Quantitative force comparisons are correlated with the vortex dynamics. The key similarities and differences in different cases are highlighted.

### 3.3.1 Advanced rotation

#### Kinematics

In advanced rotation case, the wing rotates partly or all the way before the stroke reversal ( $t/T = 0.5$ ). The wing starts to move in each half-stroke with a positive geometric angle of attack. The angle of attack is related to the pitch angle as  $\alpha = 90^\circ - \beta$ , where  $\beta$  is the rotational angle with respect to the vertical.  $\alpha$  is considered negative when  $\alpha > 90^\circ$ . The wing rotation is advanced by 4% and 8% of the total time period. Or in other words, the wing rotation has a lead with respect to the stroke. This is compared with the symmetric rotation case ( $\Delta t_s = 0$ ). A schematic of the starting positions of the wing in the rotational plane are illustrated in figure 3.14. In the fully advanced rotation ( $\Delta t_s = -\frac{T_f}{2}$ ), the wing has completed rotating at the beginning of the half-stroke and moves in the stroke plane at a geometric angle of attack,  $\alpha = 40^\circ$ . The partially advanced rotation case ( $\Delta t_s = -\frac{T_f}{4}$ ) has rotated half way through, up to  $\alpha = 65^\circ$  at the beginning of the half-stroke. Through out this section, symbols assigned to the fully advanced rotation (■), partly advanced rotation (▣) and symmetric rotation (□) are used to differentiate the cases.

#### Flow development : details

#### LEV emergence

The first stage of the flapping cycle is characterised by the accumulation of vorticity at the leading edge, which manifests as an unbound LEV and grows in the chord-normal direction. A comparison of the flow structures at the end of the first stage for all three cases is presented in figure 3.15. Phase-averaged vorticity fields are shown for fully advanced, partly advanced and symmetric rotations. The time instant at which the flow fields are shown on the top left corner of each case. Despite the difference in starting rotational angles as the wing accelerates

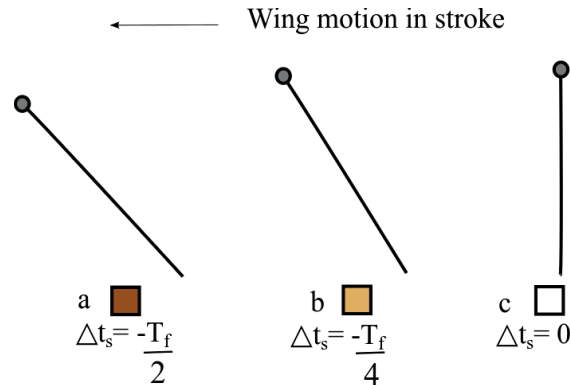


Figure 3.14 – The rotational position of the wing at the beginning of each half stroke at  $t/T = 0$  in (a) fully advanced rotation (b) partly advanced rotation (c) symmetric rotation. The wing moves to the left.

### 3.3. Influence of rotational phase for fast wing rotation

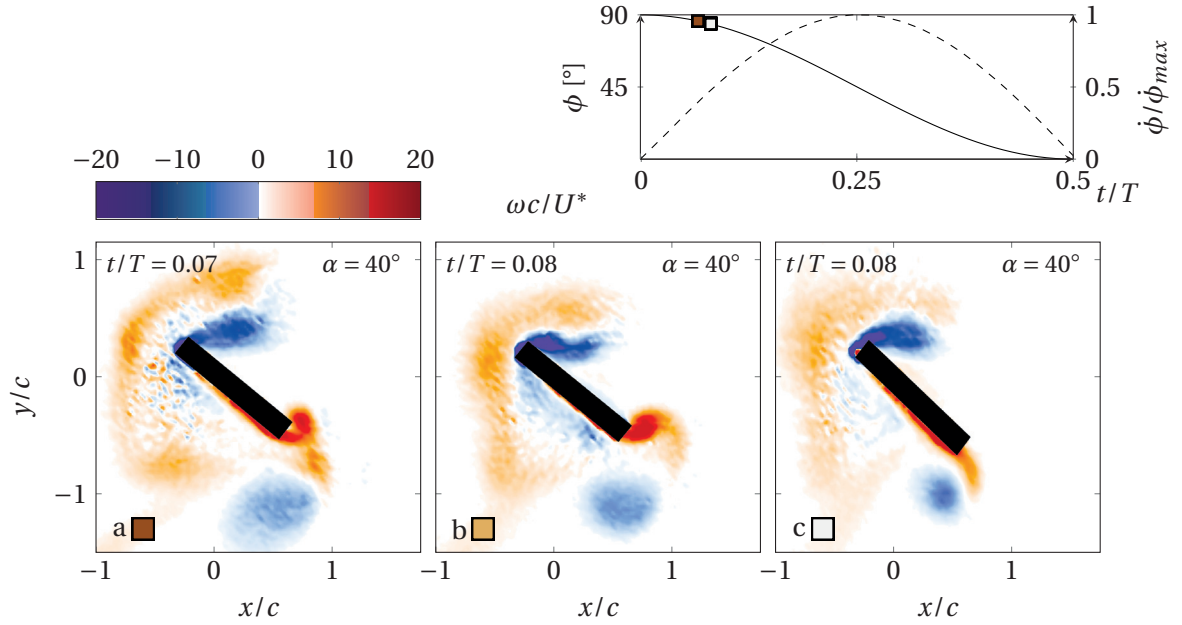


Figure 3.15 – Flow fields showing the end of LEV emergence stage for (a) fully advanced (b) partly advanced (c) symmetric rotations. Top right: Stroke position (—) and stroke velocity (---) of the half-stroke with the corresponding time instants.

in the stroke plane, a similar LEV emerges in both advanced rotation cases as compared to the symmetric rotation (figure 3.15(a),(b)). In each case, the wing moves through a region of remnant vorticity from the previous stroke. The strength and area of this remnant vorticity varies for each case. The fully advanced rotation (figure 3.15 a ■) shows a larger and stronger region of remnant vorticity compared to the partly advanced rotation (figure 3.15 b ■). This follows from the history of wing motion and thereby the flow structures in the fully advanced rotation.

In the previous half-stroke the wing begins to rotate much earlier than the symmetric rotation; when the stroke velocities are also higher (figure 3.16). Top row of this figure shows the vorticity fields at the end of the previous half-stroke, when the wing begins to rotate and the bottom row shows flow fields at nearly the end of the previous cycle. This is intended to show the variation in the way flow develops at the end of the previous half-stroke due to difference in the kinematics. In the fully advanced rotation, the wing begins to rotate at a high stroke velocity of 80% of the maximum, when the flow structures on the suction side are just beginning to split (figure 3.16 a ■). The strength of the structures are relatively high. In comparison, the LEV has split into multiple concentrations with lower vorticity in the partly advanced (figure 3.16 b ■) and the symmetric (figure 3.16 c ■). The stroke velocity is close to 50% of the maximum when the rotation begins and is closer to the stroke reversal in these two cases. The variation in the strength of the shed structures is noticeable at the end of the previous half-stroke (figure 3.16 (d ♦), (e ♦), (f ♦)). The end of the previous half-stroke leaves behind a recognisable circular rotational starting vortex in all three cases whereas the

LEV has split into multiple concentrations. The rotational vortices in the advanced cases are stronger and larger compared to that of the symmetric rotation. The trailing edge moves with a relatively high velocity in the advanced cases due to the combined stroke and rotational velocity, thus feeding more vorticity into the structure. The secondary vortex from the previous half-stroke is observed as a small concentration that is trapped between the oppositely signed LEV concentrations.

The newly emerged LEV in the subsequent half-stroke moves with the wing in this remnant vorticity and grows in the chord-normal direction (figure 3.15). The chord-normal height is again calculated as the distance between the chord and the outermost point of the nFTLE ridge that forms the boundary of the LEV and is quantified in figure 3.17. The chord-normal height increases in the LEV emergence stage, reaching a maximum height at the same time instant ( $t/T = 0.08$ ) for partly advanced and symmetric rotation cases (figure 3.17 —■—, —□—).

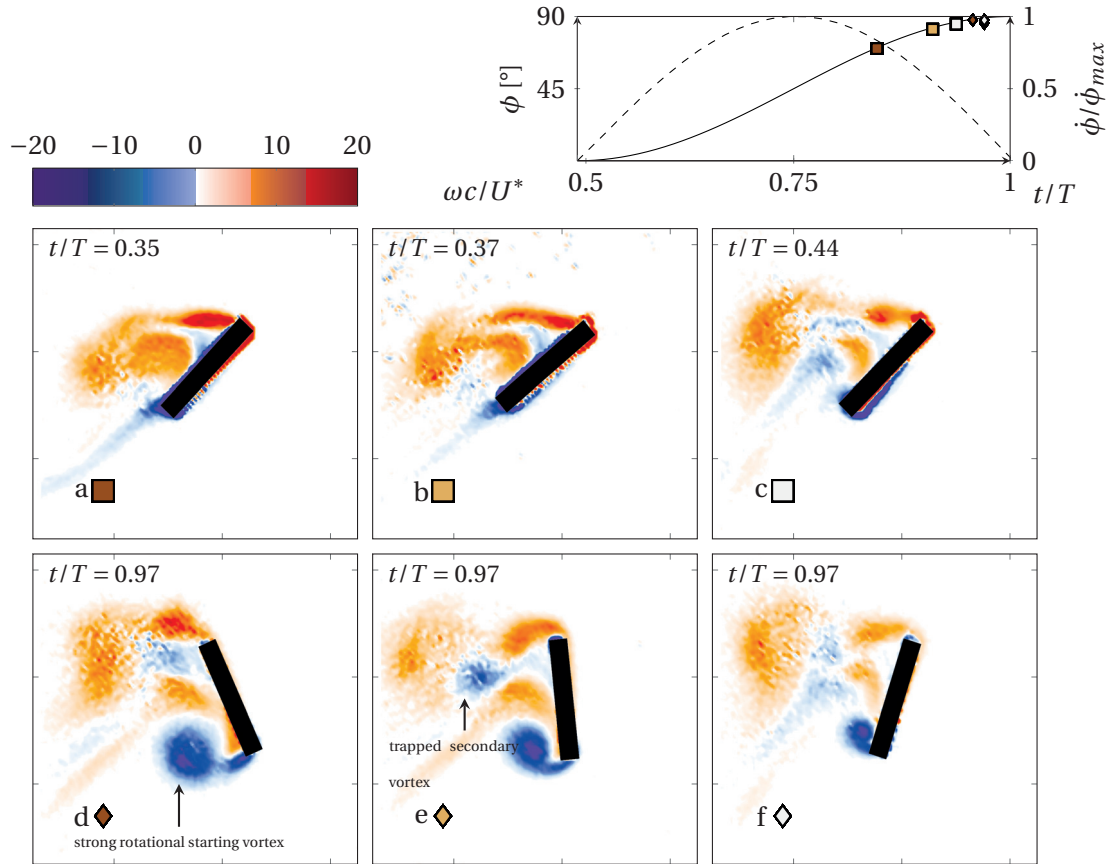


Figure 3.16 – Top row: Flow fields showing the LEV features near the end of the previous half-stroke when the wing begins to rotate. Bottom row: Flow fields showing the LEV features at the end of the previous half-stroke. (a,d) fully advanced (b,d) partly advanced (c,f) symmetric rotations. Top right: Stroke position (—) and stroke velocity (---) of the half-stroke with the corresponding time instants.

### 3.3. Influence of rotational phase for fast wing rotation

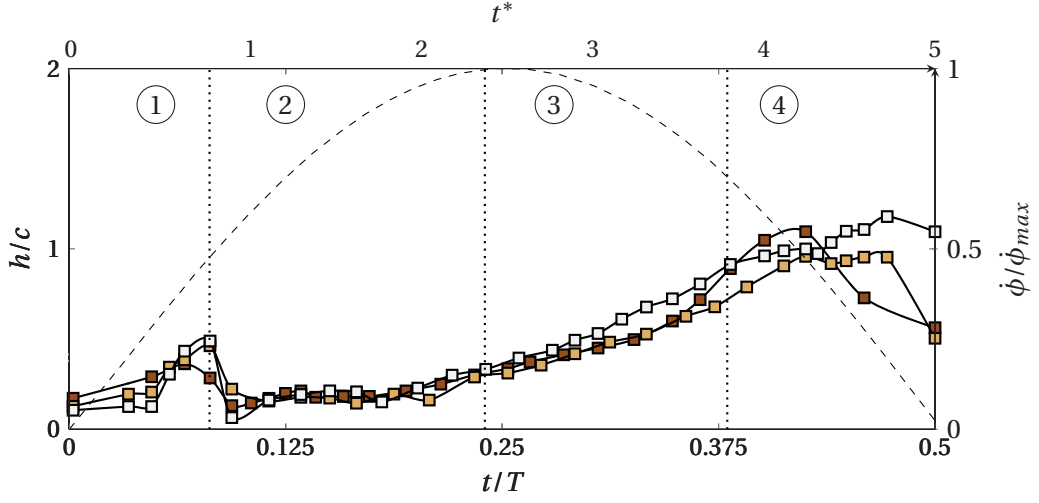


Figure 3.17 – Chord-normal height of the leading edge vortex for fully advanced (—■—), partly advanced (—◐—), and symmetric rotation(—□—). Top x-axis shows the convective time scale ( $t^*$ ).

This occurs at about 50% of maximum stroke velocity. For the fully advanced rotation, the emergence stage ends slightly earlier at  $t/T = 0.07$ , which is marked by the emergence of the pFTLE ridge.

The advanced rotations show higher circulation in the LEV emergence stage compared to the symmetric rotation (figure 3.18, region ①). This correlates with the large local peak seen in the leading edge vorticity flux in the first stage (figure 3.19—■—). The large vorticity flux in the advanced case is due to the wing surging through the fluid at a relatively smaller  $\alpha$ . This

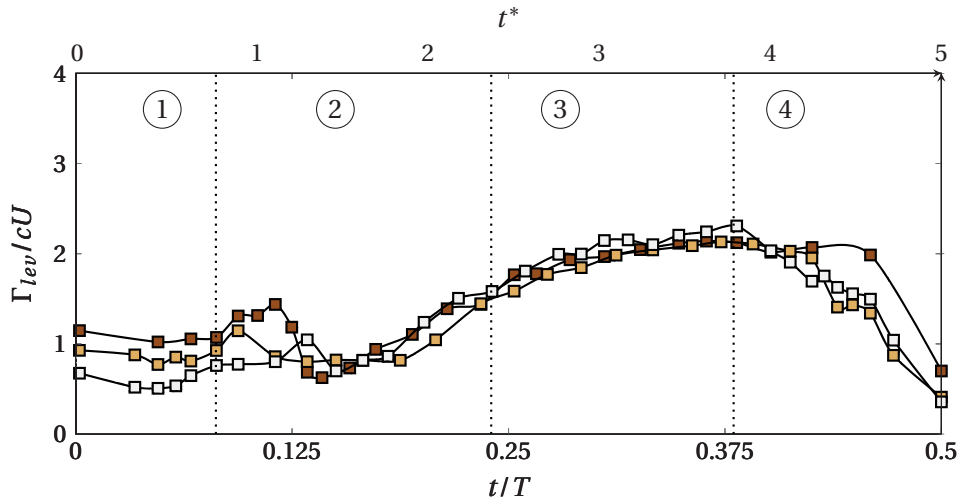


Figure 3.18 – LEV circulation for fully advanced (—■—), partly advanced (—◐—), and symmetric (—□—) rotations. Top x-axis shows the convective time scale ( $t^*$ ).

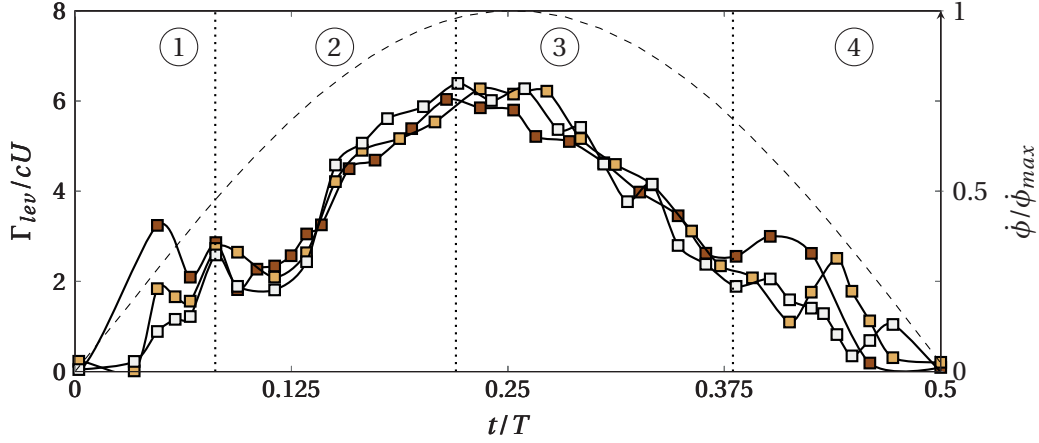


Figure 3.19 – Vorticity flux for fully advanced  $\blacksquare$ , partly advanced  $\square$ , and symmetric  $\square$  rotations

combined with a spread LEV leads to an overall higher circulation in the fully advanced case. The vorticity flux is the least in the symmetric rotation, due to the disruption in the form of the leading edge motion at the beginning of the cycle (figure 3.19- $\square$ ).

Like for symmetric rotation, the end of the emergence stage is characterised by an unbound LEV that varies in vorticity magnitude. At the trailing edge, it is observed that a rotational starting vortex is seen in the advanced rotation cases unlike the symmetric rotation. The shed TEVs from the previous half-strokes, still persist at the end of the LEV emergence stage in all three cases. However the size of the previously shed TEV decreases from fully advanced to symmetric rotation.

### LEV growth

The second stage in the flow development is characterised by the binding of the LEV on the suction side of the wing and its growth along the chord. The unbound LEV that is seen at the end of the emergence stage in all three rotations now moves towards the surface of the wing. The similarity in the binding process is supported by the fact that the chord normal height in all the three cases are nearly the same (figure 3.17, region (2)).

The half saddle ( $\blacktriangle$ ) on the surface of the wing emerges soon after the emergence stage at  $t/T \approx 0.1$  heralding the onset of the LEV growth stage. The full-saddle ( $\oplus$ ) is identified as the intersection of pFTLE and nFTLE ridge that binds the LEV. The movement of these saddles indicate the LEV binding process and is quantified by the saddle distance ( $s/c$ ) from the axis of rotation for each wing rotation. This saddle evolution is presented in the top most row of figure 3.20.

The saddle movement in the advanced rotation cases are remarkably similar to that of the symmetric rotation. The full and half saddle merge soon after the end of the first stage, move



### 3.3. Influence of rotational phase for fast wing rotation

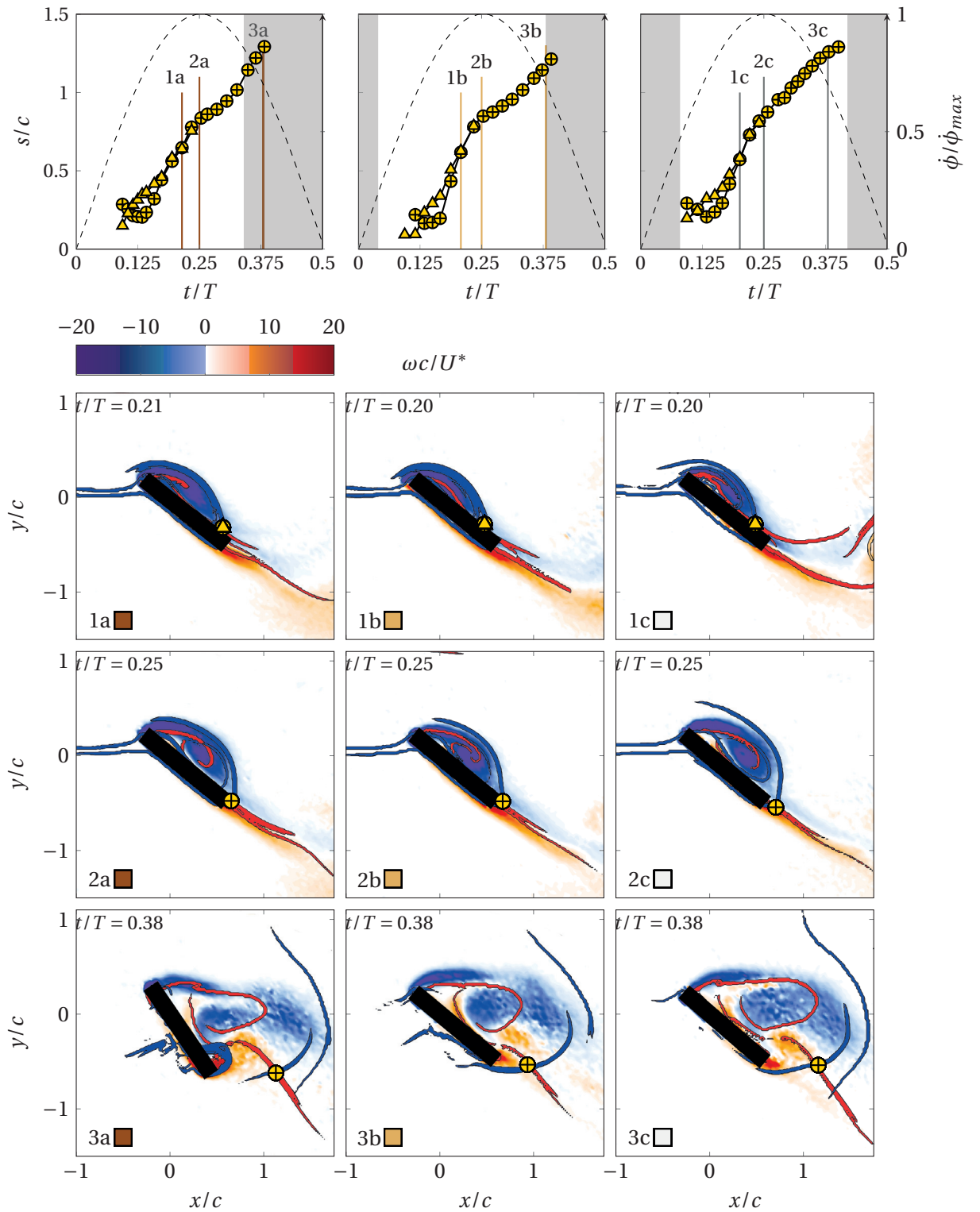


Figure 3.20 – Top row: Saddle distance evolution for (a) fully advanced (b) partly advanced (c) symmetric rotations, including stroke velocity (---). Gray areas indicate rotation. Corresponding flow fields at time instants when, row 1: saddles merge, row 2: saddle, thereby LEV lifts-off, row 3: End of LEV lift-off stage.

towards the trailing edge and eventually merge; similar to the base case figure 3.6. The full and half-saddles merge at  $t/T = 0.21$  for fully advanced rotation (figure 3.20(1a■)) and at  $t/T = 0.2$  for partly advanced and symmetric rotation (figure 3.20(1b■, 1c■)). The stroke velocity is about 94% of the maximum at this instant. This merged half-saddle moves towards the trailing edge. The end of the LEV growth stage is characterised by a fully bound LEV that has grown over the chord-length in all three cases.

The starting vortex observed in the advanced rotations has convected away by the end of the second stage and no other trailing edge features are formed. This is in contrast to the symmetric rotation where the second stage is marked by a translational vortex which convects away by the end of the second stage. This is related to the starting rotational angles of the wing. At the start of the LEV growth stage, the pure translation phase of the half-stroke has just begun in symmetric rotation whereas in the advanced rotations, the wing is well into the translation phase.

The LEV circulation is higher in the fully advanced rotation compared to the other cases at the start of the second stage (figure 3.18 —■—, region (2)). This follows from the first stage where the advanced rotation showed the highest vorticity flux and LEV circulation due to the favourable angle of attack. The LEV circulation in the fully advanced case drops to a minimum at  $t/T \approx 0.15$ , after which it increases nearly linearly until the end of the third stage. This minimum circulation also corresponds to the instant at which the full-saddle is the closest to the axis of rotation (figure 3.20 (top row (a) ⊕)). Noting that the vorticity flux continues to increase in the second stage (figure 3.19, region (2)), this dip in LEV circulation and decreased saddle distance indicates that the LEV is a compact and bound feature on the wing, smaller in size compared to the unbound LEV seen in the first stage. This fact however, does not affect the evolution of the saddles in the flow and all three cases exhibit similar growth process, traversing the full chord length at  $t/T = 0.24$ , signifying the end of the growth stage.

#### LEV lift-off

The merged saddle lifts-off from the trailing edge at maximum stroke velocity ( $t/T = 0.25$ ) in all three cases, transitioning into the third stage of the flow development (figure 3.20(row 2)). The lifting of the saddle signifies the beginning of a reverse flow from the trailing edge to the leading edge. A secondary vortex between the wing and the LEV becomes visible at lift-off in all the three rotations.

The backflow along the chord can be better visualised by the tangential velocity plot where the time-wise variation of the velocity along the chord is presented (figure 3.21). The magnitude of the reverse flow just after lift-off is only slightly lower in the advanced rotation cases (figure 3.21 a ■, b ■) as compared to the symmetric rotation (figure 3.21 c ■). The continuous upward fluid movement after LEV lift-off is consistent with the backflow region between the wing and the main LEV resulting in the formation of a secondary vortex with oppositely signed vorticity, as seen in figure 3.20(row 2). Given that the LEV evolves similarly, the effect on the fluid at the

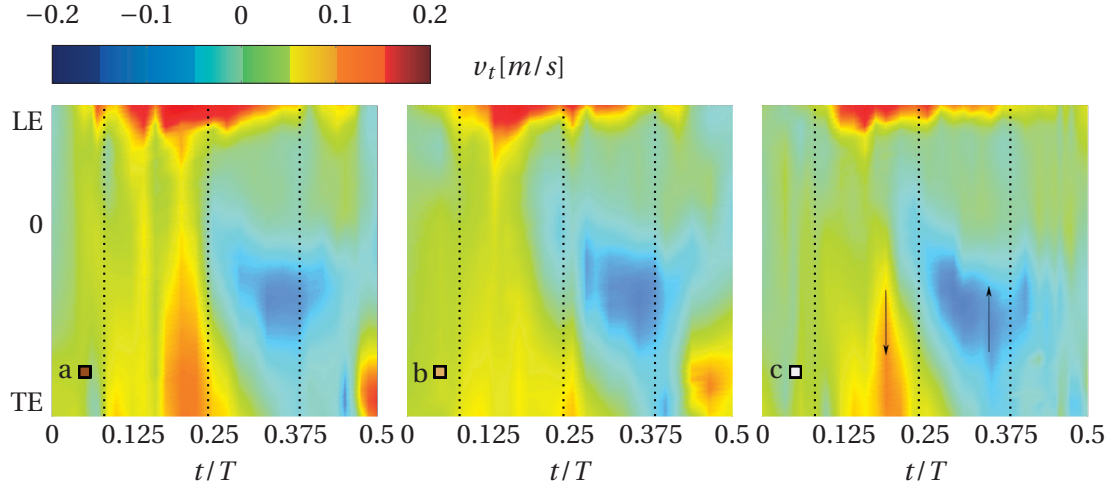


Figure 3.21 – Tangential velocity on the suction side of the wing through half-stroke for (a) fully advanced, (b) partly advanced, and (c) symmetric rotations. Black arrows represent the direction of flow for warm colors (LE to TE) and cold colors (TE to LE). Dotted lines represent the end of flow stages.

wing is nearly the same.

The LEV circulation continues to increase almost linearly after the LEV lift off despite a decreasing vorticity flux (figure 3.19, region ③). The LEV circulation reaches a maximum at  $t/T \approx 0.38$  (figure 3.18, region ③). This marks the end of the LEV lift-off stage, which corresponds to 3.8 convective time scales. The end of the LEV lift-off stage is again characterised by a recognisably circular structure on the suction side of the wing on the verge of splitting in the partly advanced and symmetric rotations (figure 3.20 3b ■, 3c ■). In the fully advanced rotation the wing has begun rotating resulting in a visibly split LEV concentrations (figure 3.20 1a ■). In all the rotations, the LEV is detached from the wing, which can be observed by the nFTLE ridge between the wing and the LEV that differentiates dynamically different regions. The full saddle (⊕) moves away from the wing at approximately the same rate in all three cases. The saddle rates will be discussed in detail at the end of the flow comparisons of both advanced and delayed rotations.

#### LEV breakdown and decay

The nearly perfect circular structure observed at the end of the lift-off stage undergoes changes due to the decreasing stroke velocity in the fourth and final stage of the flow evolution. As the wing slows down, the LEV spreads in the stroke plane and splits into multiple vorticity concentrations during this stage (figure 3.22). Despite the difference in the rotational angles at this stage of the cycle, the flow features are remarkably similar, although varying in vorticity strength. The fully advanced rotation shows stronger vorticity concentrations compared to that of the other cases (figure 3.22 a ■). The advanced rotations show a strong trailing edge

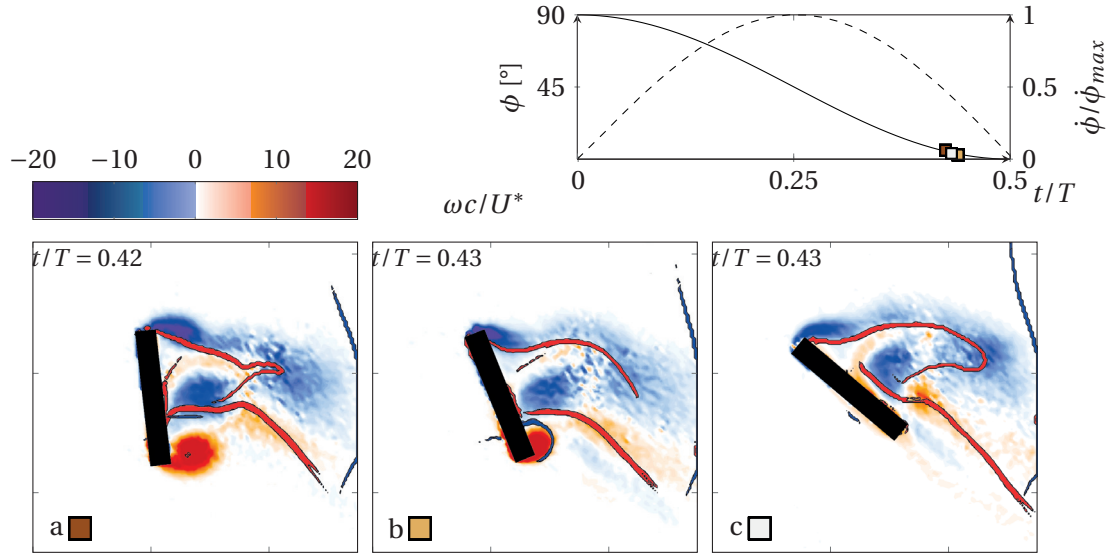


Figure 3.22 – Flow fields showing the LEV breakdown and decay stage for (a) fully advanced, (b) partly advanced, and (c) symmetric rotations. Top right: Stroke position (—) and stroke velocity (---) of the half-stroke with the corresponding time instants.

vortex unlike the symmetric rotation. This behaviour in the advanced rotation follows from the higher velocity at the leading and the trailing edge due to the combined rotation and stroke motion in a direction opposite to that of the stroke. In comparison, the wing has just begun to rotate in the symmetric rotation.

The LEV circulation in all cases decreases in this final stage of the flow cycle due to decaying vorticity (figure 3.18). However, the fully advanced rotation (—■—) is characterised by slightly higher vorticity flux (figure 3.19) and higher circulation (figure 3.18), compared to that of the symmetric rotation. This is because the in the fully advanced rotation the wing begins to rotate earlier, when the stroke velocities are higher. The combined rotational and stroke velocity at the leading edge is higher in the fully advanced case, which results in higher vorticity flux, thereby circulation.

#### 3.3.2 Delayed rotation

##### Kinematics

In delayed wing rotation cases, the wing rotates most or all the way after the stroke reversal. The wing starts in each half-stroke at  $\alpha > 90^\circ$ , i.e. at a negative angle of attack. For the same duration of wing rotation, the wing rotation is delayed by 4% and 8% of the total time period with respect to the stroke motion. This is compared with the symmetric rotation case ( $\Delta t_s = 0$ ). In both delayed rotation cases, the wing is yet to complete rotating more than half of the total wing rotation at the beginning of each half-stroke. Or in other words, the wing rotation has a lag with respect to the stroke. A schematic of the starting positions of the wing in the rotational plane are illustrated in figure 3.23. In the fully delayed rotation case ( $\Delta t_s = +\frac{T_f}{2}$ ), the wing is yet to begin rotation in the new half-stroke and rotates from  $\alpha = 140^\circ$  to  $\alpha = 40^\circ$ . The partially delayed rotation case ( $\Delta t_s = +\frac{T_f}{4}$ ) has rotated up to  $\alpha = 115^\circ$  at the start of the half-stroke. Through out this chapter, symbols assigned to the fully delayed rotation (■), partly delayed rotation (▣) and symmetric rotation (□) are used to differentiate the cases.

##### Flow development : details

##### LEV emergence

The first stage of the flow cycle in the delayed rotations are characterised by a slight delay in the emergence of the LEV (figure 3.24(a)-(c)). The negative angle of attack in the delayed cases combined with low stroke velocity inhibits the accumulation of vorticity at the leading edge at the very beginning of the half-stroke. The LEV emerges earliest in the symmetric rotation (figure 3.24(c) ◇) because the wing attains a positive geometric angle of attack sooner than the delayed rotation cases. The other notable aspect at the commencement of the stroke is the distribution of the remnant vorticity around the wing. In the partly delayed (figure 3.24 ◆)

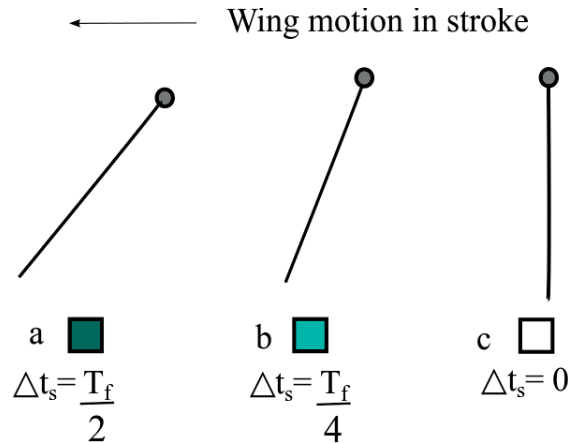


Figure 3.23 – The rotational position of the wing at the beginning of the half-stroke at  $t/T = 0$  in (a) fully delayed (b) partly delayed (c) symmetric rotations.

and symmetric (figure 3.24 c  $\diamond$ ) cases, the vorticity is more dispersed around the wing. The remnant vorticity accumulates much closer to the wing and in a more compact manner in the fully delayed rotation (figure 3.24 a  $\blacklozenge$ ). This is because of the lack of rotation at the end of the previous stroke where the split LEV is not disturbed by the wing. The wing pushes all of the suspended vorticity along with it in the new half-stroke as it rotates and accelerates in the stroke plane. The arc like motion of the rotating leading edge when the stroke velocity is increasing results in an unbound LEV that is entrained along the trajectory of the leading edge (figure 3.24(d  $\blacksquare$ ), (f  $\blacksquare$ )). The emergence of the pFTLE ridge marks the end of the emergence stage, which is delayed as the rotational delay increases (figure 3.24 (bottom row)). The end of the LEV emergence stage in delayed rotation is characterised by an unbound LEV with a larger chord-normal height (figure 3.25  $\blacksquare$ ,  $\blacksquare$ ). The first stage lasts longer in the delayed rotations at  $t/T = 0.11$  (figure 3.24  $\blacksquare$ ,  $\blacksquare$ ) than the symmetric rotation ( $t/T = 0.08$ ) (figure 3.24  $\square$ ).

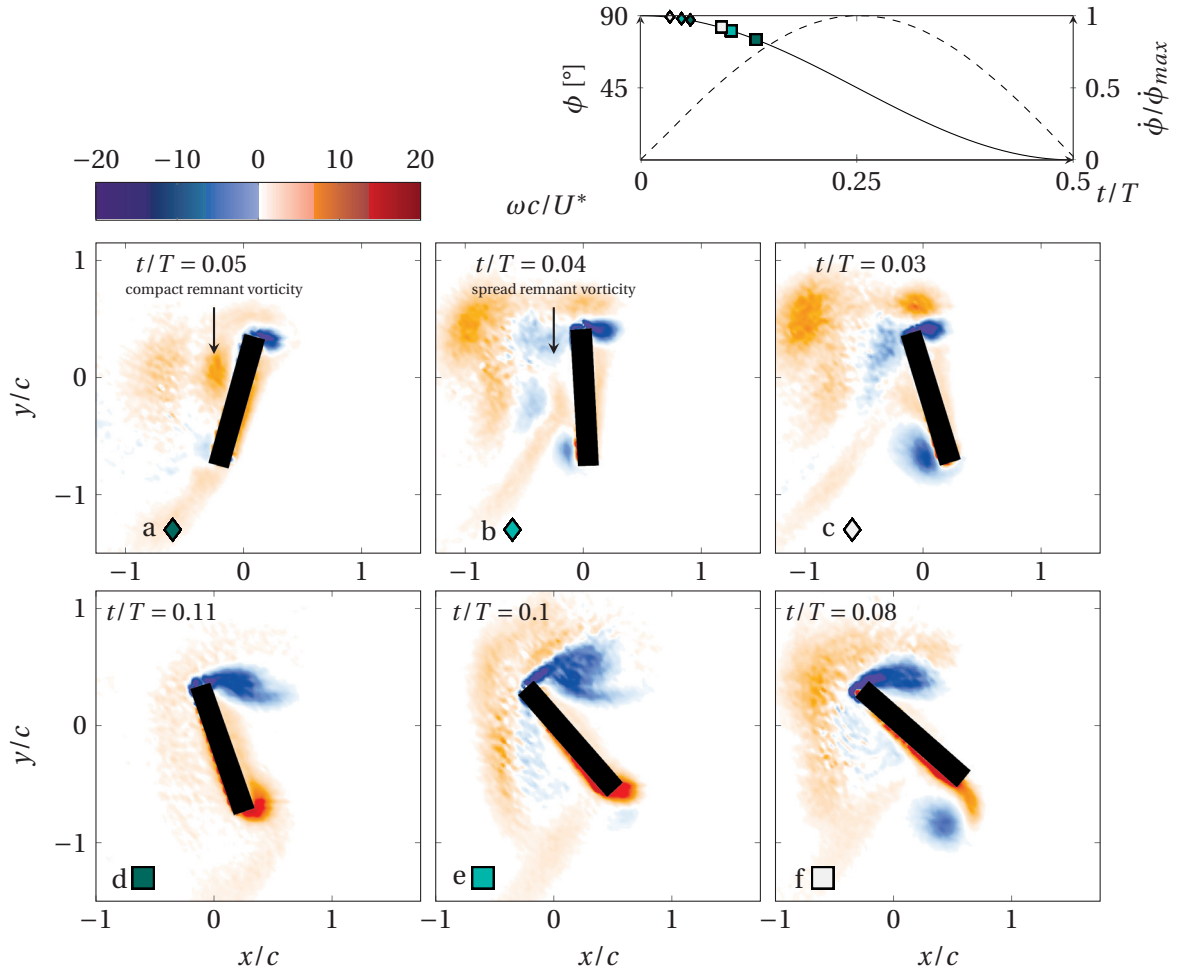


Figure 3.24 – Flow fields showing LEV emergence stage for (a,d) fully delayed, (b,e) partly delayed, and (c,f) symmetric Top row: Start of LEV emergence stage. Bottom row: End of LEV emergence stage. Top right: Stroke position (—) and stroke velocity (---) of the half-stroke with the corresponding time instants.

### 3.3. Influence of rotational phase for fast wing rotation

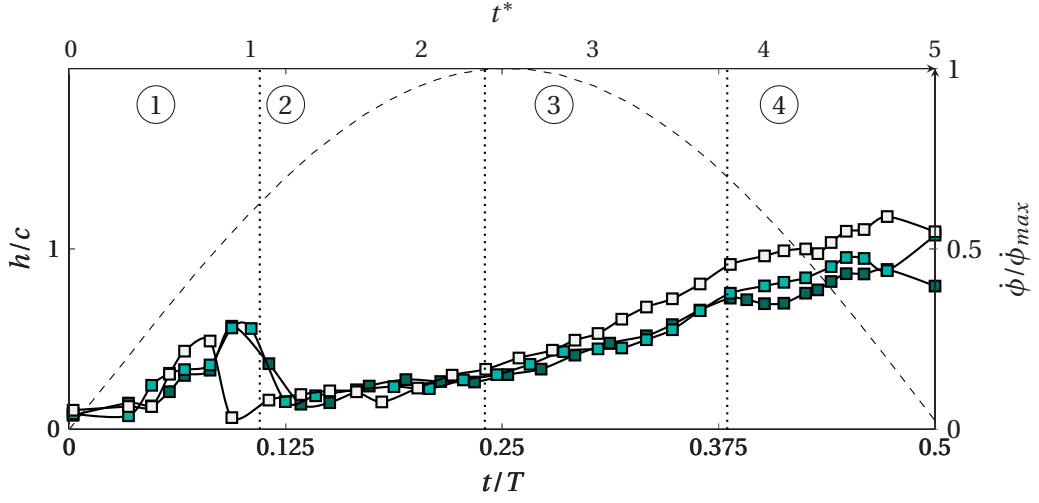


Figure 3.25 – Chord-normal height of the leading edge vortex for fully delayed ( $\blacksquare$ ), partly delayed ( $\blacksquare$ ) and symmetric ( $\square$ ) rotations. Top x-axis shows the convective time scale ( $t^*$ ).

The LEV circulation is relatively low in the delayed rotations than in the symmetric rotation at the start of the half-stroke (figure 3.26). This corresponds to the lower vorticity generated in the delayed rotation cases due to the negative  $\alpha$  (figure 3.27). This follows from the fact that the LEV emergence is delayed and its strength is affected by the wing rotation.

#### LEV growth

The LEV growth stage is similar to the symmetric rotation where the unbound LEV from the first stage moves towards the wing and binds to it. The saddle distance is tracked as before and presented in the top row of figure 3.28 for fully delayed ( $\blacksquare$ ), partly delayed ( $\blacksquare$ ) and symmetric ( $\square$ ) rotations.

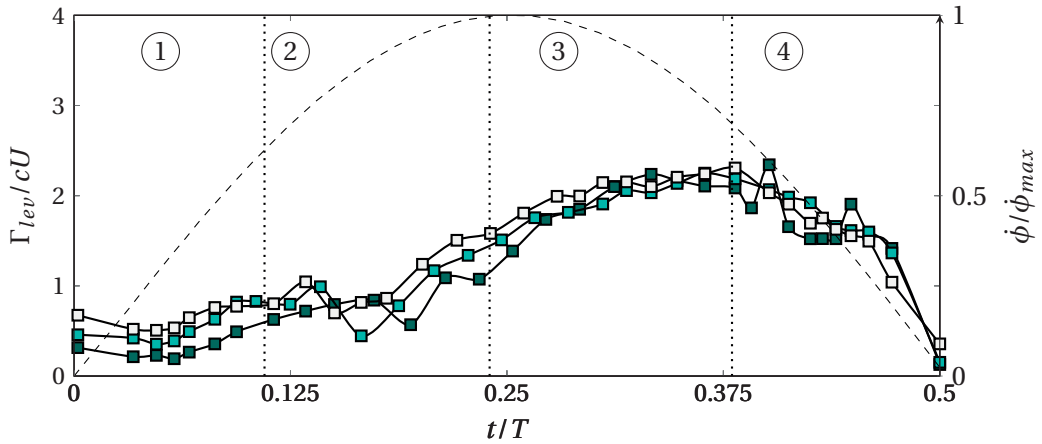


Figure 3.26 – LEV circulation for fully delayed,  $\blacksquare$ , partly delayed,  $\blacksquare$ , and symmetric  $\square$  rotations. Top x-axis shows the convective time scale ( $t^*$ ).



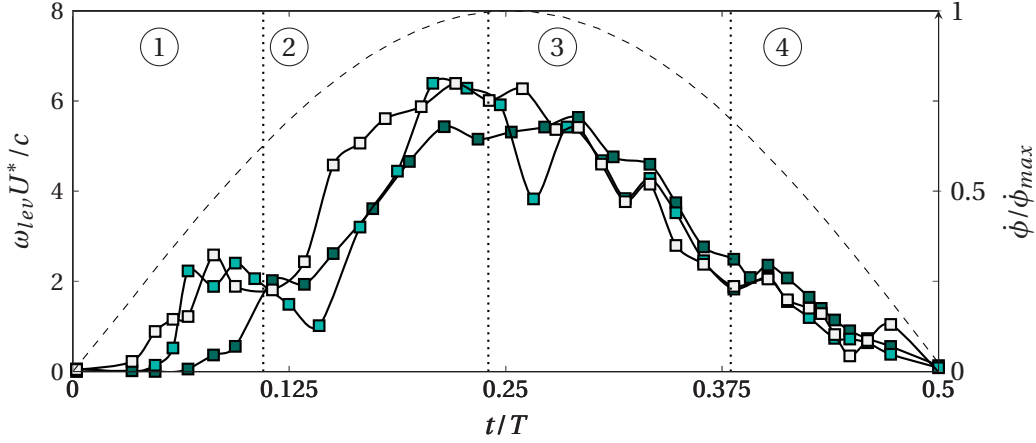


Figure 3.27 – Vorticity flux for fully delayed  $\blacksquare$ , partly delayed  $\blacksquare$ , and symmetric  $\blacksquare$  rotations.

rotation ( $\blacksquare$ ). The flow fields at crucial instances are shown in the same figure. The onset of the second stage is characterised by the emergence of the half saddle at the wing surface and full saddle identified by the intersection of the nFTLE and pFTLE ridge. A deviation from all other cases so far in terms of the saddles merging is the fully delayed rotation ( $\blacksquare$ ). The pFTLE ridge does not intersect on the surface of the wing for most of growth stage in this case. In the fully delayed rotation, the saddles do not seem to merge before the LEV lift-off stage (figure 3.28 (1a, 2a)). For the partly delayed and symmetric rotations, the merging of the full and half saddle are shown in figure 3.28(1b  $\blacksquare$ , 1c  $\blacksquare$ ). Due to the delay in the formation of the LEV and the end of the emergence stage in the partly delayed rotations, the saddles merge at a later instant compared to the symmetric rotation (figure 3.28(1b  $\blacksquare$ , 1c  $\blacksquare$ )). The fully delayed rotation is also characterised by a trailing edge vortex that convects away from the wing.

### LEV lift-off

The LEV lifts-off at  $t/T = 0.25$ , similar to the symmetric and advanced rotations. The lift-off subsequently lifts the LEV off the surface, inducing a reverse flow. A small region of secondary vorticity is observed between the wing and the LEV which pushes out the primary LEV. In the fully delayed rotation, the full saddle continues to exist after the growth stage and at lift-off of the half-saddle from the trailing edge (figure 3.28 (2a)). This provides additional proof that the LEV lift-off is governed by the stroke velocity. The recognisably circular LEV continues to enlarge in this stage reaching a maximum size and thereby circulation at  $t/T = 0.36$  in the delayed rotation cases, only slightly after the symmetric case. Clear presence of the secondary vortices is observed in all the cases. The onset of the reverse flow and formation of secondary vortices is shown in figure 3.29 through the tangential velocity along the chord. The velocity plots of the delayed rotation are remarkably similar to each other. They do show stronger velocity at the leading edge during the growth stage (figure 3.29 (a),(b)) as compared to the symmetric rotation (figure 3.29(c)).



### 3.3. Influence of rotational phase for fast wing rotation

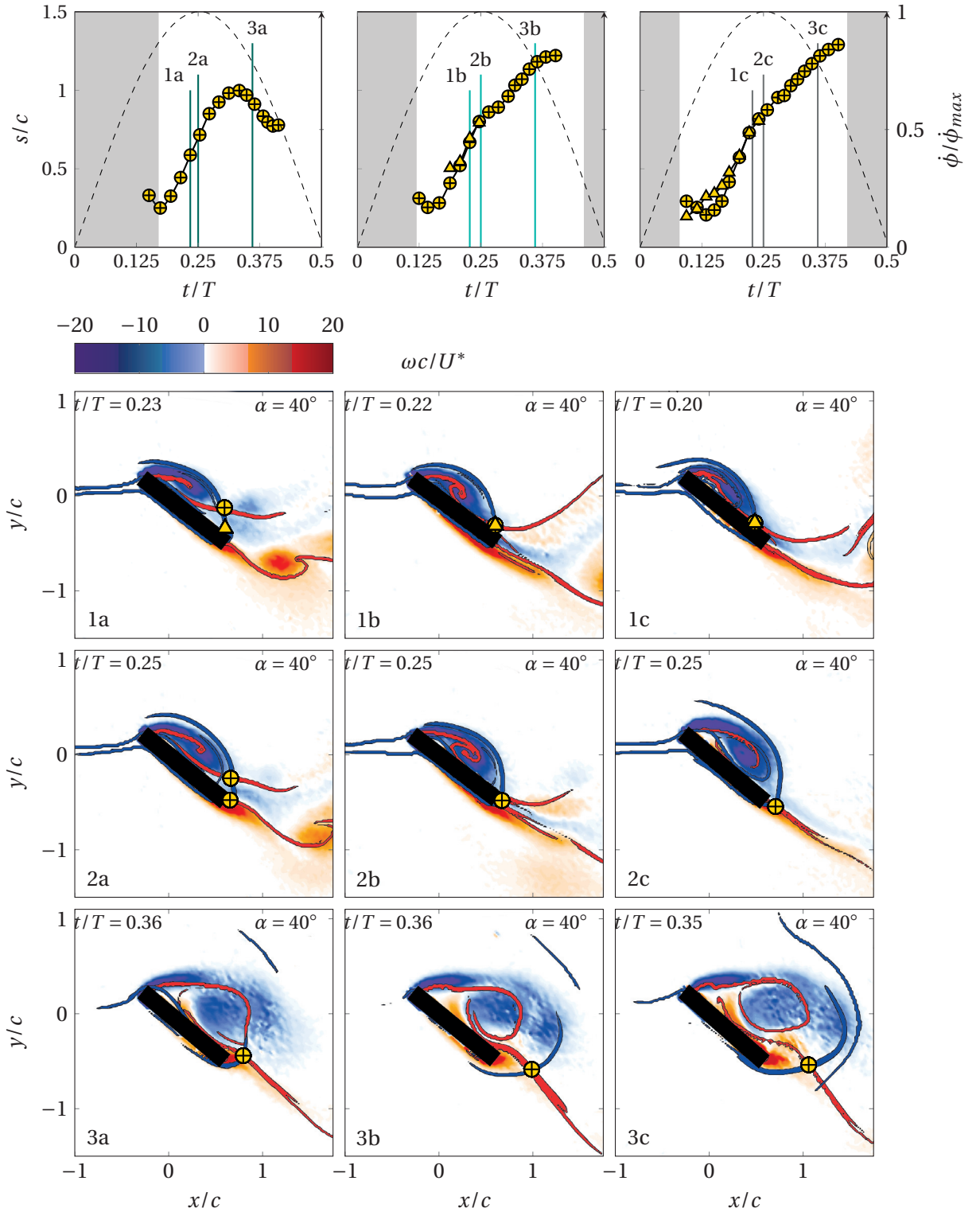


Figure 3.28 – Top row: Saddle distance evolution for (a) fully delayed (b) partly delayed (c) symmetric rotations, including stroke velocity (---). Gray areas indicate rotation. Corresponding flow fields at time instants when, row 1: saddles merge, row 2: saddle, thereby LEV lifts-off, row 3: End of LEV lift-off stage.

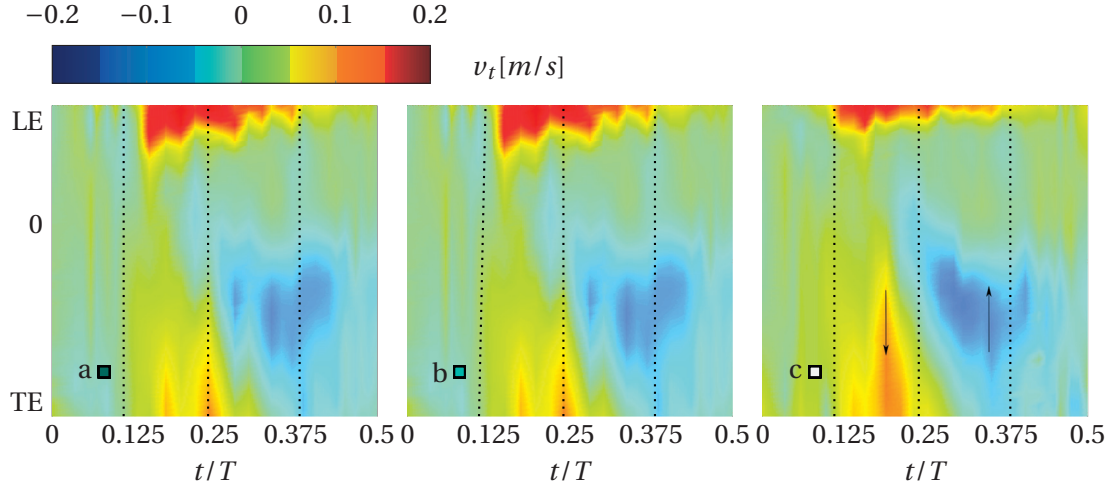


Figure 3.29 – Tangential velocity on the suction side of the wing through half-stroke for (a) fully delayed, (b) partly delayed, and (c) symmetric rotations . Black arrows represent the direction of flow for warm colors (LE to TE) and cold colors (TE to LE).

### LEV breakup and decay

The LEV in all three cases breaks down almost at the same time (figure 3.30). The fully delayed rotation shows the strongest vorticity. Unlike the symmetric rotation, the flow features stay close to the wing in fully delayed rotation figure 3.30 (a ■). Given that the wing does not rotate

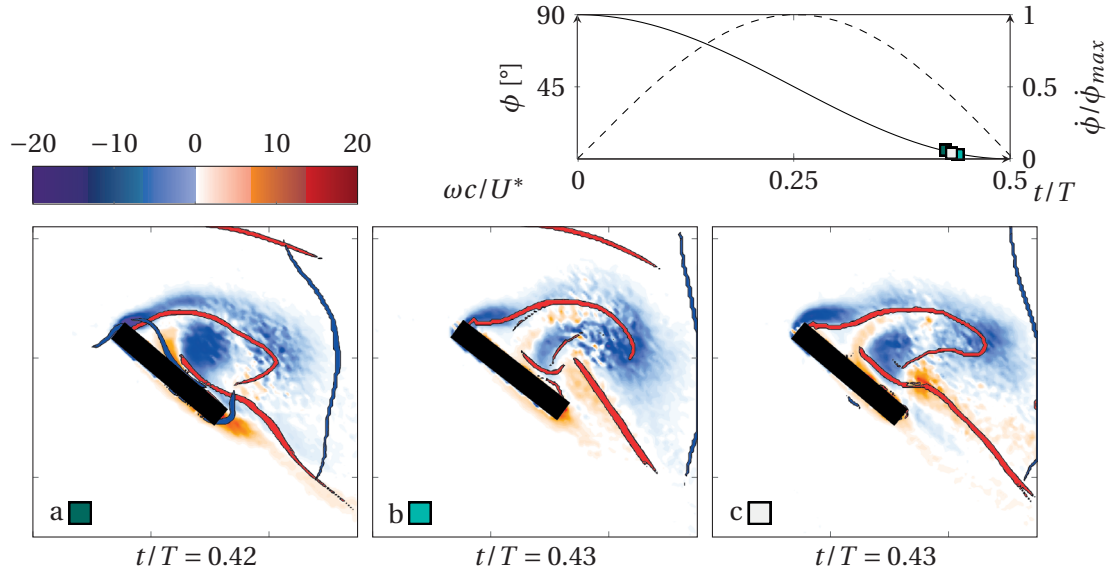


Figure 3.30 – Flow fields showing the end of LEV break-up for (a) fully delayed rotation (b) partly delayed (c) symmetric rotation. Top right: Stroke position (—) and stroke velocity (---) of the half-stroke with the corresponding time instants.

### 3.3. Influence of rotational phase for fast wing rotation

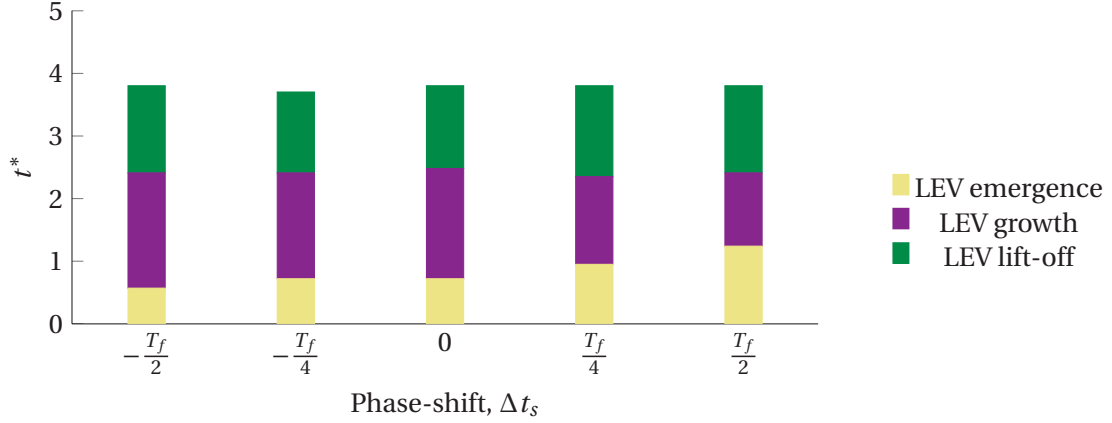


Figure 3.31 – Notable non-dimensional times during the life-cycle of the LEV for the fast wing rotation ( $T_f = T/6$ ).

anymore in the delayed rotations, the structures do not disperse like in the case of symmetric rotation. But the split concentrations remain close to each other. The LEV splits in the partly delayed (b □) rotation breaks down and decays in the flow similar to the symmetric rotation (c □).

The convective time scales at which the crucial stages of flow development occur in the different phases of wing rotation with a fast flip duration is presented in figure 3.31. The LEV emergence stage lasts longer in the delayed rotation cases compared to the advanced and symmetric rotation. This is due to the negative angle of attack during the initial acceleration in stroke, which pulls the LEV along the trajectory of the leading edge. The end of the LEV growth occurs nearly at the same time, at  $\approx 2.5$  convective time scales, indicating that the stroke velocity plays an important role in defining the feeding of vorticity into the flow structure and the saddle lift-off. The subsequent lift-off results in similar behaviour of the LEV for all cases

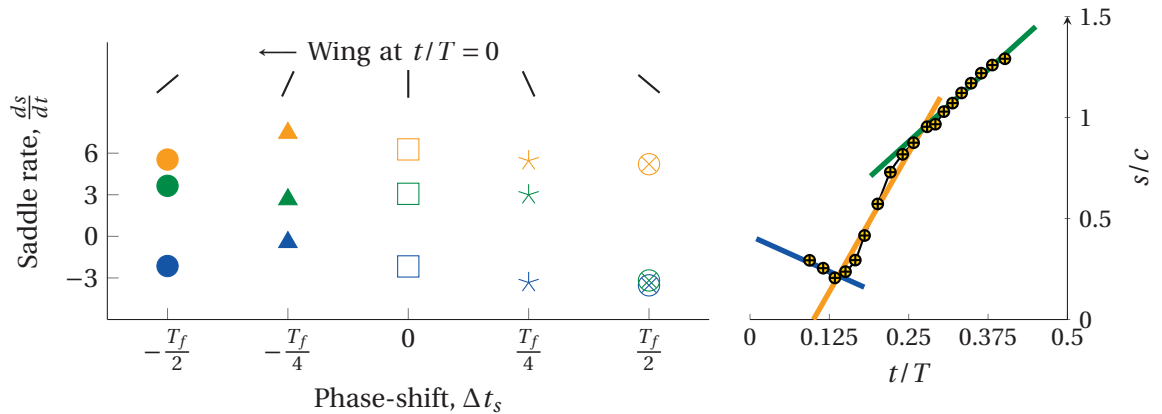


Figure 3.32 – Left: Rates of the full saddle movement for the fast wing rotation ( $T_f = T/6$ ). Right: Example demonstrating the three segments in the saddle curve with varying growth rate.

and reaches a maximum circulation at about 3.8 convective time scales, which corresponds to the end of the third stage beyond which the LEV breaks down.

The saddle distance curve in general shows three gradients in each case, which is differentiated by the three colors (figure 3.32 (right)). The rate at which the saddle moves in the flow fields are tracked for all phase-shifts and a comparison is presented in figure 3.32 (left). The blue symbols indicate the rate at which the full saddles in each case move towards the wing's axis of rotation. The orange symbols indicate the rate at which the saddles move towards the trailing edge. The green symbols indicate the rate at which the saddles move away from the wing after lift-off. The saddle rates decrease in general from most advanced to most delayed rotation. The saddle rates in the growth stage (orange) beyond the axis of rotation ( $t/T > 0.125$ ) are approximately twice that of the LEV lift-off stage (green).

### 3.3.3 Forces during the fast wing rotation

#### Lift

The general lift force distribution for entire flapping cycle for representative phase-shifts with the fast wing rotation is presented in figure 3.33. All the cases exhibit roughly sinusoidal lift distribution over the flapping cycle. The advanced rotation shows higher lift at the half-stroke commencement and the delayed rotation shows the least. This is related to the rotational phase at the start of the stroke. Maximum lift is produced close to the maximum stroke velocity around  $t/T = 0.25$ . The least lift produced is close to stroke reversal ( $t/T = 0.5$ ). For advanced rotation, it occurs before the stroke reversal and delayed rotation, after the stroke reversal. This low lift region corresponds to the period where the wing rotates. This is discussed in detail and compared along with other measurement cases.

The maximum lift and mean lift produced for varying phase-shifts ( $\Delta t_s$ ) is presented in figure 3.34. As expected with a fast flip duration, in which case the duration of rotation is very small, the maximum lift produced is nearly the same for all cases. For most of the half-stroke, the wing translates with a constant angle of attack ( $\alpha = 40^\circ$ ), which implies that there is ample time in the flapping cycle for a sustained build up of the vorticity on the suction side of the wing. The maximum lift occurs close to the mid half-stroke; which corresponds to the maximum stroke velocity (figure 3.35). The maximum stroke velocity,  $(\frac{d\phi}{dt})_{max}$  at  $t/T = 0.25$ , is a constant for all phase-shifts and flip duration and is marked by the vertical dashed line. This corresponds to the saddle lift-off from the trailing edge, signaling the start of the LEV lift-off stage. The maximum lift points are all situated very close to this line on the stroke curve. Except for the most delayed rotation, the maximum lift is attained just before the LEV lift-off. In the fully delayed rotation, the maximum lift is attained just after the LEV lift-off. The most advanced rotation attains the maximum lift earliest among all cases.

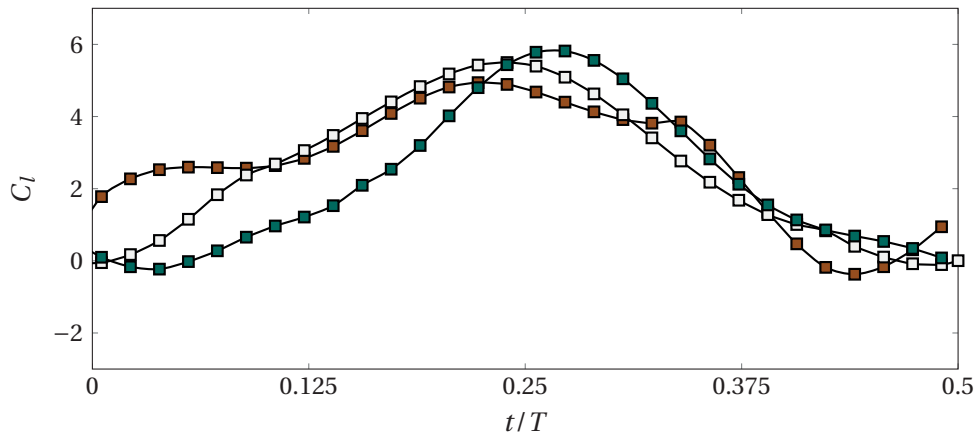


Figure 3.33 – Lift evolution in half-stroke for representative variations of phase-shift  $\Delta t_s$ , for the fast rotation. Fully advanced —■—, symmetric —□—, fully delayed —▲— rotations.

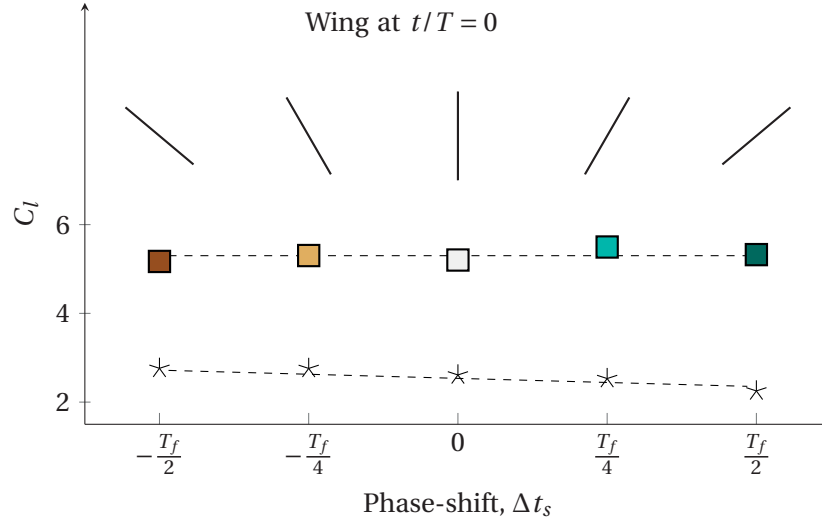


Figure 3.34 – Maximum (squares) and mean (stars) lift for variations in the phase-shifts for the fast rotation. The black bars on the top represent the angle of attack at the beginning of the half-stroke.

The corresponding flow fields at the instant of maximum lift is presented in figure 3.36(a)-(e). In all the cases, the flow fields look remarkably similar with a bound LEV on the suction side of the wing and the merged saddle at the trailing edge. This suggests that the growth stage is the critical part in the LEV life cycle which sees an increasing vorticity flux, thereby an increasing lift. The lift-off of the LEV from the surface alters the pressure distribution on the wing and along with the decreasing vorticity production at the leading edge, contributes to the decrease in lift. The above described trends suggest that for a very short duration of rotation, despite varying the phase, no considerable changes in the maximum lift can be noted. The short rotation doesn't affect the lift generation and lift primarily depends on the stroke velocity.

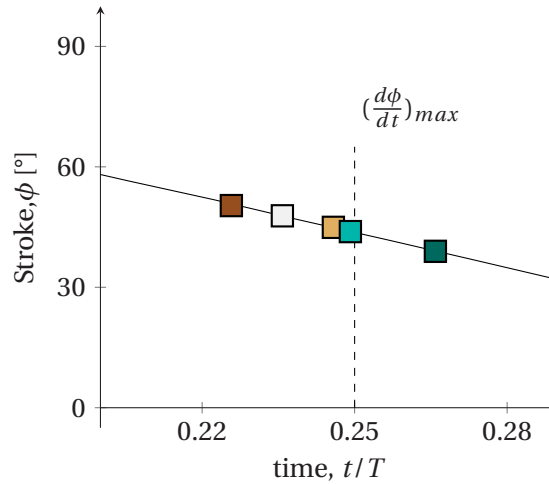


Figure 3.35 – The time at which maximum lift occurs for the fast rotation in a stroke cycle.

### 3.3. Influence of rotational phase for fast wing rotation

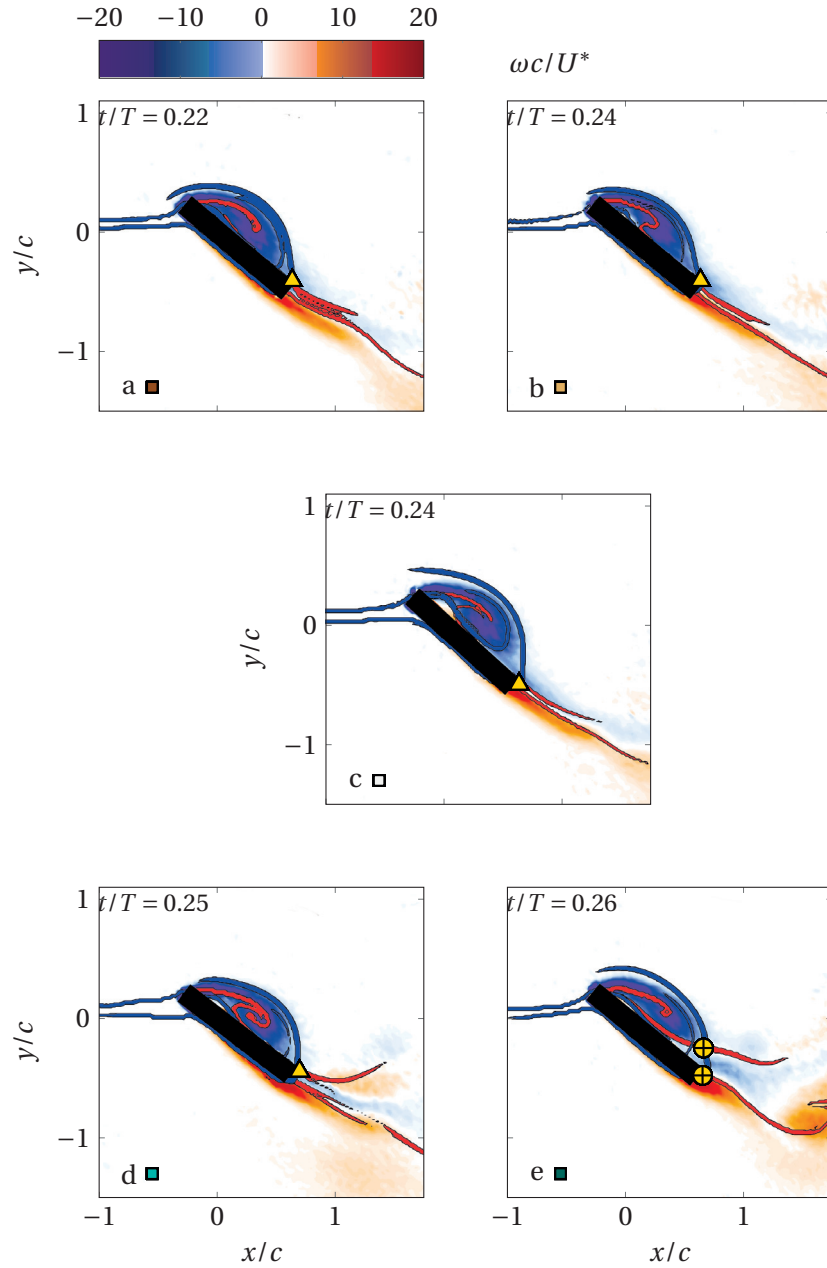


Figure 3.36 – Flow fields at maximum lift for (a) fully advanced (b) partly advanced (c) symmetric (d) partly delayed (e) fully delayed during a fast rotation.

#### Drag

The general drag force distribution for entire flapping cycle for representative phase-shifts with the faster flip duration are presented in figure 3.37. The advanced rotation shows higher, nearly constant drag at the half-stroke commencement whereas the delayed and the symmetric rotation increases from a minimum with large gradients. Maximum drag is produced close to

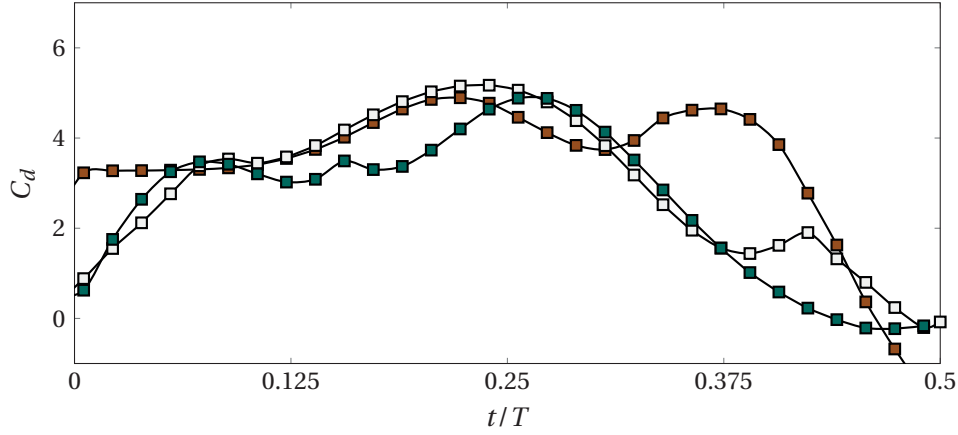


Figure 3.37 – Drag evolution in half-stroke for representative variations of phase-shift  $\Delta t_s$ , for the fast rotation. Fully advanced —■—, symmetric —□—, fully delayed —■— rotations.

the maximum stroke velocity around  $t/T = 0.25$ . The least drag produced is close to stroke reversal ( $t/T = 0.5$ ). This is discussed in detail and compared along with other measurement cases.

A comparison of the maximum drag produced in each case of rotation are presented in 3.38. The maximum drag produced is nearly the same for all phase-shifts. The time instant during the flapping cycle at which it occurs is indicated in figure 3.39. Except for most delayed rotation case, all other variations in phase-shift result in maximum drag values occurring before maximum stroke velocity line represented by  $(\frac{d\phi}{dt})_{max}$  in figure 3.39. The maximum drag occurs at nearly the same instants as the maximum lift and hence the flow fields are

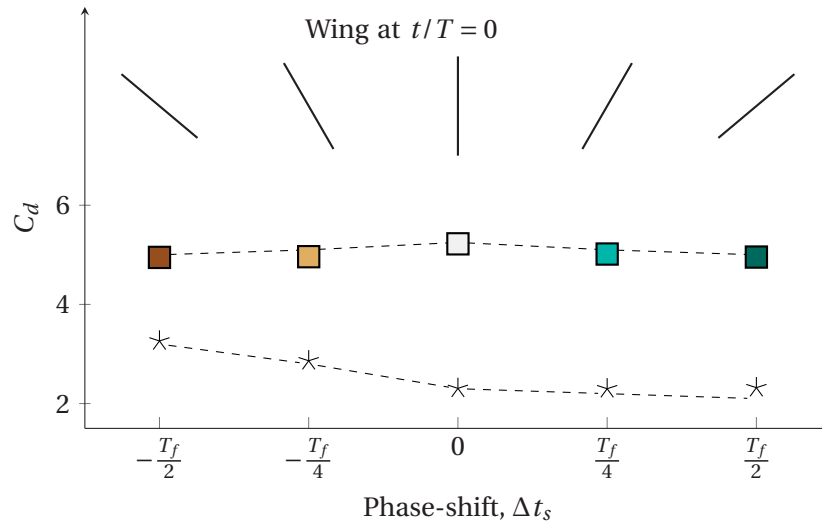


Figure 3.38 – Maximum (squares) and mean (stars) drag variations in the phase-shift for the fast rotation. The black bars on the top represent the angle of attack at the beginning of the half-stroke.



### 3.3. Influence of rotational phase for fast wing rotation

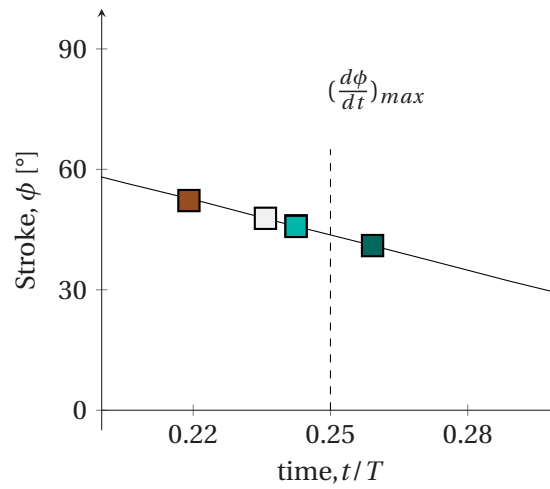


Figure 3.39 – The time at which maximum drag occurs for the fast rotation in a half-stroke.

nearly the same as in figure 3.36. The shorter flip duration here seems to nullify the effect of rotational delay or advancement on the production of drag. Noting the similarities in the flow behaviour for advanced and delayed rotations, these trends in forces are as expected.

### 3.3.4 Summary

The advanced rotation with a fast wing rotation is characterised by a single large LEV just as in the symmetric rotation case. The LEV goes through the same stages of development as seen in the symmetric rotation case (section 3.3). However, the rotation slightly alters the duration and timing of the emergence of the LEV and the subsequent evolution.

A new LEV emerges at the start of the half-stroke and grows in the chord-normal direction characterising the **LEV emergence** stage (figure 3.40(a)). The LEV then moves towards the wing and binds to the wing marking the transition into the second stage (figure 3.40 (b)). The bound LEV grows in the chord-wise direction until the end of the **LEV growth** stage (figure 3.40 (c)). The LEV then lifts-off from the wing allowing a reverse flow from trailing edge to leading edge commencing the **LEV lift-off** stage (figure 3.40 (d)). This enhances the secondary vortex of opposite vorticity between the wing and the LEV (figure 3.40 (e)). The LEV grows further and eventually splits into multiple connected vortical concentrations in the fourth and final stage of the flow cycle (figure 3.40 (f)). The vortical concentrations closest to the wing follow the wing, and the outboard concentrations convect away from the wing in this **LEV breakdown and decay** stage (figure 3.40 (g)-(h)). The advanced wing rotation with a fast flip is characterised by starting vortex at the beginning and at the end of the half-stroke. The wing at the beginning of the half-stroke exhibits a surge-like behaviour leading to higher lift at the start of the half-stroke.

The characteristic flow development for a delayed rotation is presented in figure 3.41. The beginning of the half-stroke is characterised by remnant vorticity concentrations on the wing

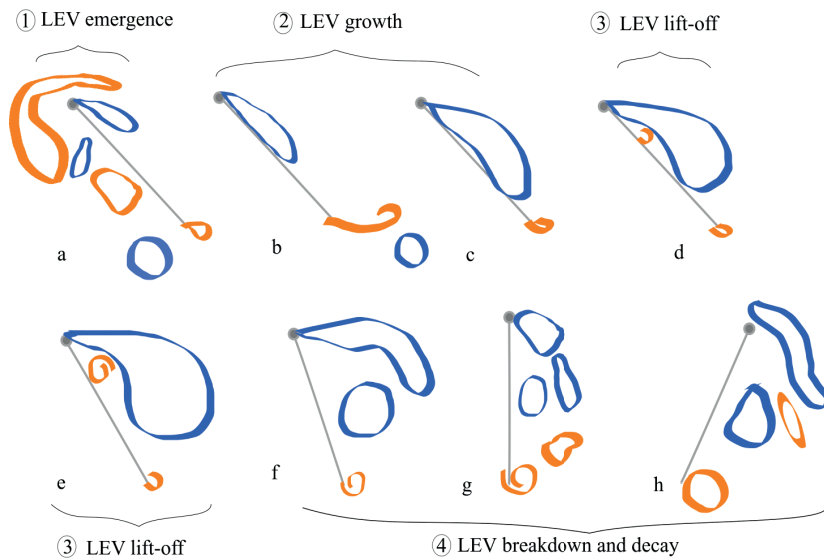


Figure 3.40 – Characteristic flow development in a flapping cycle with advanced, fast wing rotation . The wing moves to the left. The illustration of the features are based on vorticity. Blue features are indicative of the LEV and orange are indicative of the TEV.

### 3.3. Influence of rotational phase for fast wing rotation

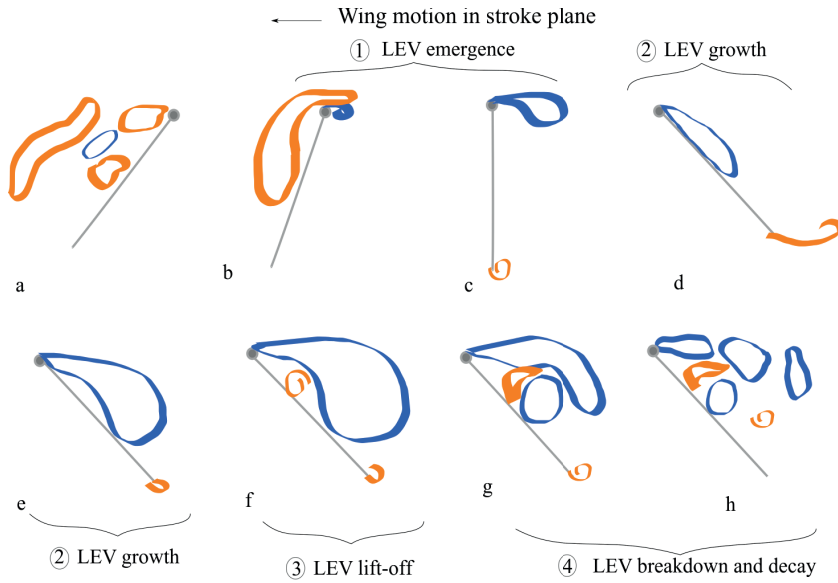


Figure 3.41 – Characteristic flow development in a flapping cycle with delayed, fast wing rotation. The wing moves to the left. The illustration of the features are based on vorticity. Blue features are indicative of the LEV and orange are indicative of the TEV.

from the previous stroke due to the large negative angle of attack (figure 3.41(a)). Vorticity is accumulated over the wing to form an unbound LEV in the first stage : **LEV emergence**. This LEV grows in the chord-normal direction (figure 3.41(b),(c)). The new LEV binds to the wing transitioning into the second stage. This bound LEV now grows in the chordwise direction, until the end of the **LEV growth** stage (figure 3.41(d)-(e)). The LEV then lifts-off at maximum stroke velocity and grows in the chord-normal direction characterising the **LEV lift-off** stage (figure 3.41(f)). The LEV breaks down into multiple concentrations marking the onset of the **LEV breakdown and decay** stage (figure 3.41(g)). These concentrations appear to remain suspended on the wing at the end of the final stage (figure 3.41(h)).

### 3.4 Influence of rotational timing for slow wing rotation

#### 3.4.1 Effect of rotational duration for symmetric rotation

The effect of rotational phase on the vortex dynamics and forces for a hovering wing with a rotational duration of  $T_f = T/6$  in a half-stroke was discussed in section 3.3. It was shown that the lead or lag in the rotational phase did not affect the process of formation, growth and, breakdown of the LEV but altered the duration of the flow stages and forces. The different rotational phases were characterised by a single bound LEV that exhibited a chord-wise and then a chord-normal growth before breaking down into multiple vorticity concentrations. The effect of rotation was minimal in these cases, and the flow and force evolution showed a strong dependence on the stroke velocity. In order to explore this dependence further, the rotational duration was doubled for a symmetric rotation and was analysed similar to the previous chapter. In this section, a symmetric rotation with zero phase-shift ( $\Delta t_s = 0$ ) for wing rotation that spans one-third of the time period in each half-stroke ( $T_f = T/3$ ) has been compared to the base case presented in section 3.2. The effect of this rotational duration on the development of the flow fields and forces in a symmetric rotation is discussed extensively.

The flow development in the crucial stages of the flapping cycle for both fast and slow rotation are presented in figure 3.42. The symmetric rotation in the fast rotation shows a newly emerged LEV that grows in the chord-normal direction during the first stage of the flow cycle (figure 3.42 (a)). Due to the fast rotation, the emerging LEV is entrained by the leading edge which results in an elongated arc shaped LEV. The chord-normal growth in this case ends with the end of the first rotation at  $t/T = 0.08$ . Once the wing assumes a constant geometric angle of attack in the translation phase, the LEV binds to the wing as described in figure 3.6.

A similar first stage is observed in the slow rotation, which is characterised by a chord-normal growth of the unbound LEV (figure 3.42 (d)). The leading edge velocity is lower due to the slow rotation which does not result in an elongated arc shaped LEV as seen in the fast rotation. The first stage in the flow cycle of the slow rotation with symmetric rotation ends at a later time instant of  $t/T = 0.13$ . The slow rotation is also characterised by a starting vortex at the trailing edge. A distinct starting vortex is absent in case of the fast rotation where the duration of rotation is too small for a sustained roll up of the shear layer during the first rotation. In the slow rotation, the wing is still rotating when the **LEV emergence stage** is completed.

The second stage in the flapping cycle: LEV growth is dominated by the binding and chord-wise growth of the LEV on the suction side of the wing. At the end of the LEV growth stage, the fast rotation exhibits a larger LEV, along with a secondary vortex between the wing and the LEV (figure 3.42(b)). A half-saddle ( $\Delta$ ) sits at the trailing edge binding the LEV to the wing. In comparison, a compact LEV identified by the rolled up nFTLE ridge characterises the slow rotation in the second stage (figure 3.42(e)). The nFTLE and pFTLE intersect to reveal a full saddle ( $\oplus$ ), while the pFTLE ridge interacts with the trailing edge to form a half-saddle ( $\Delta$ ). This suggests the presence of two concentrations of the LEV on the suction side of the wing.

### 3.4. Influence of rotational timing for slow wing rotation

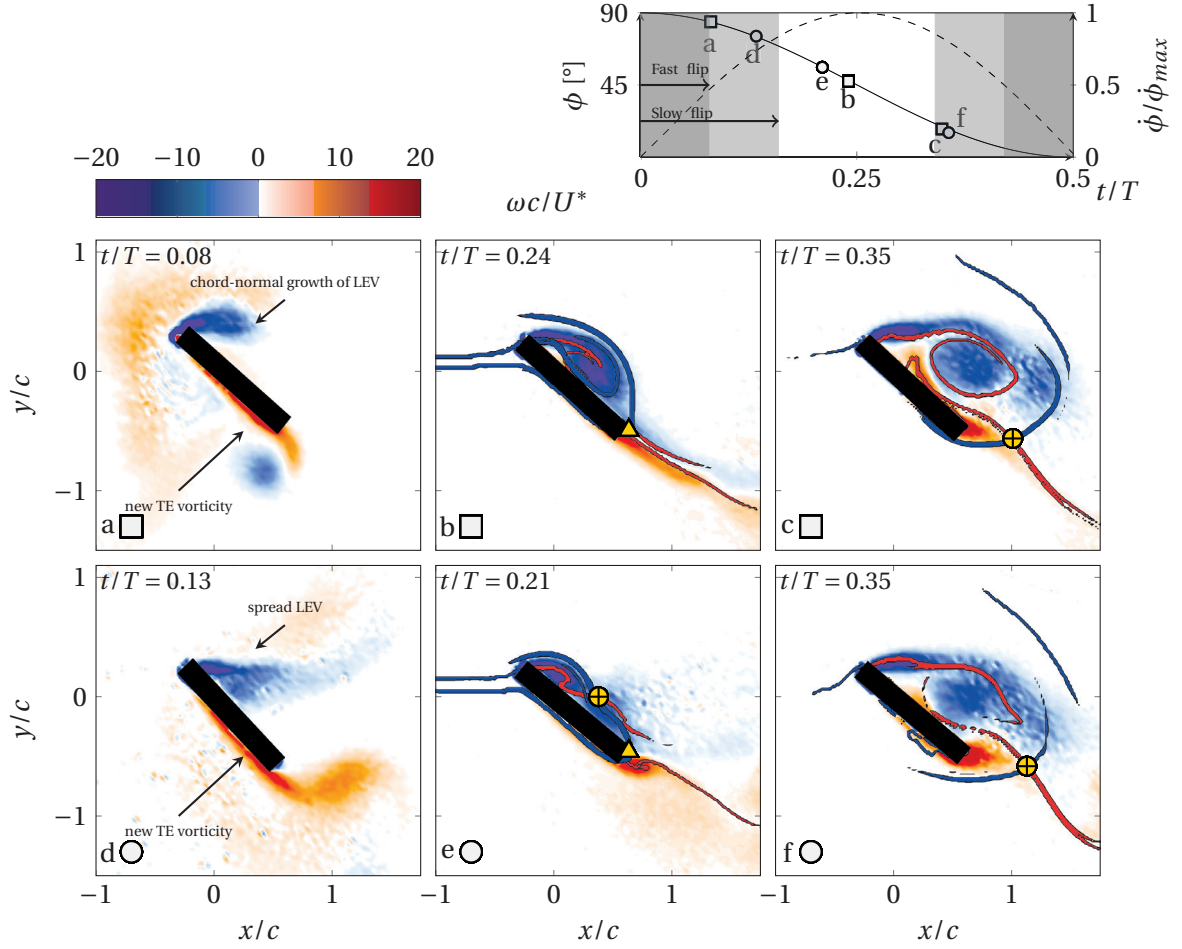


Figure 3.42 – Flow fields at crucial stages in symmetric rotation Top row: Fast flip ( $T_f = T/6$ ). Bottom row: Slow flip ( $T_f = T/3$ ). Column 1: End of LEV emergence, Column 2: End of LEV growth, Column 3: End of LEV lift-off. Top right: Stroke position (—) and stroke velocity (---) of the half-stroke with the corresponding time instants. Gray area indicate period of rotation for fast and slow rotation.

This development of the LEV is characterised by the movement of topological saddles that are identified as the intersection of nFTLE and pFTLE ridges. The appearance of the intersecting FTLE ridges and movement of saddles is slightly different in the slow rotation. In comparison to the fast rotation where the half-saddle merges with the full-saddle at the wing surface and they move together towards the trailing edge, the slow rotation does not exhibit the merging of the full and half-saddle.

The detailed saddle movement for the slow rotation is depicted in figure 3.43. The nFTLE ridge at the end of the LEV emergence stage at  $t/T = 0.13$  is horizontal and begins to pivot towards the wing (figure 3.43 (a)-(b)). The emergence of pFTLE ridge near the axis of rotation of the wing is observed at  $t/T = 0.15$  ( $\Delta$ ). At the same time a pFTLE ridge emerges at the trailing edge (figure 3.43 (b)). The top pFTLE ridge lifts-off the surface of the wing and merges with the

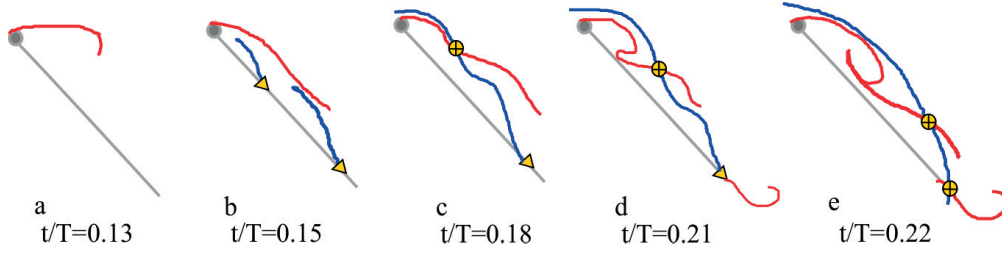


Figure 3.43 – LEV binding phenomenon during pure translation for the slow rotation. The sketch is based on the **nFTLE** and **pFTLE** ridges.

bottom pFTLE ridge to form a single ridge with an inflection point close to the mid-chord at  $t/T = 0.18$ , as seen in figure 3.43 (c). A similar inflection point is observed in the nFTLE ridge as well. The nFTLE ridge folds in close to this inflection point, indicating a compact LEV that spans up to the axis of rotation (figure 3.43 (d)). The half-saddle formed by the single pFTLE and the wing is now at the trailing edge (figure 3.43 (d)). A TEV is formed at the end of the LEV growth stage. The full-saddle (⊕) is near three-fourths of the chord at the end of the **LEV growth** stage.

The end of the growth stage is characterised in both cases with the half-saddle reaching the trailing edge. In case of the fast rotation the growth stage ends at  $t/T = 0.24$ , just before the maximum stroke velocity (figure 3.42(b)). Whereas, in the slow rotation, the growth stage ends sooner than the fast rotation as the half-saddle lifts-off at  $t/T = 0.22$  (figure 3.42(f)). This signifies the onset of the **LEV lift-off** stage. The lift-off of the saddle allows a reverse flow from the trailing edge to the leading edge. The tangential velocity plot shows a reverse flow established in the third stage which lasts the rest of the half-stroke (figure 3.44(a)). In comparison to the fast rotation (figure 3.44(b)), the reverse flow in the slow rotation is stronger, especially in the fourth stage. The slow rotation at the end of the half-stroke is characterised by stronger LEV compared to the fast rotation. This strong clock-wise vorticity promotes the upward velocity at the wing until the end of the half-stroke. The slow rotation also shows reverse flow near the axis of rotation which corresponds to the roll up of the nFTLE ridge in the LEV growth stage (figure 3.43 (c)-(d)). During this third stage of flow cycle, the LEV grows in the chord normal direction, which is substantiated by the chord normal height. The lift-off stage ends at  $t/T \approx 0.36$ , nearly the same as the fast rotation (figure 3.42 (c), (f)). From hereon, the LEV breaks into multiple concentrations and decays until the end of the half-stroke, similar to the fast rotation.

The chord-normal height ( $h/c$ ) in the slow rotation is smaller and nearly even compared to that of the fast rotation (figure 3.45, region (1)). The growth of the unbound LEV is slower (—○—) as seen by the smaller gradient in the chord-normal height in comparison to the fast rotation (—□—). This correlates with the slower velocity at the leading edge in the slow rotation. The chord-normal height ( $h/c$ ) in the second stage is nearly the same for fast and slow rotations (figure 3.45, region (2)). The chord normal height (—○—) decreases at  $t/T = 0.13$  to a minimum in the slow rotation, signifying the onset of the LEV growth stage where the

### 3.4. Influence of rotational timing for slow wing rotation

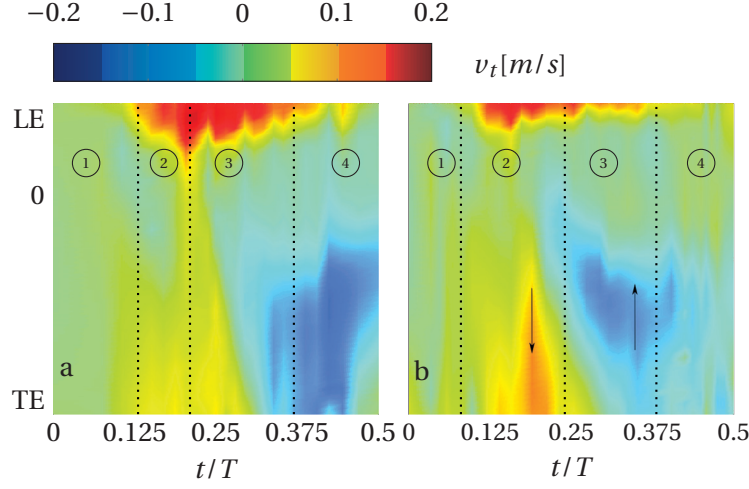


Figure 3.44 – Tangential velocity on the suction side of the wing through half-stroke. Left: Slow rotation ( $T_f = T/3$ ). Right: Fast rotation ( $T_f = T/6$ ). Black arrows represent the direction of flow for warm colors (LE to TE) and cold colors (TE to LE).

LEV moves towards the wing and binds to the suction side. The lift-off stage (region ③) is characterised by a linear increase in the chord-normal height ( $h/c$ ) (figure 3.45 —○—).

The saddle movement in the half-stroke is quantified by tracking the saddle-distance ( $s/c$ ) (figure 3.46). The top half-saddle at the quarter-chord (—▲—) emerges soon after the end of the first stage at  $t/T = 0.15$ . When  $0.18 \leq t/T \leq 0.21$ , the pFTLE ridges merge and form a single half-saddle close to the trailing edge. The full-saddle (figure 3.46 —●—) is formed only

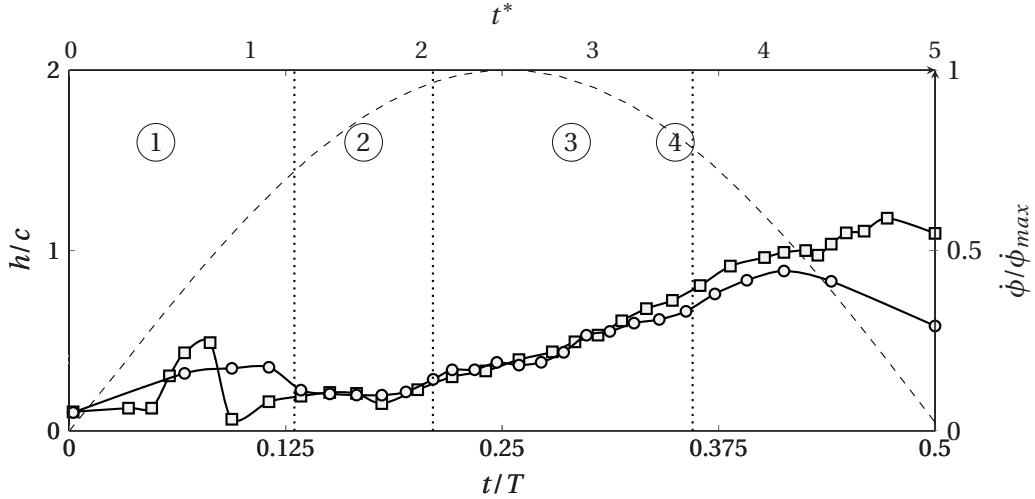


Figure 3.45 – Chord-normal height of the leading edge vortex for symmetric rotation for slow flip (—○—) in comparison with fast flip duration (—□—). Top x-axis shows the convective time scale ( $t^*$ ).

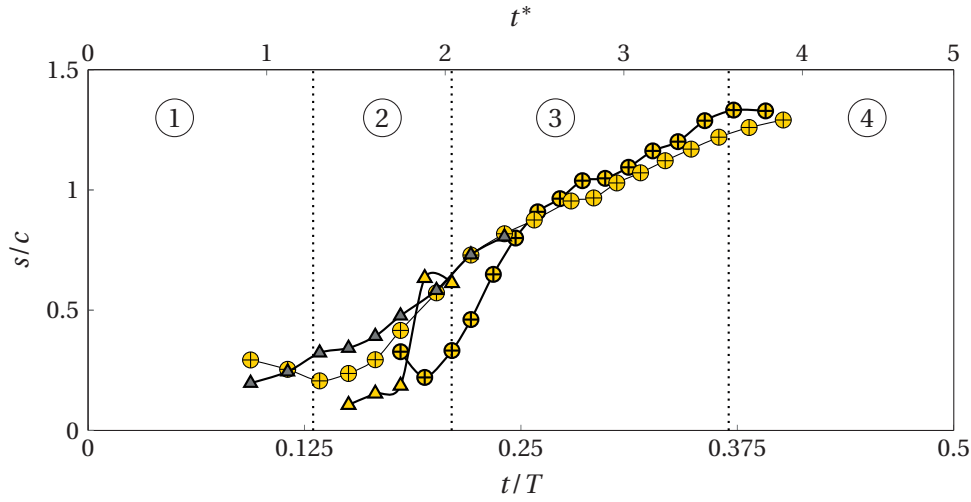


Figure 3.46 – Full saddle distance (—●—) and half-saddle distance(—▲—) for slow rotation. The saddles in gray denote that of the fast flip. Top x-axis shows the convective time scale ( $t^*$ ). The vertical dotted lines separate the LEV (1) emergence, (2) growth, (3) lift-off, and (4) breakdown and decay stages of the slow flip.

at  $t/T = 0.18$ , unlike the fast rotation where the full-saddle emerges at the same time as the half-saddle. In the third stage, the full-saddle moves away at nearly the same rate as in the fast rotation.

The convective time scales at which the crucial stages of flow development occur in the different phases of wing rotation with a slow rotation duration is compared with that of the fast rotation and is presented in figure 3.47. The LEV emergence stage lasts longer in the slow rotation compared to the fast rotation case. The LEV growth stage ends earlier compared

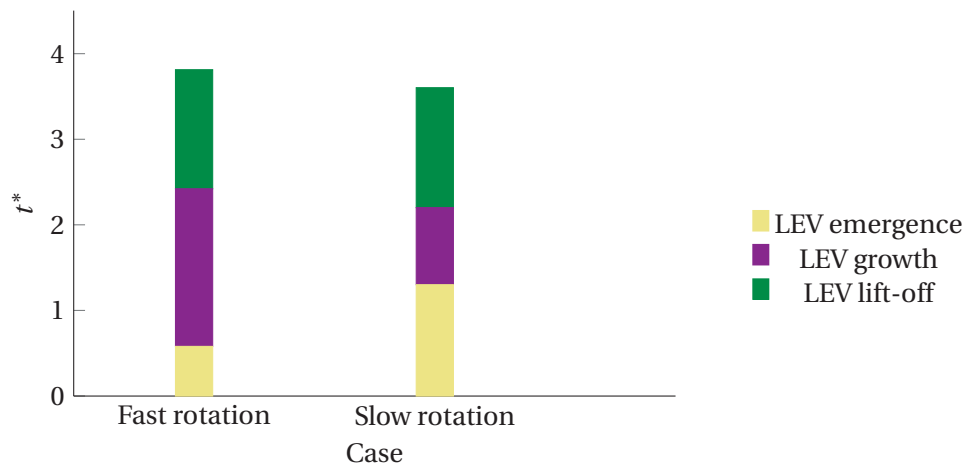


Figure 3.47 – Notable non-dimensional times during the life-cycle of the LEV for the symmetric wing rotation with fast and slow rotations.



### 3.4. Influence of rotational timing for slow wing rotation

to the fast rotation case. The short duration of the LEV growth stage in the slow rotation is expected as the emergence stage lasts longer and the half-saddle lifts off earlier than in the case of slow rotation. The subsequent lift-off results in nearly similar behaviour of the LEV for both cases. The LEV reaches a maximum circulation at 3.6 convective time scales slightly earlier than the fast rotation ( $t^* = 3.8$ ).

#### Effect of rotational duration on forces

The lift and drag evolution for slow (—■—) and fast rotation (—) of symmetric rotation are presented in figure 3.48. The slow rotation displays an inherent dependence on the stroke velocity which drives the vorticity accumulation. Lift increases in the LEV emergence and LEV growth stages while decreasing in the LEV lift-off and breakdown stages. The rate at which lift increases in the LEV growth stage (region ②) is nearly twice that of the LEV emergence stage (region ①). Lift (—■—) reaches a maximum at the maximum stroke velocity  $t/T \approx 0.25$  in the LEV lift-off stage (region ③). This suggests that the LEV growth stage is when most of the lift is produced in the presence of a bound LEV. The lift produced in the slow rotation increases at a rate nearly half that of the fast rotation in the LEV emergence stage (region ①). This is caused by the combination of the slower wing rotation which generates less vorticity around the leading edge in the first stage. The lift gradient increases slightly after the end of rotation and is similar to that of the fast rotation in the LEV growth stage (region ②). Another change in the gradient is seen at the end of the LEV lift-off stage, just before the start of the final wing rotation in the half stroke at  $t/T \approx 0.36$  (region ③). Here, the lift decreases at a faster rate compared to the previous stage due to a decreasing stroke velocity and high angles of attack.

The drag produced in the slow rotation is lower than that of the fast rotation. Maximum drag occurs at the maximum stroke velocity, same as the maximum lift just after LEV lift-off (region ③). The gradients in the drag are not as intuitive in the slow rotation. The start of the half-stroke is characterised by large drag (region ①). This is attributed to the bluff body like behaviour by the wing as it moves in the half-stroke with relatively low stroke velocity. The end of the half-stroke (region ④) is characterised by a decreasing drag even as the angle of attack increases. This correlates with the decreasing stroke velocity, highlighting the strong influence of the stroke velocity during wing rotation.

The difference between the forces of slow and fast rotations is observed in the gradients. In the fast rotation, lift increases at a faster rate in the LEV emergence stage compared to the LEV growth stage, whereas in the slow rotation (—■—), it is the reverse (figure 3.48). However, the maximum lift is higher in the fast rotation due to the higher vorticity generation. The third and fourth stages, show almost the same rate of decrease in the lift. In case of the drag, the slow rotation produces an overall higher drag in the LEV emergence stage compared to the fast rotation (region ①). This shows that the duration of rotation has a strong influence on the drag at low stroke velocity.

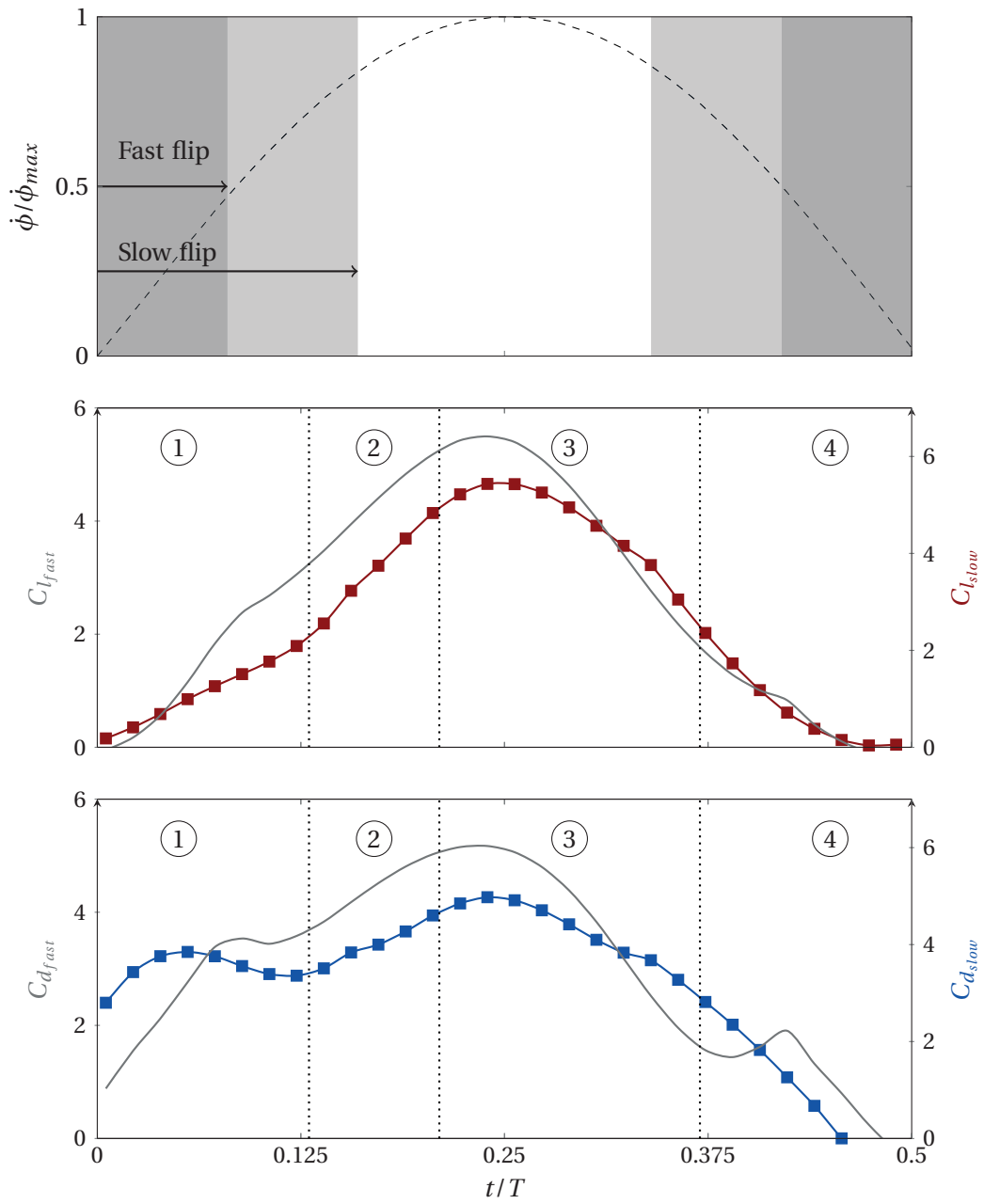


Figure 3.48 – Force coefficients for symmetric rotation. Colored symbols represent the slow rotation Row 1: Kinematics for fast and slow rotation. Gray area indicates the period of rotation. Row 2: Lift coefficients for slow rotation (—■—) compared to lift coefficients from fast rotation (—). Row 3: Drag coefficients for slow rotation (—■—) compared to drag coefficients from fast rotation (—)

### 3.4.2 Advanced rotation

#### Kinematics

In advanced rotation case, the wing rotates most or all the way before the stroke reversal. At the beginning of each half-stroke, the wing is at a positive geometric angle of attack. The wing rotation is advanced by 8%, 10%, and 16% of the total time period. Or in other words, the wing rotation has a lead with respect to the stroke. This is compared with the symmetric rotation case ( $\Delta t_s = 0$ ). A schematic of the starting positions of the wing in the rotational plane are illustrated in figure 3.49. In the fully advanced rotation case ( $\Delta t_s = -\frac{T_f}{2}$ ), the wing has rotated completely at the beginning of the half-stroke and moves in the stroke plane at a geometric angle of attack,  $\alpha = 40^\circ$ . The partly advanced rotation case ( $\Delta t_s = -\frac{T_f}{3.3}$ ) has rotated more than half-way through, up to  $\alpha = 58^\circ$  at the start of the half-stroke. The least advanced rotation case ( $\Delta t_s = -\frac{T_f}{4}$ ) has rotated up to  $\alpha = 65^\circ$  at the start of the half-stroke. Through out this section, symbols assigned to the fully advanced rotation (●), partly advanced rotation (◐), least advanced rotation (◑) and symmetric rotation (○) are used to differentiate the cases. The fully advanced rotation is presented in this section as a representative of the flow evolution in the advanced rotation in a half-stroke. Relevant quantitative comparisons of the other advanced cases are included.

#### Flow development

The flow evolution in the fully advanced rotation case is presented in figure 3.50. The top right panel shows the kinematics and the time instants in the half stroke at which the flowfields are presented. Remnant vorticity pockets of opposite signs are observed in the path of the wing, which undergoes pure translation at an angle of attack of  $\alpha = 40^\circ$  (figure 3.50(a)). A distinct shed TEV from the previous stroke is observed near half-chord. Vorticity is generated at the LE and the pFTLE ridge (blue) delineates the new and old vorticity. This heralds the first stage of the flow cycle : **LEV emergence and growth**. Unlike the previous cases, identifying emergence and chord-wise growth stages separately is tricky in the fully advanced rotation

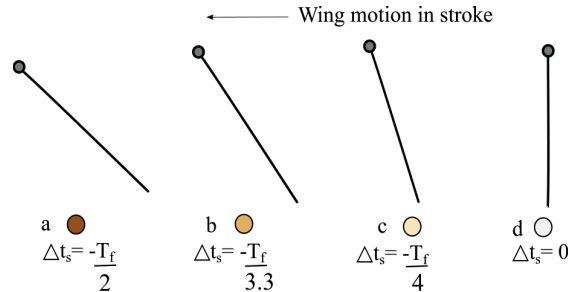


Figure 3.49 – The rotational angle of the wing at the beginning of each half stroke in (a) fully advanced (b) partly advanced (c) least advanced (d) symmetric rotations. The wing moves to the left.

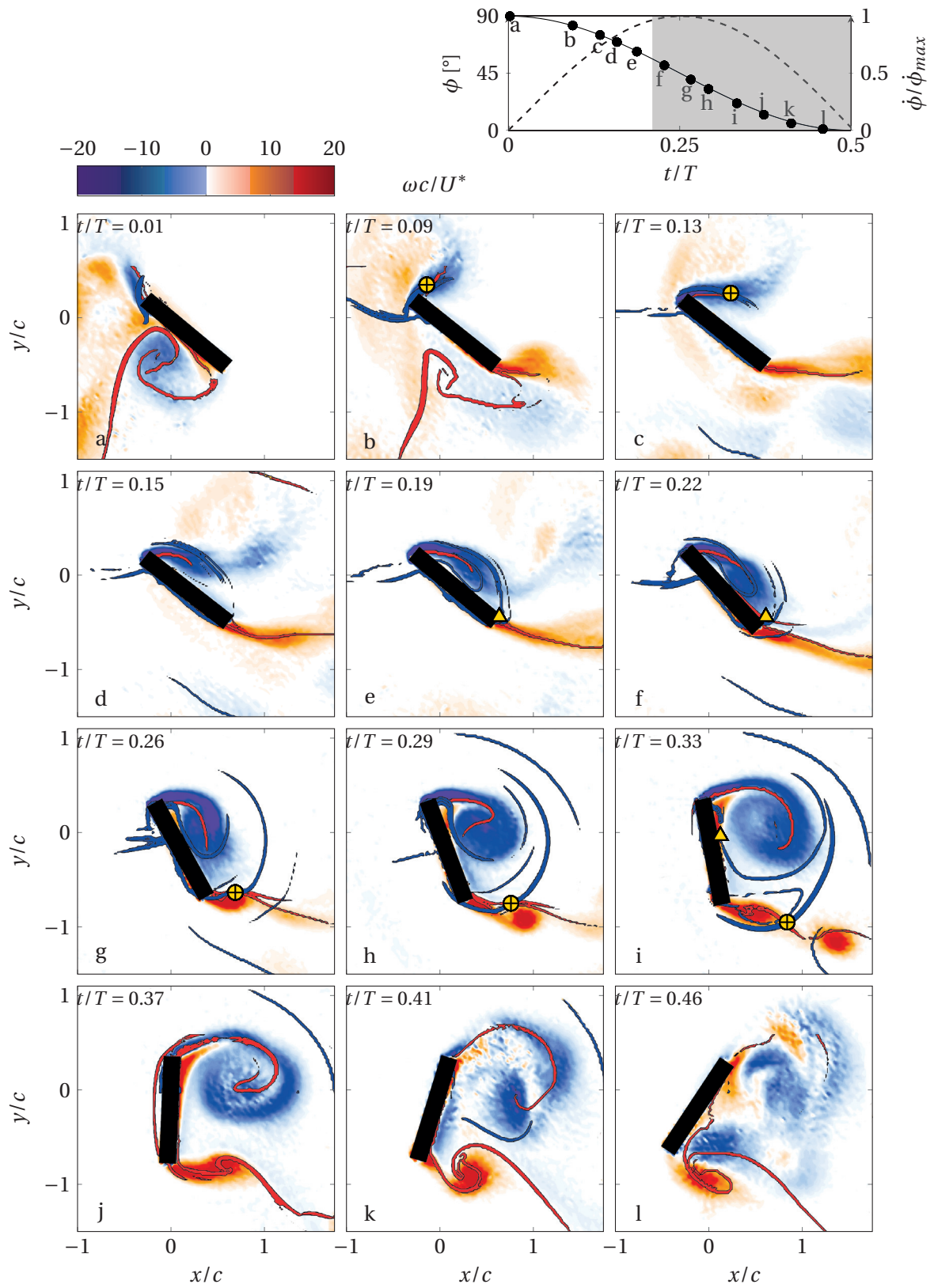


Figure 3.50 – Flow evolution in fully advanced, slow rotation. Top right: Corresponding time instants at which flow fields are shown.

of the slow flip. Due to a favourable  $\alpha$  as the stroke velocity increases, the newly formed LEV continuously accumulates vorticity and simultaneously moves towards the wing. The vertical band of vorticity at the leading edge pivots around the leading edge in a clockwise direction as observed by the nFTLE ridge (figure 3.50(b)). The wing continues to move through the remnant vorticity at  $t/T = 0.09$ . This is substantiated by the pivoting pFTLE ridge at the leading edge which shows that the flow diverges in that region. The pivoting FTLE ridges interact to form a full-saddle ( $\oplus$ ). The LEV grows in size even as it moves towards the wing, observed by the movement of the full-saddle in an arc (figure 3.50(b)-(c)). This full-saddle is not traceable after  $t/T = 0.15$  for the subscribed ridge threshold (figure 3.50(d)). The nFTLE ridge moves closer to the wing while the pFTLE ridge seemingly grows towards the trailing edge. The interaction of the pFTLE ridge with the wing becomes apparent at  $t/T = 0.19$ , revealing the presence of a half-saddle ( $\triangle$ ) (figure 3.50(e)). The presence of the half-saddle indicates a bound LEV. Soon after the wing begins to rotate at  $t/T = 0.21$  which lasts the rest of the half-stroke. The rotation does not influence the half-saddle at the trailing edge until the maximum stroke velocity is reached. The LEV continues to grow along the chord even as  $\alpha$  increases (figure 3.50(f)). This could be due to the increasing stroke velocity.

The pFTLE ridge and thereby the half-saddle then lifts off of the wing at maximum stroke velocity ( $t/T = 0.25$ ), marking the transition into the **LEV lift-off** stage of the flow cycle. The LEV spread over the chord begins to change its direction of growth. Aided by the very large  $\alpha$  at high stroke velocities, the LEV spreads in the chord-normal direction giving an arc like outer shape to the LEV (figure 3.50(g)). The pFTLE ridge interacts with the nFTLE ridge at the trailing edge to form a full saddle. Meanwhile, the LEV detaches from the wing. This enhances the reverse flow in the region which forms a visible secondary vortex between the wing and the LEV (figure 3.50(h)). The LEV continues to grow in size in the chord-normal direction. The arc shape of the LEV is very easily recognisable from the nFTLE ridge (figure 3.50(i)). The LEV appears to be connected to the LE through a band of vorticity. The secondary vortex is pulled into the main LEV that now has a large area. The LEV spreads until  $t/T = 0.35$  when  $\alpha$  becomes negative, which reduces the vorticity being fed to the LEV, thus ending the LEV lift-off stage.

The decreasing stroke velocity combined with a negative angle of attack causes the LEV to spread radially (figure 3.50(j)). Subsequently, the LEV cannot sustain the shape and size despite the relatively high stroke velocity. The LEV and the secondary vortex lose momentum and break down at  $t/T = 0.41$  (figure 3.50(k)). This characterises the **LEV breakdown and decay** stage of the flow cycle. The negative  $\alpha$  allows the wing to move into the LEV that appears to be squeezed. This can be observed by the arc that appears to be squeezed towards the top of the frame. As the wing's angle of attack continues to extreme angles, the LEV and the secondary vortex break into multiple pockets of vorticity (figure 3.50(l)).

At the trailing edge, distinct flow features are observed through out the advanced rotation unlike other cases. The first stage is characterised by a starting vortex at the TE, which convects away (figure 3.50(b)-(c)). The starting vortex is then replaced by a thin shear layer at the TE

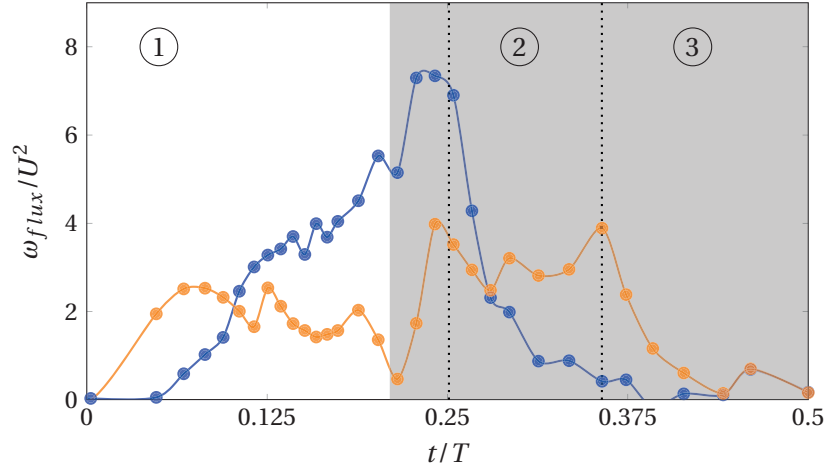


Figure 3.51 – Vorticity flux near the leading edge (—●—) and trailing edge (—○—).

until the end of the translation (figure 3.50(d)-(e)). Upon the start of the rotation, the shear layer rolls up into recognisable circular vortex. This rotational vortex is shed upon the lift-off of the half-saddle from the wing, characterising the end of the first stage (figure 3.50(f)-(g)).

The second stage is characterised by continuous formation and shedding of rotational vortices at the trailing edge (figure 3.50(g)-(i)). The full saddle (⊕) near the trailing edge moves away from the wing and clearly highlighting the movement of the flow in this region. The rotational vortex from the first stage is shed from the trailing edge and a second rotational vortex takes its place soon after. The nFTLE ridges clearly show an interconnected trailing edge vortex system during the wing rotation (figure 3.50(h)-(i)). As the wing tips over to extreme angles of attack, the trailing edge moves in the same direction as the stroke and the rotational vortex formed at the end of the second stage is elongated horizontally (figure 3.50(j)). As the trailing edge moves further upwards, the rotational vortex sheds from the wing (figure 3.50(k)). This shed structure then lingers behind the wing and mixes with the decaying LEV concentrations (figure 3.50(l)).

The flow dynamics are well corroborated by the vorticity flux trends (figure 3.51). The vorticity flux at the leading edge increases sharply in the first stage indicating that the LEV is continuously fed with vorticity figure 3.51—●—). This can be attributed to the constant  $\alpha$  at the start of the stroke when the stroke velocity increases (region ①). Even as the wing rotates at the start of the second stage, the vorticity flux at the LE continues to increase nearly until the maximum stroke velocity. The flux decreases after this instant, proving the primary dependence of the vorticity production on the stroke velocity. Additionally, the steep decrease in LE flux can be attributed to the negative  $\alpha$  in the second stage (region ②). The breakdown stage is characterised by near zero flux at the LE (region ③).

At the trailing edge, the notable part of the flux curve is in the second stage (figure 3.51—○—). The start of the second stage sees a sharp rise in the TE flux due to the wing rotation corresponding to figure 3.50(f). At the end of the second stage, TE flux rises, which corresponds to

### 3.4. Influence of rotational timing for slow wing rotation

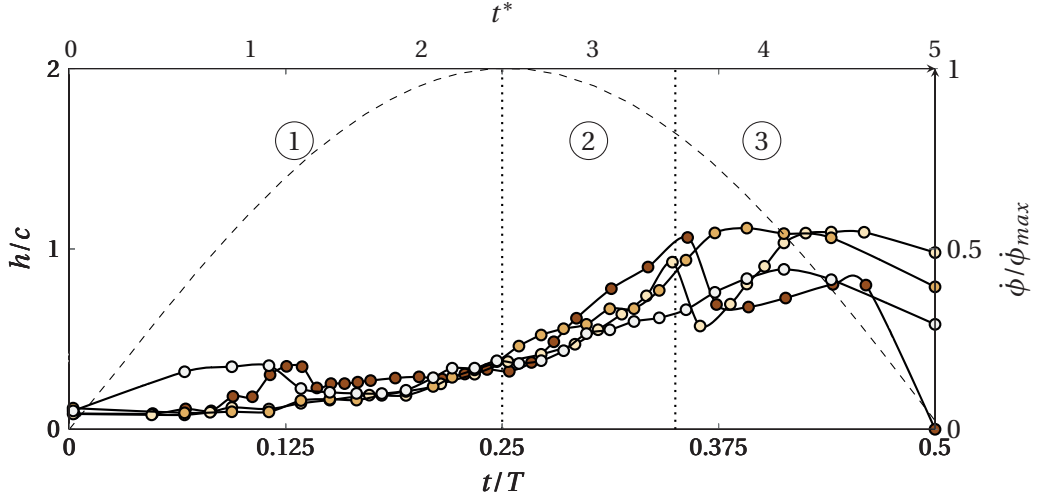


Figure 3.52 – Chord-normal height of the LEV for fully advanced (—●—), partly advanced (—◐—), least advanced (—○—) and symmetric rotations (—○—). The dotted lines mark the end of flow development stages in the advanced rotations. Top x-axis shows the convective time scale ( $t^*$ ).

the TE moving in the direction of the stroke.

The chord normal height for the fully advanced and other advanced rotations are presented in figure 3.52. In general, the advanced rotations show similar stages of development. In the first stage, the LEV starts off with a low chord normal height, signifying that the flow cycle does not begin with a chord-normal growth in this stage for advanced rotations as seen in the symmetric rotation (figure 3.52 region ①). The chord-normal height slowly increases as the LEV pivots and binds to the wing. In the second stage, the LEV sees a rapid growth in

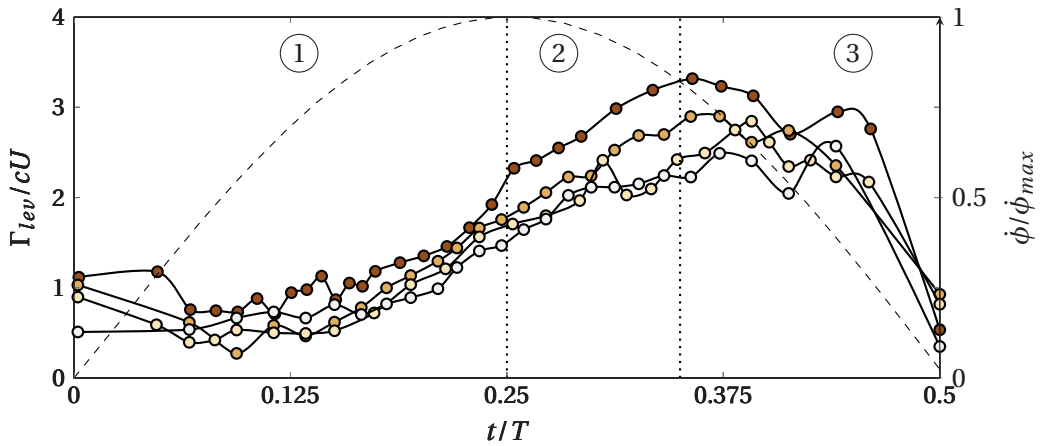


Figure 3.53 – LEV circulation for fully advanced —●—, partly advanced —◐—, least advanced —○—, symmetric —○— rotations. The dotted lines mark the end of flow development stages in the advanced rotations. Top x-axis shows the convective time scale ( $t^*$ ).



the chord-normal direction in comparison to the first stage, as observed by the approximate doubling in the gradient of  $(h/c)$  (figure 3.52 region (2)). As the LEV breaks down, the chord normal height decreases only slightly (figure 3.52 region (3)). At the end of the cycle, the multiple structures have spread up to about 0.5 chord lengths.

A comparison of the LEV circulation for all advanced and symmetric rotations are presented in figure 3.53. The general trends look similar for all the cases. Through the half-stroke, the fully advanced rotation shows the highest circulation (figure 3.53 —●—). This is expected given the large size of LEV generated as well as the surge in the vorticity flux for nearly half the stroke. The symmetric rotation shows the least maximum circulation (figure 3.53 —○—). The maximum circulation is reached almost at the same time at the end of the second stage and the small differences observed here will be discussed more in detail in section 3.4.5. Just like the chord-normal height, the LEV circulation also sees a slow rise in the first stage, a rapid increase in the second stage and a gentle decrease in the third stage until the very end of the half-stroke when the circulation becomes a minimum (figure 3.53, region (1), (2), (3)). The related forces are discussed in section 3.4.6.



### 3.4.3 Delayed rotation

#### Kinematics

In delayed rotation cases, the wing rotates most or all the way after the stroke reversal. The wing starts in each half-stroke at a negative geometric angle of attack. The wing rotation is delayed by 8% , 10%, and 16% of the total time period of the flapping cycle. Or in other words, the wing rotation has a lag with respect to the stroke. This is compared with the symmetric rotation case ( $\Delta t_s = 0$ ). A schematic of the starting positions of the wing in the rotational plane are illustrated in figure 3.54. In the fully delayed rotation case ( $\Delta t_s = +\frac{T_f}{2}$ ), the wing rotates a full amplitude of  $100^\circ$ , starting from a negative angle attack of  $\alpha = 140^\circ$ . The partly delayed rotation case ( $\Delta t_s = +\frac{T_f}{3.3}$ ) has rotated less than half-way through, up to  $\alpha = 122^\circ$  at the start of the half-stroke. The least delayed rotation case ( $\Delta t_s = +\frac{T_f}{4}$ ) has rotated half way through, up to  $\alpha = 115^\circ$  at the start of the half-stroke. Through out this section, symbols assigned to the fully delayed rotation (●), partly delayed rotation (◐), least delayed rotation (◑) and symmetric rotation (○) are used to differentiate the cases. The fully delayed rotation is presented in this section as a representative of the flow evolution in the delayed rotation in a half-stroke. Relevant quantitative comparisons of the other delayed cases are included.

#### Flow development

The flow evolution in the fully delayed rotation case is presented in figure 3.55. The top right panel shows the kinematics and the time instants in the half stroke at which the flowfields are presented. There is a distinct lag in the emergence of the LEV in the fully delayed rotation. The wing has to get rid of the remnant LEV that sits on the wing and attain a positive angle of attack before an LEV emerges.

A large LEV with counter clockwise vorticity from the previous stroke sits on the wing at the beginning of the half-stroke (figure 3.55(a)). The wing simultaneously rotates and translates in the stroke plane through the remnant LEV, starting from a large negative angle of attack ( $\alpha = 140^\circ$ ). The combination of the wing rotation and increasing stroke velocity forces the LEV from the previous stroke to breakdown, decay and spread over the pressure side of the wing.

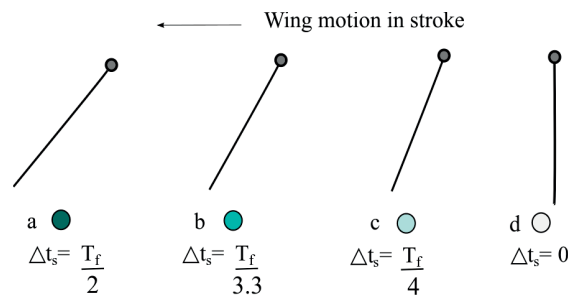


Figure 3.54 – The rotational position of the wing at the beginning of each half stroke in (a) fully delayed (b) partly delayed (c) least delayed (d) symmetric rotations. The wing moves to the left.

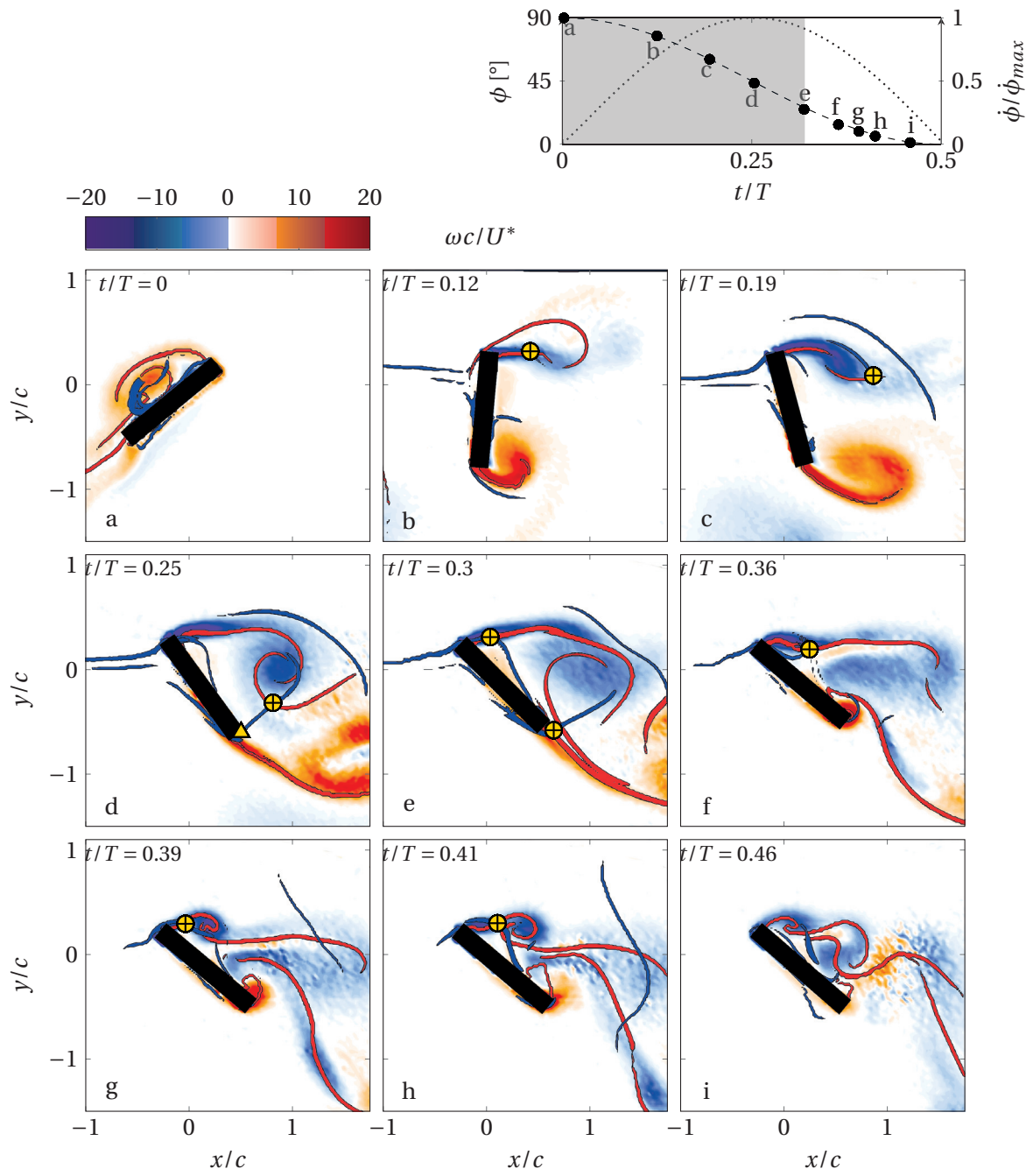


Figure 3.55 – Flow evolution in fully delayed, slow rotation. Top right: Corresponding time instants at which flow fields are shown.

### 3.4. Influence of rotational timing for slow wing rotation

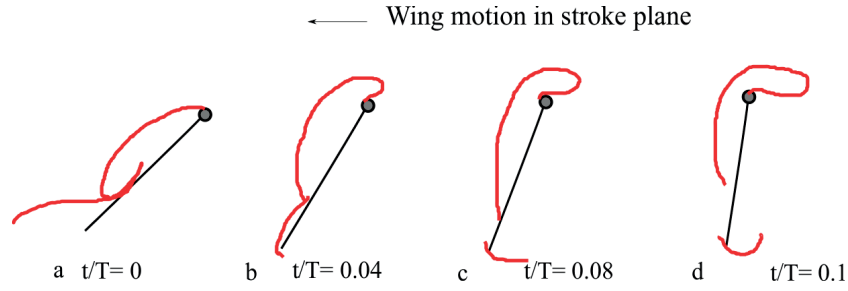


Figure 3.56 – LEV emergence in the delayed rotation of slow flip. Sketch based on nFTLE ridge. The features are indicative of the remnant LEV through which the wing moves.

This phenomenon is presented in detail with the help of the nFTLE ridges in figure 3.56. The nFTLE ridges on the pressure side of the wing moves closer to the wing as the leading edge moves into the remnant LEV from rest (figure 3.56(a)-(b)). The remnant LEV envelops the wing, especially near the leading edge as the wing moves through it. This can be observed by the nFTLE ridge that arcs above the leading edge (figure 3.56 (c)). The arc of the nFTLE ridge over the LE increases in length by  $t/T = 0.1$  when the wing is very close to attaining a positive  $\alpha$  (figure 3.56(d)). The nFTLE ridge evolution here clearly indicates that as the wing moves through the remnant LEV, it carries a part of the old vorticity in the stroke plane up to  $t/T = 0.1$ . The clockwise vorticity accumulating at the leading edge due to increasing stroke velocity and rotation becomes more distinguishable at this instant. The wing attains a positive angle of attack soon after this instant, by which time the remnant LEV on the pressure side is no longer present and the new LEV that emerges over the suction side of the wing grows in the chord-normal direction ( figure 3.55(b)). This marks the end of the **LEV emergence** stage.

The newly emerged LEV grows in the chord-normal direction without binding to the wing as in symmetric and delayed rotations. This chord-normal growth is more apparent once the wing attains a positive angle of attack (figure 3.55(c)). The chord normal growth is unique in delayed rotations in the sense that a band of LE vorticity concentration elongates horizontally while continuing to roll up at a chord-length away from the axis of rotation. A distinct circular feature is discerned by the nFTLE ridge around the LEV (figure 3.55(d)). A secondary vortex forms between the wing and the LEV. This reverse flow in this region is influenced by the clockwise vorticity of the LEV (figure 3.55(c)-(e)). The LEV begins to lose its well defined circular shape as the wing rotation ends (figure 3.55(e)). This marks the end of the **LEV growth** stage of the flow cycle in the delayed rotation.

The onset of the second stage of the flow cycle is marked by the lift-off of the half-saddle just after maximum stroke velocity(figure 3.55(e)). This phenomenon is shown in figure 3.57. A pFTLE ridge delineating the LEV from the outer fluid emerges when  $\alpha > 0$  at  $t/T = 0.19$  and moves towards the trailing edge without interacting with the nFTLE ridge (figure 3.57(a)). The pFTLE ridge interacts with the trailing edge to form a half-saddle ( $\blacktriangle$ ) at  $t/T = 0.25$  (figure 3.57(b)). Soon after the maximum stroke velocity has passed, the half-saddle lifts off the wing at  $t/T = 0.26$  (figure 3.57(c)). The pFTLE ridge interacts with the nFTLE ridge to form a

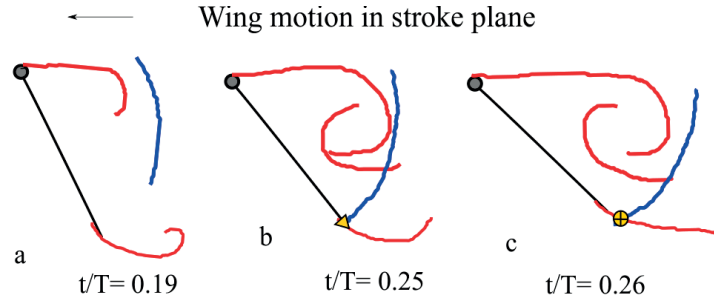


Figure 3.57 – LEV growth in the fully delayed, slow rotation. Sketch based on **nFTLE** and **pFTLE** ridges. The features are mainly indicative of the LEV.

full saddle ( $\oplus$ ). At the end of the second stage, this full saddle is found to linger close to the trailing edge (figure 3.55(e)).

The rest of the half-stroke is characterised by the formation and shedding of multiple LEV at the leading edge, which constitutes to the third and the final stage of the flow cycle : **LEV breakdown and re-emergence**. Soon after the wing begins its pure translation, a strong new LEV is formed at the wing which is observed by the pFTLE ridge intersecting with the nFTLE ridge and forming a full-saddle ( $\oplus$ ) (figure 3.55(f)). This LEV is immediately shed from the wing (figure 3.55(g)). The shedding process of the LEV can be observed by the roll up of the nFTLE ridge and the pFTLE ridge that cuts through the nFTLE ridge forming a full-saddle ( $\oplus$ ) (figure 3.55(g),(h)). Subsequently, a new LEV is formed. The primary LEV from the first two stages of the flow cycle decays and spreads behind the wing (figure 3.55(f)-(i)). The multiple LEV observed during pure translation of the delayed rotation could be attributed to the decreasing stroke velocity and the constant angle of attack. At the end of the half-stroke, due to extremely low stroke velocities the vorticity generation declines and the existing multiple concentrations in the wake follow the wing due to inertia and accumulate as a single concentration, mirroring the flow field at  $t/T = 0$  (figure 3.55(a)).

A starting vortex forms at the trailing edge, aided by the vorticity of the same sign on the pressure side that envelopes the trailing edge and an increasing stroke velocity during rotation (figure 3.55(b)-(d)). The starting vortex grows stronger by the end of the LEV emergence stage and convects away by the end of the second stage. It is replaced by a thin layer of vorticity at the trailing edge as  $\alpha$  becomes smaller (figure 3.55(e)). At the end of wing rotation a translational starting vortex is formed (figure 3.55(f)-(i)), which decays over the rest of the half-stroke due to lowering stroke velocity.

A comparison of the LEV circulation for all delayed and symmetric rotations are presented in figure 3.58. Generally through the half-stroke, symmetric rotation shows lesser circulation compared to the delayed rotations, especially close to maximum stroke velocity (figure 3.58—○—). The most notable difference is the circulation in the last stage of the flow cycle. The symmetric rotation shows higher circulation (figure 3.58 —○—). This is expected as the multiple LEV in the delayed rotations are smaller than that of symmetric rotation. Though the vorticity

### 3.4. Influence of rotational timing for slow wing rotation

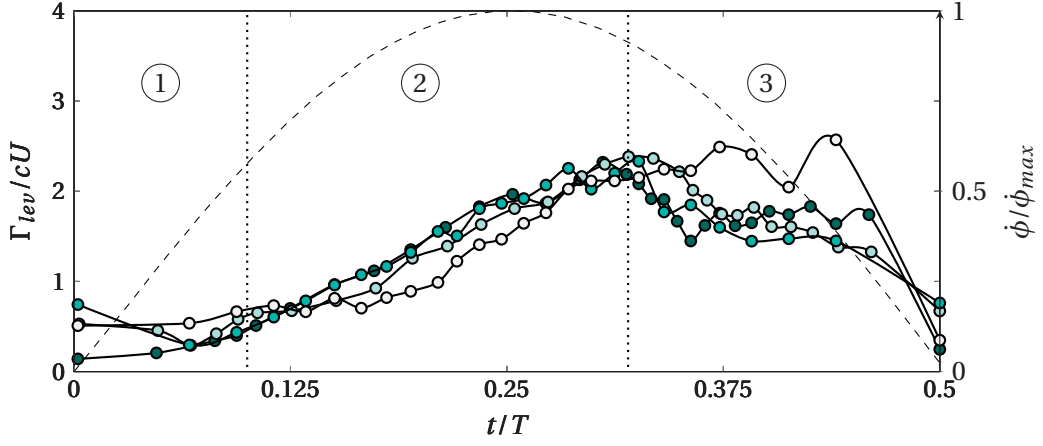


Figure 3.58 – LEV circulation for fully delayed  $\text{---}\bullet\text{---}$ , partly delayed  $\text{---}\bullet\text{---}$ , least delayed  $\text{---}\circ\text{---}$ , symmetric  $\text{---}\circ\text{---}$  rotations. The dotted lines mark the end of flow development stages in the delayed rotations. Top x-axis shows the convective time scale ( $t^*$ ).

generated is nearly the same in symmetric and delayed cases, the size of the LEVs are smaller. The maximum circulation is reached almost at the same time at the end of the second stage and the small differences observed here will be discussed more in detail in section 3.4.5. The LEV circulation also sees an slow increase in the first stage and a rapid increase in the second stage and a gentle decrease in the third stage until the very end of the half-stroke when the circulation becomes a minimum (figure 3.58, region ①, ②, ③). The related forces are discussed in section 3.4.6.

One of the kinematic characteristics at the end of the half-stroke in the advanced and symmetric cases was wing rotation. Due to a decreasing stroke velocity combined with wing rotation, the flow features in these cases experienced breakdown and decay to different

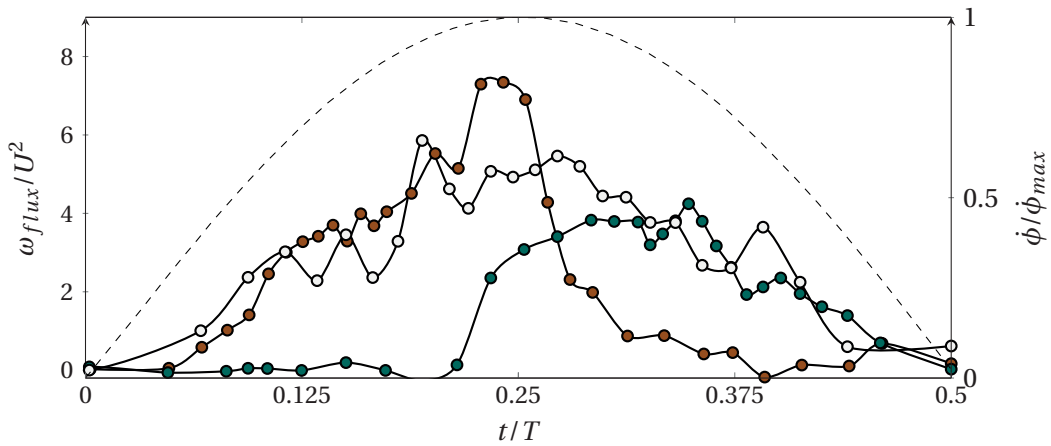


Figure 3.59 – Vorticity flux at the leading edge for fully advanced ( $\text{---}\bullet\text{---}$ ), fully delayed ( $\text{---}\bullet\text{---}$ ) and symmetric rotation ( $\text{---}\circ\text{---}$ ).

extents. However, in the fully delayed rotation the wing maintains a constant  $\alpha$ , which is relatively conducive for the vorticity generation even at low stroke velocities. The vorticity flux comparison towards the end of the half-stroke of advanced and delayed rotations shows that the vorticity flux is higher in delayed rotation (figure 3.59—●—). The maximum vorticity generated during the entire half-stroke is higher in the advanced and symmetric rotation compared to delayed rotation. While the vorticity flux is negligible for advanced rotation when the stroke velocity is less than 50 % of the maximum towards the end of the half-stroke, the delayed rotation shows a relatively slow decline in the vorticity generation, on par with the symmetric rotation.

#### 3.4.4 Summary of flow stages in slow rotation

##### Advanced rotation

The unsteady flow development in the advanced rotation cases with a slow flip is presented in figure 3.60. The distinction between stages is not clear in the advanced rotations, especially in the beginning of the half-stroke. The LEV emerges amidst large regions of remnant vorticity from the previous stroke (figure 3.60(a)). A surge-like behaviour is observed due to the constant angle of attack at the beginning of the half-stroke. The LEV binds to the wing and grows in the chord-wise direction in the first stage: **LEV emergence and growth** (figure 3.60(b)-(c)). The first stage is accompanied by a starting vortex at the trailing edge which convects away at the end of the first stage (figure 3.60(b)). The LEV then lifts-off of the wing transitioning into the second stage: **LEV lift-off**, and continues to grow in the chord-normal direction (figure 3.60(d)). The detached LEV grows larger and exhibits a circular shape through out this stage. The large LEV is held on close to the wing by a band of vorticity at the leading edge, which is the defining characteristic of the LEV in the advanced rotation (figure 3.60(e)-(g)). A strong secondary vortex is formed between the wing and the main LEV which is further pulled into the growing LEV (figure 3.60(g)). The lift-off of the LEV is accompanied by the shedding of compact, multiple trailing edge vortices unlike all other cases (figure 3.60(f)). The LEV then breaks down into multiple vorticity concentrations close to the stroke reversal to reach the final **LEV breakdown** stage (figure 3.60(h)). A strong TEV sheds from the wing at the end of the third and final stage.

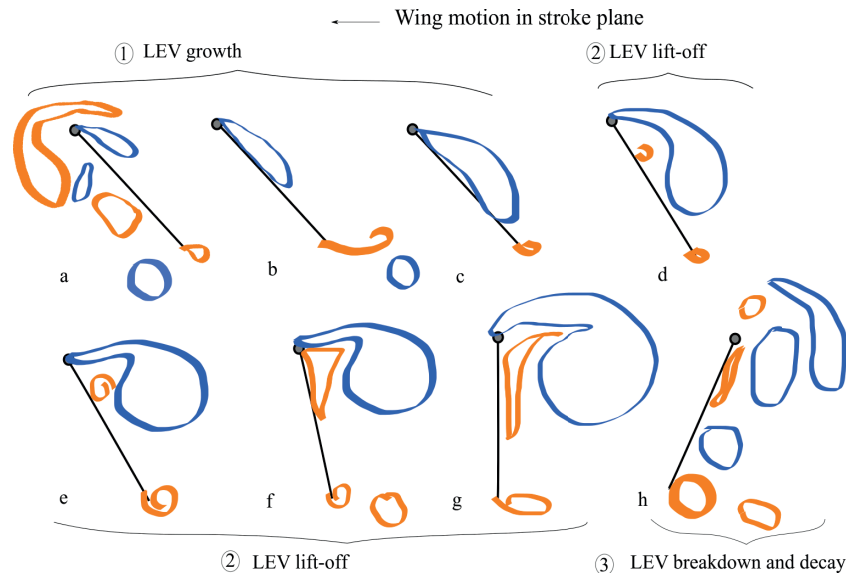


Figure 3.60 – Characteristic flow development in a flapping cycle with advanced, slow wing rotation. The wing moves to the left. The illustration of the features are based on vorticity. Blue features are indicative of the LEV and orange are indicative of the TEV.

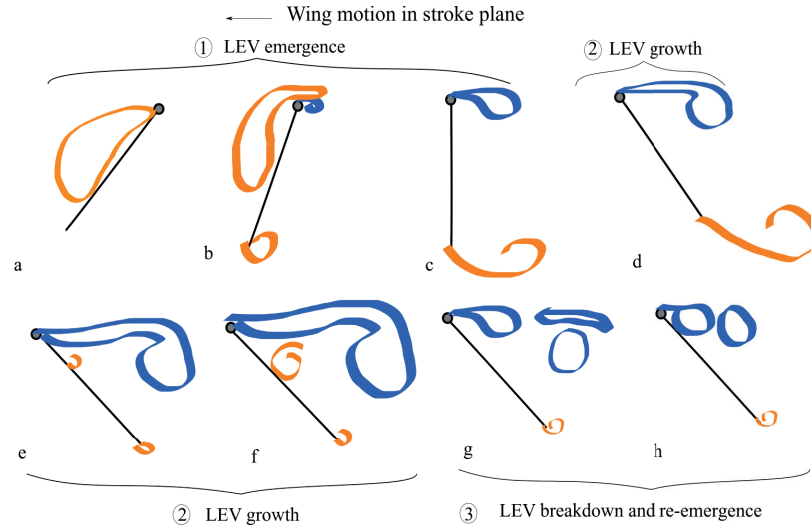


Figure 3.61 – Characteristic flow development in a flapping cycle with delayed, slow wing rotation. The wing moves to the left. The illustration of the features are based on vorticity. Blue features are indicative of the LEV and orange are indicative of the TEV.

### Delayed rotation

The unsteady flow development in the delayed rotation cases with a slow flip is different from other cases. The onset of the **LEV emergence** is delayed as the wing interacts with the large region of vorticity from the previous stroke as it rotates at the beginning of the half-stroke (figure 3.61(a)). The newly formed unbound LEV grows in the chord-normal direction (figure 3.61(b)). The end of LEV emergence stage is characterised by the convection of the strong starting vortex at the trailing edge away from the wing. The LEV in the delayed case does not bind to the wing and continues to grow in the chord-normal direction which characterises the **LEV growth stage** (figure 3.61(d)-(f)). The LEV strength decreases close to the end of the half stroke and splits into multiple weak vorticity concentrations (figure 3.61(g)). This heralds the third and final stage of the flow development in the delayed rotations : **LEV breakdown and re-emergence**. At the same instant, multiple strong and compact LEV is shed from the leading edge (figure 3.61(h)). A compact TEV is observed closed to the end of the cycle. The shed LEVs remain close to the wing and at the end of the half stroke, the multiple concentrations settle on the wing as a single feature.

The flow stages in the slow flip case are compared through the tangential velocity plots for each case in advanced, symmetric and delayed rotation (figure 3.62). In general, the first stage in the advanced rotation lasts longer than in the delayed and symmetric cases. During the first stage, the LEV emerges and immediately grows in the chord-wise direction. This stage is characterised by a downward tangential velocity along the chord that signifies a mostly bound flow. This is more apparent in the least and partially advanced rotations, indicating that the LEV is more tightly bound to the wing in these cases. The second stage : LEV lift-off indicates a reverse flow that is most prominent around the half-chord. The fully advanced



### 3.4. Influence of rotational timing for slow wing rotation

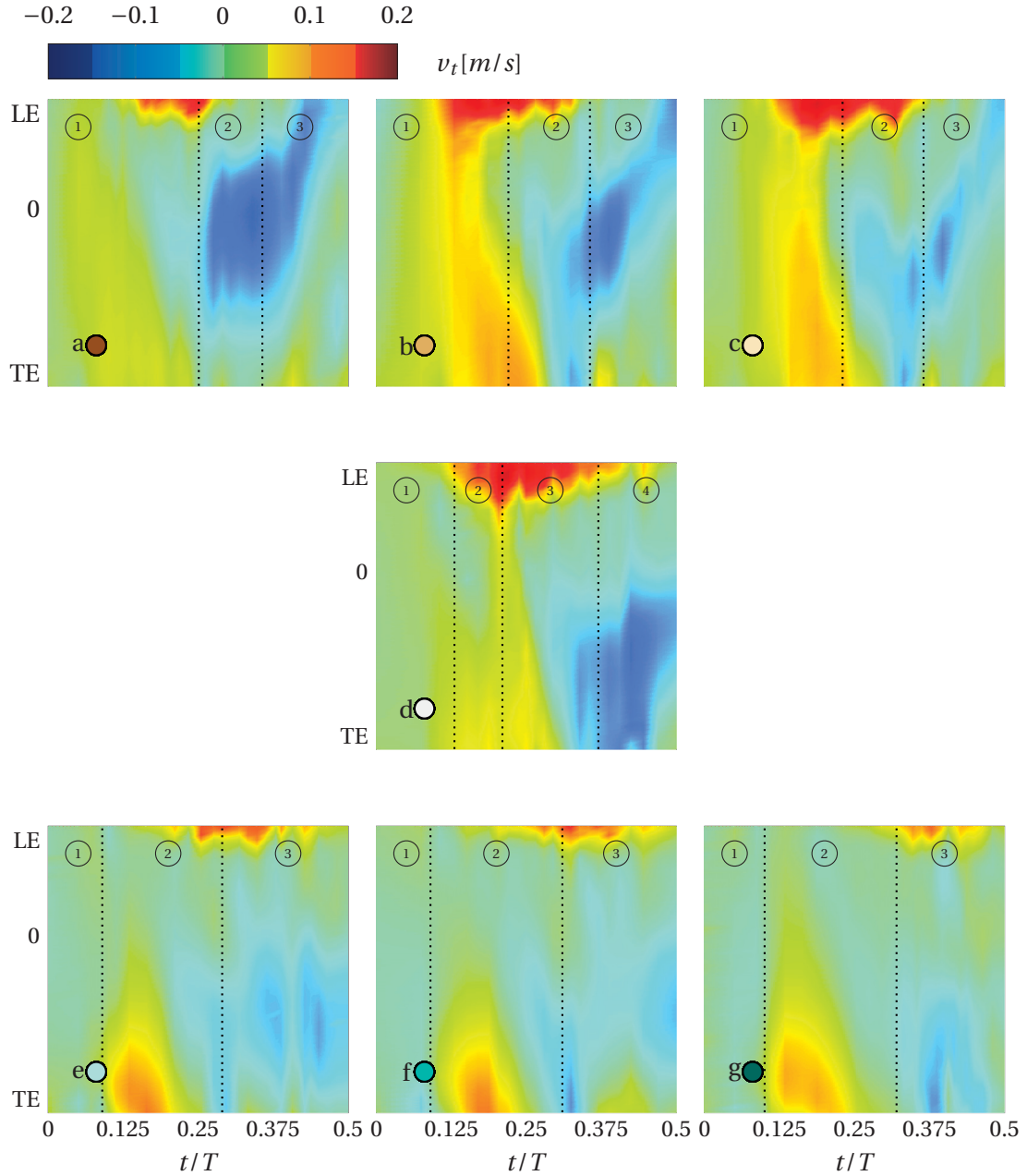


Figure 3.62 – Tagential velocity plots for (a) fully advanced , (b) partly advanced (c) least advanced (d) symmetric (e) least delayed, (f) partly delayed (g) fully delayed rotations. Warm colors signify a downward velocity along the chord (LE to TE) and cold colors signify upward velocity (TE to LE).

rotation sees the strongest upward tangential velocity (figure 3.62(a)). This feature decreases with decrease in advancement of rotation (figure 3.62(a) to (c)). The third and final stage of the flow development in the advanced rotations show an almost fully reverse flow along the chord up to the leading edge. This correlates with the negative angle of attack in the final stage when

the LEV is pushed upwards by the rotating wing, initiating a breakdown. In all the advanced cases, the wing has rotated to a negative angle of attack which results in the breakdown of LEV, secondary vortex and the movement of the oppositely signed TEV upwards.

The symmetric rotation (figure 3.62(d)) is characterised by LEV emergence where a chord-normal growth of the LEV is observed. The LEV then binds to the suction side of the wing and grows along the chord in the second stage: LEV growth. The third stage is characterised by the LEV lift-off and shows a strong region of reverse flow from the trailing edge, which continues well into the fourth stage : LEV breakdown and decay.

In the delayed rotations, the LEV is never bound to the wing. The wing rotation in the opposite direction of the stroke motion enforces a relatively strong downward tangential velocity in the second stage. In the delayed rotations, the strength of the reverse flow is lesser compared to the other cases since the LEV is further away from the wing and thereby has relatively lesser influence on the fluid at the wing ((figure 3.62(e) - (g))).

#### 3.4.5 Circulation

The flow fields for advanced and delayed phase-shifts for a slow rotation show interesting variations from the typical symmetric rotation. Unlike the fast rotation where the changes in the flow fields are nearly absent for different rotational phases, the slow flip clearly plays an important role in the evolution of the flow. To substantiate this better, comparisons of important parameters such as circulation is presented in this section and the aerodynamic forces in the next.

The comparison for maximum LEV circulation for variations in slow rotation is presented in figure 3.63. The maximum circulation decreases from fully advanced to symmetric rotations whereas in the delayed rotations, the maximum LEV circulation remains nearly constant. The maximum LE vorticity at the same time instants as maximum circulation is presented by the purple markers. The maximum LE vorticity decreases from fully advanced to symmetric rotation. The symmetric rotation shows the least maximum LE vorticity and the delayed rotations in general show the highest vorticity. The maximum LEV circulation in a flapping cycle is observed after the maximum stroke velocity instant, during wing deceleration in stroke. In case of delayed rotations, the maximum circulation is reached earlier, closer to the maximum stroke velocity ( $3 \leq t^* \leq 3.5$ ). And in cases of symmetric and advanced rotations, it occurs slightly later, closer to the stroke reversal ( $3.5 \leq t^* \leq 4$ ).

The flow fields at the instant of maximum circulation are indicated in figure 3.64. In the advanced rotations, the maximum LEV circulation is observed during the wing rotation, close to the end of the stroke. The LEV is unique in the fully advanced rotation where a very large unbound LEV is seen in the wake of the rotated wing (figure 3.64(a) ●). The other advanced

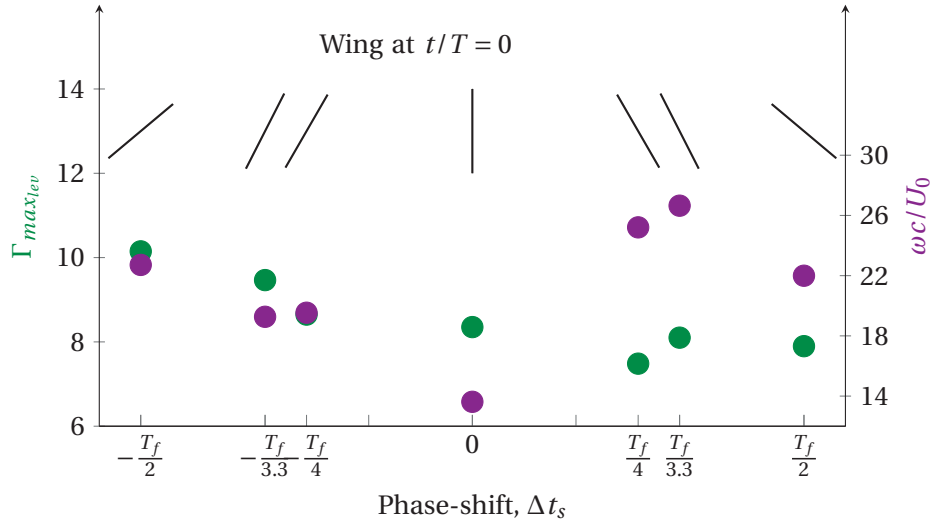


Figure 3.63 – Maximum LEV circulation (green) and maximum vorticity (purple) at the same time instant as maximum circulation for variations in the phase-shift for slow rotation. The black bars on the top represent the angle of attack at the beginning of the half-stroke.

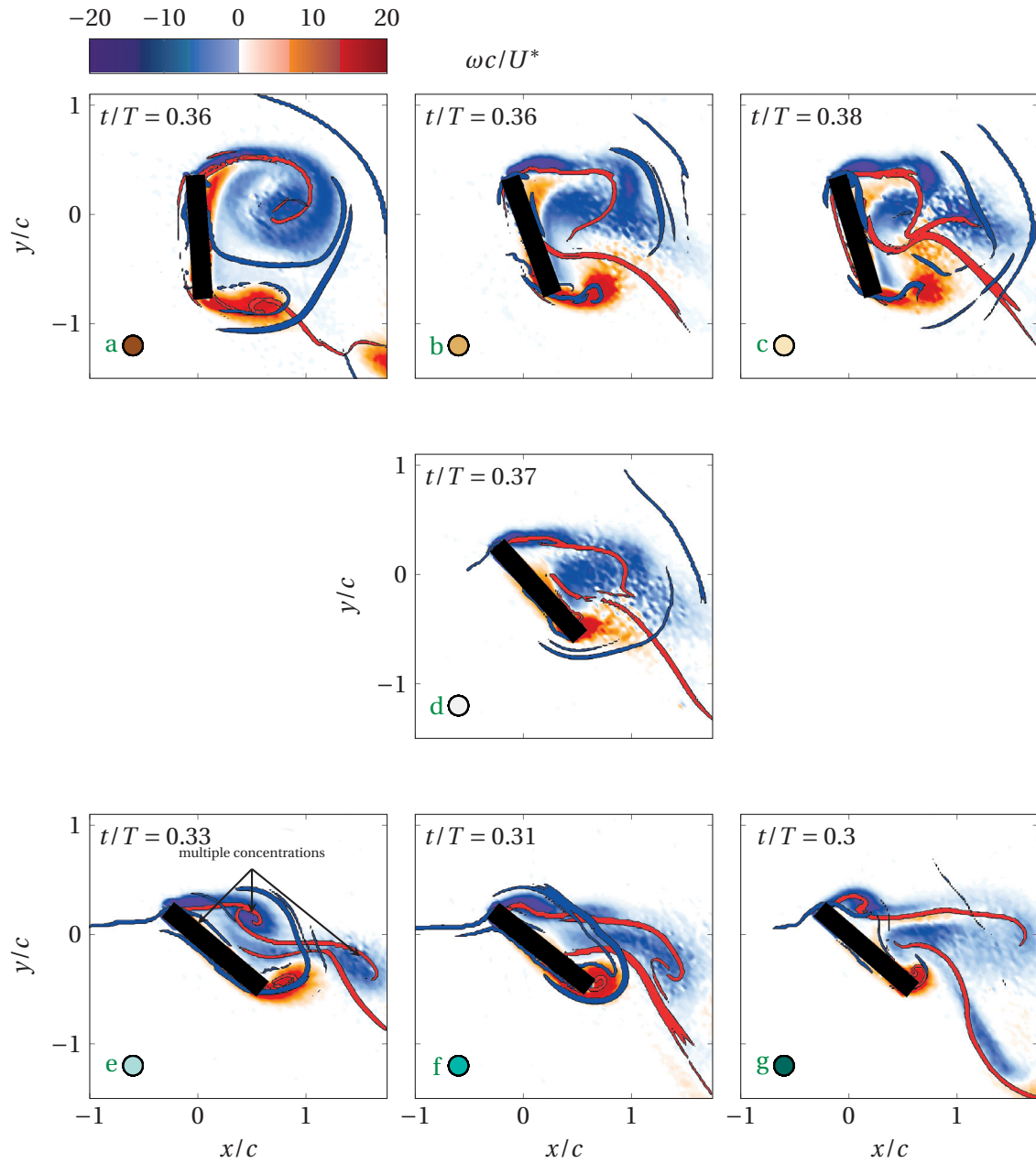


Figure 3.64 – Flow fields at maximum circulation for (a) fully advanced (b) partly advanced (c) least advanced (d) symmetric (e) least delayed (f) partly delayed (g) fully delayed rotations during slow rotation

### 3.4. Influence of rotational timing for slow wing rotation

---

cases whose phase-shifts are close to each other show large, bound vortical features from the leading edge at nearly identical wing positions (figure 3.64 (b), (c)). This large area of the strong vorticity contributes to large values of circulation. The decreasing stroke velocity decreases the vorticity production at the leading edge. The relatively smaller area of the LEV combined with lower vorticity, produces lower circulation.

In symmetric rotation, the maximum LEV circulation is observed during pure translation. The symmetric rotation shows a well defined, relatively compact structure with lower vorticity than the advanced rotations (figure 3.64(d)). The maximum LEV circulation occurs just before the rotation commences close to stroke reversal.

The delayed rotations show multiple but compact regions of strong vorticity that have travelled up to 1.5 chord lengths away from the axis of rotation (figure 3.64 (e),(f), (g)). The maximum circulation in these cases occurs after the rotation has ended. This occurs at the fourth stage of the flow cycle when multiple, compact LEV emerge and shed. The difference in the sizes and vorticity distribution can be attributed to the variations in rotational phase.

### 3.4.6 Effect of rotational timing on the aerodynamic forces

The general lift force distribution in a half-stroke for the representative phase-shifts with the slower flip duration exhibit similar, roughly sinusoidal lift distribution over the flapping cycle. A noteworthy trend in these curves is that the least lift occurs during wing rotation in each case. For advanced rotation cases, the least lift occurs before the stroke reversal (close to  $t/T \approx 0.375$ ). For delayed rotation cases, the least lift is produced at the beginning of the half-stroke ( $t/T \approx 0.125$ ). This correlates to the angle of attack ( $\alpha$ ) of the wing at the beginning of the half-stroke. In advanced rotations, larger lift values are observed even at the beginning of the half-stroke due to a favorable and constant  $\alpha$  that promotes a mostly uninterrupted LEV formation and growth. In delayed cases, the wing has a negative  $\alpha$ . This reduces the lift produced even as the wing accelerates at the beginning of the half-stroke. The delayed rotations are characterised by an unbound and multiple LE vortical concentrations throughout the half-stroke, which results in the overall reduction in the lift.

The general drag distribution in a half-stroke for the representative phase-shifts with the slower flip duration exhibit similar, roughly sinusoidal lift distribution over the flapping cycle (figure 3.66). The advanced rotation produces the highest maximum drag, close to maximum stroke velocity ( $t/T = 0.25$ ). The delayed rotation produces its maximum earlier in the half-stroke at about  $t/T = 0.15$ . This follows from the rotational phase of the wing at the beginning of the half-stroke. The symmetric rotation approximately produces the least maximum drag.

The details of the lift and drag behaviour during hovering with slow wing rotation for all phase-shifts are presented in this section.

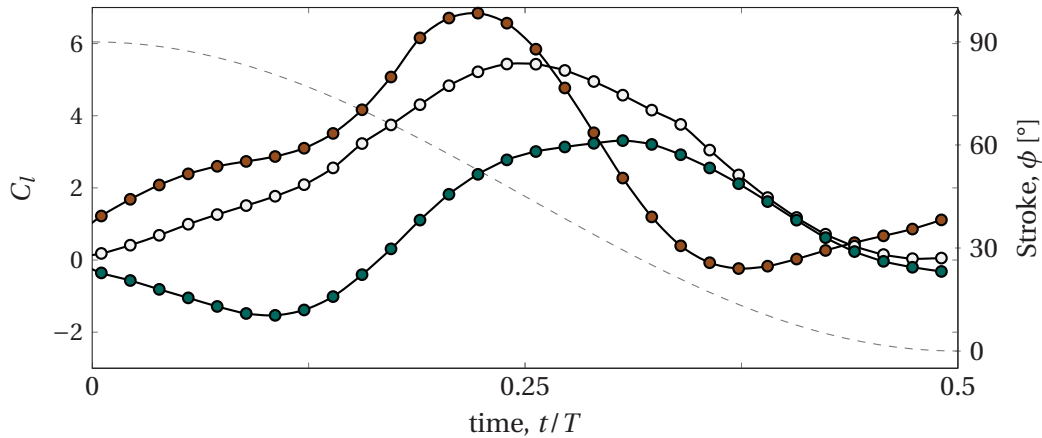


Figure 3.65 – Lift evolution in half-stroke for all variations of phase-shift  $\Delta t_s$ , for the slow flip duration. Fully advanced —●—, Symmetric —○—, fully delayed —●— rotations

### 3.4. Influence of rotational timing for slow wing rotation

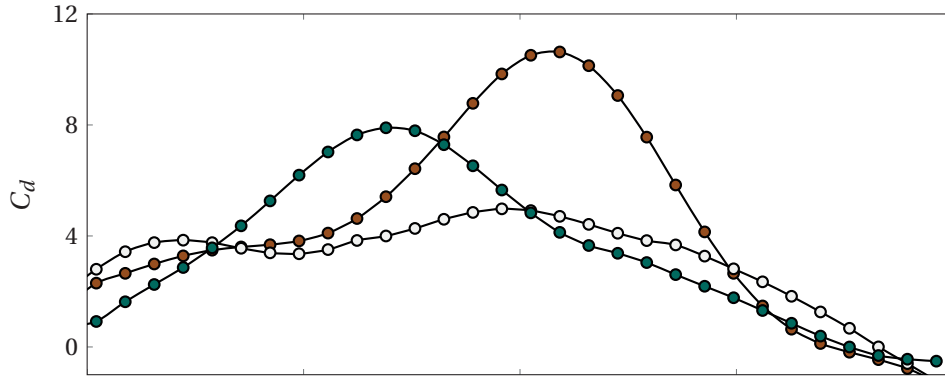


Figure 3.66 – Drag evolution in half-stroke for representative variations of phase-shift  $\Delta t_s$ , for the slow flip duration. Fully advanced —●—, Symmetric —○—, fully delayed —●— rotations

#### Lift

The trends for the mean and maximum lift produced versus phase-shifts ( $\Delta t_s$ ) is presented in figure 3.67. The mean lift ( $\star$ ) is nearly the same for all cases except fully delayed rotation, which is slightly lower. The maximum lift produced decreases from most advanced to most delayed rotation cases. In other words, the maximum lift produced in the symmetric rotation is lower than that of advanced rotations and higher than that of delayed rotations. This agrees with the findings of earlier studies [69, 1]. Taking this finding a step further, the time instant at which the maximum lift occurs is presented in the figure 3.68. The maximum lift occurs close to the maximum stroke velocity,  $(\frac{d\phi}{dt})_{max}$ , indicated by the dashed line in figure 3.68. The maximum lift occurs the earliest in the fully advanced case, before the instant of maximum stroke velocity

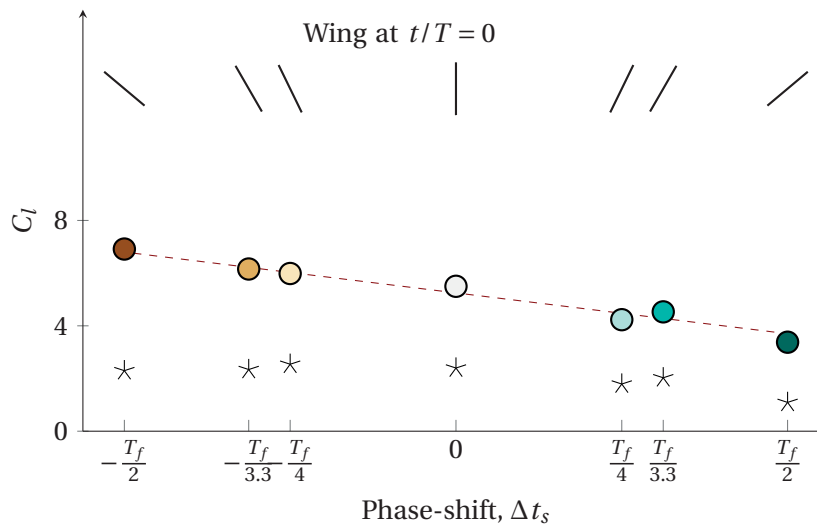


Figure 3.67 – Maximum lift (circles) and mean lift (stars) trends for variations in the phase-shift for the slow rotation. The black bars on the top represent the angle of attack at the beginning of the half-stroke.

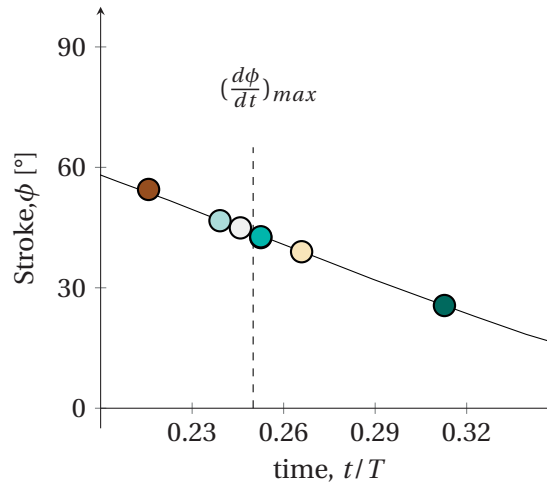


Figure 3.68 – The time at which maximum lift occurs for the slow rotation in a half-stroke.

(●). The maximum lift in the half-stroke is delayed the most in the fully delayed rotation (●). In the advanced rotations, maximum lift produced in the half-stroke is delayed with decrease in advancement of the rotational phase. Whereas in delayed rotations, maximum lift produced in the half-stroke is delayed with increase in delay of the rotational phase.

The corresponding flow fields at maximum lift for each of the phase-shifts are presented in figure 3.69. In the advanced rotation cases, the nFTLE (red) ridges clearly indicate recognisable LEV in the lift-off stage (figure 3.69 (a)-(c)). The nFTLE ridge rolls up close to three-quarters of the chord indicating the boundary of the well developed LEV. The vorticity strength decreases from the most advanced (a ●) to least advanced rotation (○). For the most advanced rotation case, the maximum lift is achieved just after the wing begins to rotate in the half-stroke (figure 3.69(a ●)). The surge like motion created by the wing at the beginning of the half-stroke in the most advanced rotation case, causes continuous vorticity generation and accumulation close to the wing, forming a bound LEV in the first stage of the flow cycle. This head-start in terms of LEV development in the beginning of the half-stroke leads to higher lift in terms of magnitude and timing than in other cases. Just before the maximum stroke velocity is reached, the wing begins to rotate at  $t/T = 0.22$  resulting in the lift-off of the LEV from the surface of the wing and causing a decline in the lift produced after this point. The strong vorticity combined with a relatively small angle of attack ( $\alpha$ ) of the wing moving at high velocity in the stroke plane is the reason for the highest lift produced among all rotation cases. The lift drops after this point due to a large  $\alpha$ , in which case, the wing acts like a bluff-body.

In the other two advanced rotations the wing is at the end of pure translation at the instant of maximum lift produced, owing to the smaller advancement in rotation (figure 3.69 (b ○), (c ○)). In these cases, the LEV emergence stage is slightly delayed because at the beginning of the half-stroke the wing is yet to finish a part of the rotation, which slows the vorticity accumulation and results in an unbound and spread LEV. Eventually as the translation phase sets in, the LEV binds to the wing and grows in the chord-normal direction. As the wing



### 3.4. Influence of rotational timing for slow wing rotation

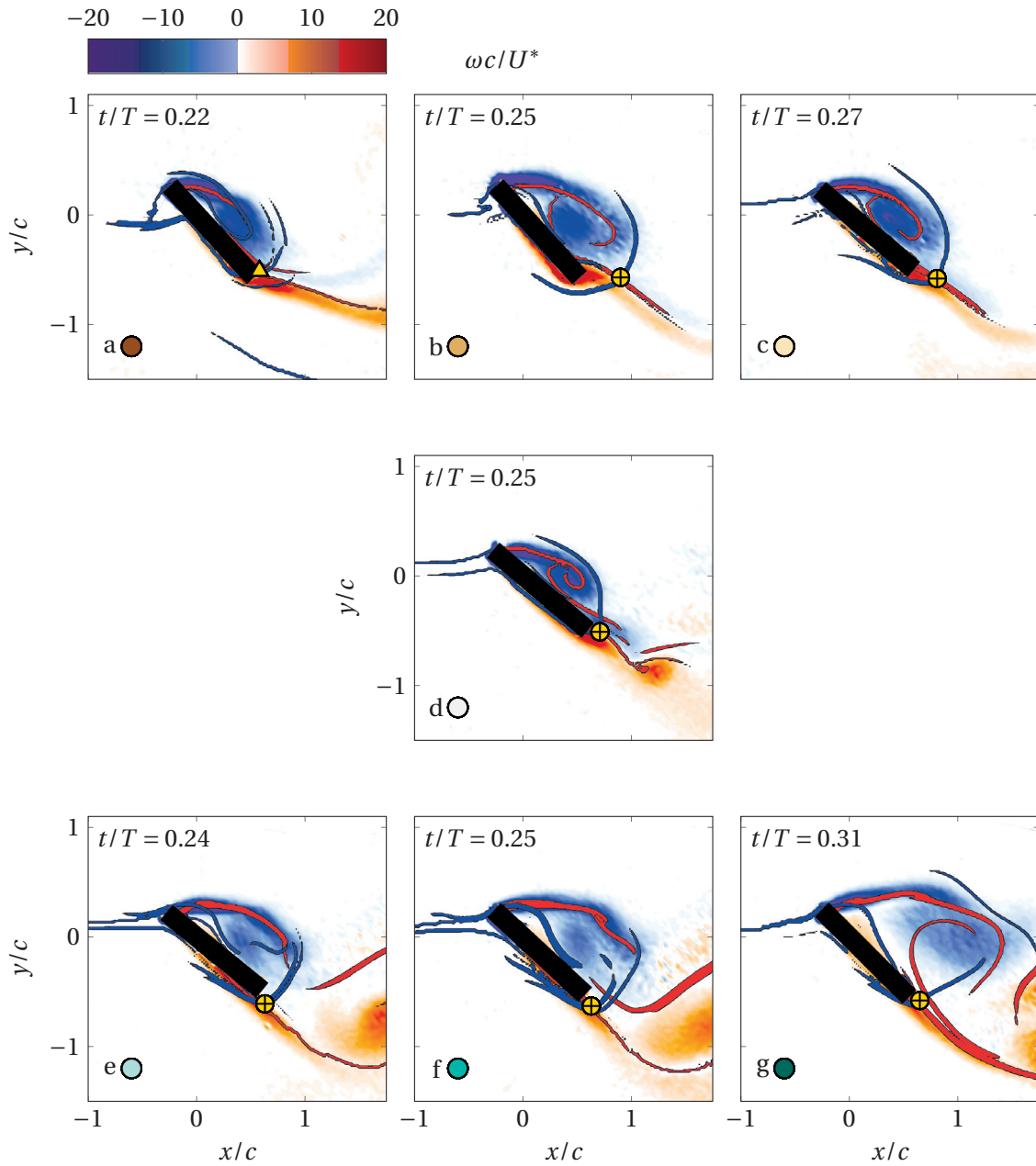


Figure 3.69 – Flow fields at maximum lift for (a) fully advanced (b) partly advanced (c) least advanced (d) symmetric (e) least delayed (f) partly delayed (g) fully delayed. The time instant in the flapping cycle ( $t/T$ ) for the given flow field is included in each panel.

begins to rotate close to maximum stroke velocity, the LEV detaches from the wing and results in the decrease in lift. This behaviour, along with the most advanced rotation case, shows that the slow rotation definitely influences the lift production. Thereafter, the wing rotation close to maximum stroke velocity results in the enlargement and subsequently breakdown of the LEV causing the lift to drop (figure 3.69(b ●), (c ○)). In these two cases, the size and strength of the vortical features are different despite the smaller difference in the phase-shifts. The boundaries of the LEV indicated by the nFTLE ridges (red) show that the least advanced rotation case exhibits the largest structure with weakest vorticity compared to the other cases. This could contribute to the fact that least advanced rotation produces the lowest maximum lift amongst advanced rotations. The maximum also occurs after the maximum stroke velocity has passed coinciding with the start of the rotation. Thus the relatively small angles of attack, combined with little or no disruption during acceleration in the form of wing rotation allows for the generation of large lift values.

The symmetric rotation for the slower flip duration case shows a bound LEV at mid-translation, corresponding to the maximum stroke velocity. It is also observed that the saddle lifts off at this instant showing a dependence on the stroke velocity in symmetric rotation similar to the fast flip. The combined effect of the wing's maximum stroke velocity and the sustained build up of the vorticity, produces maximum lift. It can be noted that the vorticity magnitude is lower compared to the advanced rotation cases which could explain the relatively lower lift produced in the symmetric case. Soon after, the stroke velocity begins to drop causing the vorticity strength to decrease even as the size of the structures increase, as described in detail in section 3.4. This suggests that in the case where the flow isn't perturbed by the wing rotation close to the maximum stroke velocity, lift primarily depends on the stroke velocity, similar to that of the fast rotation (section 3.3.3).

The maximum lift in the delayed rotation cases is observed when the wing translates with a constant  $\alpha = 40^\circ$ . In case of delayed rotation (figure 3.69(e ○), (f ●), (g ●)), the size of the structures identifiable by the nFTLE ridges (red) on the suction side are larger in general compared to the advanced and symmetric rotation cases. In all the three delayed rotation cases, the large unbound LEV is caused due to the rotation of the wing as it accelerates in the beginning of the half-stroke. This LEV grows in the chord-normal direction without binding to the wing. Upon the completion of wing rotation, the single large LEV is split into multiple components. It is just before this breakdown that the maximum lift is observed. The size and strength of the observed structures vary due to the differences in the rotational delay. With increasing delay in rotation (from (e ○) to (g ●)) and the distance of the outermost boundary point of the structures from the chordline increases. The decreasing vorticity strength as well as the proximity to the wing probably contributes to the decrease in the maximum lift values produced. In the least delayed rotation (e○), the wing has rotated for a shorter period at the beginning of the half-stroke and mostly rotates in the direction of the stroke. This allows the formation of a stronger LEV, closer to the wing. Prominent secondary vortices are observed in all three delayed rotation cases as expected.

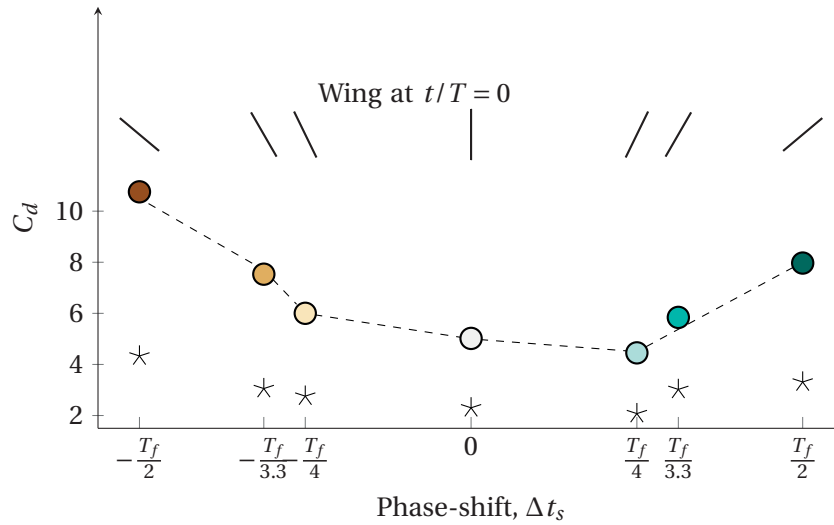


Figure 3.70 – Maximum drag (circles) and mean drag (stars) trends for variations in the phase-shift for the slow rotation. The black bars on the top represent the angle of attack at the beginning of the half-stroke.

The most delayed rotation case shows a near circular, unbound LEV with low vorticity (figure 3.69(g ●)). The center of this structure at about  $x/c \approx -1$  is furthest away from the wing. This is caused because of the entire wing rotation occurring after the stroke reversal. The LE rotates from a negative to a positive  $\alpha$  pulling the LEV in its wake in an elongated arc until the rotation ends. As the wing approaches the end of rotation and the stroke velocity is also decreasing, vorticity accumulated over the suction side enlarges and follows the wing before disintegrating shortly thereafter. The lowered influence of the LEV on the wing contributes to the the least maximum lift observed in the most delayed rotation case. The fact that the wing rotates at the beginning of each half-stroke for all the delayed rotation cases, causes a bluff-body like situation during wing acceleration, lowering the overall lift produced during the flapping cycle. This results in delayed production of maximum lift compared to symmetric and advanced rotation cases.

#### Drag

Unlike the continuous decrease in maximum lift produced from fully advanced to fully delayed rotations with slow flip duration, the maximum drag shows a roughly 'U' trend from the most advanced to most delayed rotation cases (figure 3.70). The mean drag also follows a similar trend although the variations is not easily discernible. The maximum drag produced decreases from fully advanced to least advanced rotation as well as fully delayed to least delayed rotation cases. The timing of this maximum drag in the flapping cycle also shows a trend where all the delayed rotation cases, produce maximum drag much earlier than the maximum stroke velocity instant (figure 3.71). And the advanced rotations produces maximum drag after the maximum stroke velocity instant has passed; so during deceleration of the wing in the stroke

plane. The maximum drag during symmetric rotation occurs almost exactly at the maximum stroke velocity ( $t/T = 0.25$ ).

The flow fields at the time instant when maximum drag is produced indicate that high drag values occur at large geometric angles of attack,  $\alpha$  (figure 3.72). Evidently, the maximum drag produced in all cases except the symmetric rotation case (figure 3.72(d ○)), is during the wing rotation when the wing behaves like a bluff body. The maximum drag during symmetric rotation however occurs mid-transition at the same time instant as the maximum lift. This once again suggests that if the flow field is unperturbed by wing rotation around the maximum stroke velocity, it results in the maximum aerodynamic forces, leading to the conclusion that the aerodynamic forces in such case, depends primarily on the stroke velocity.

In the advanced rotation cases (figure 3.72((a ●),(b ●),(c ○))), a circular large anti-clockwise rotating leading edge structure is visible on the suction side of the wing with distinct clockwise rotating trailing edge vortex in each case. The LEV increases in size and decreases in vorticity from fully advanced to least advanced rotation cases (from (a ●) to (c ○)). The chord-normal height increases with decreasing advancement in rotation. The distance between the centers of these structures and the leading edge increases with decreasing advancement in rotation. The distance between the centers of these structures and the centers of the trailing edge vortices decreases with decreasing advancement in rotation. In the fully advanced rotation, the saddle at the trailing edge has just lifted off. The  $\alpha$  at which maximum drag occurs decreases with decreasing advancement of rotation. The stroke velocity at which maximum drag occurs decreases with decreasing advancement of rotation. In all the three advanced rotation cases, the drag continues to build up during pure translation which occurs at the start of the half-stroke. The wing rotation combined with the deceleration in the stroke plane causes delayed maximum drag production in the flapping cycle. In all the three cases, the maximum drag is produced just after the rotation begins close to the end of the half-stroke and before the LEV breaks down.

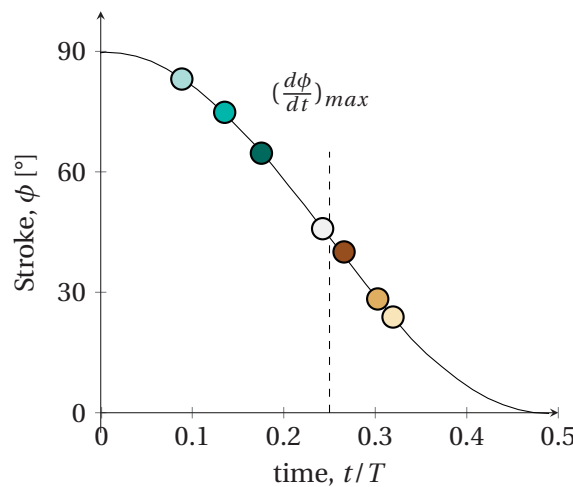


Figure 3.71 – The time at which maximum drag occurs for the slow rotation in a half-stroke.

### 3.4. Influence of rotational timing for slow wing rotation

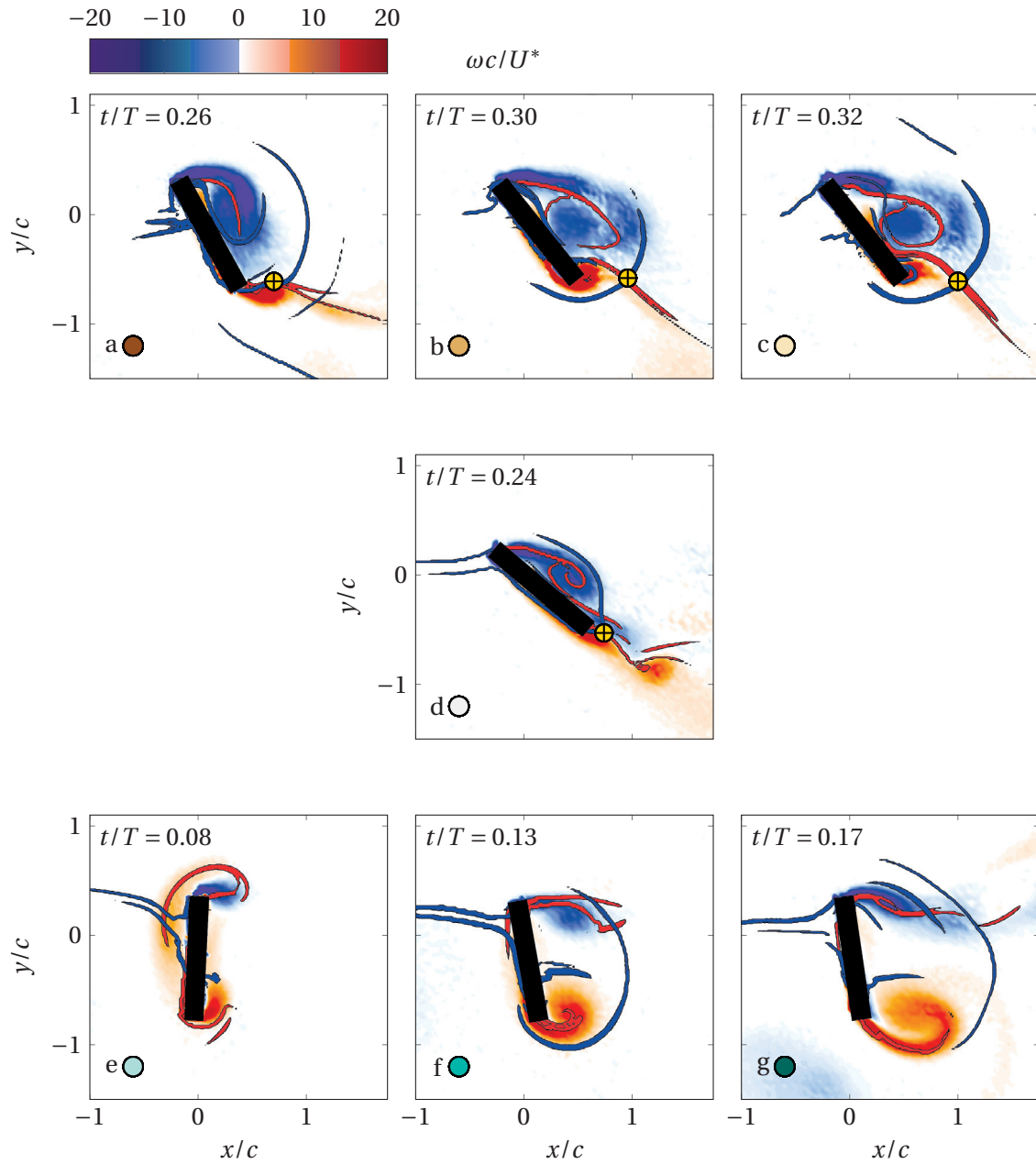


Figure 3.72 – Flow fields at maximum drag for (a) fully advanced (b) partly advanced (c) least advanced (d) symmetric (e) least delayed (f) partly delayed (g) fully delayed. The time instant in the flapping cycle represented by the flow field is included in each panel ( $t/T$ ).

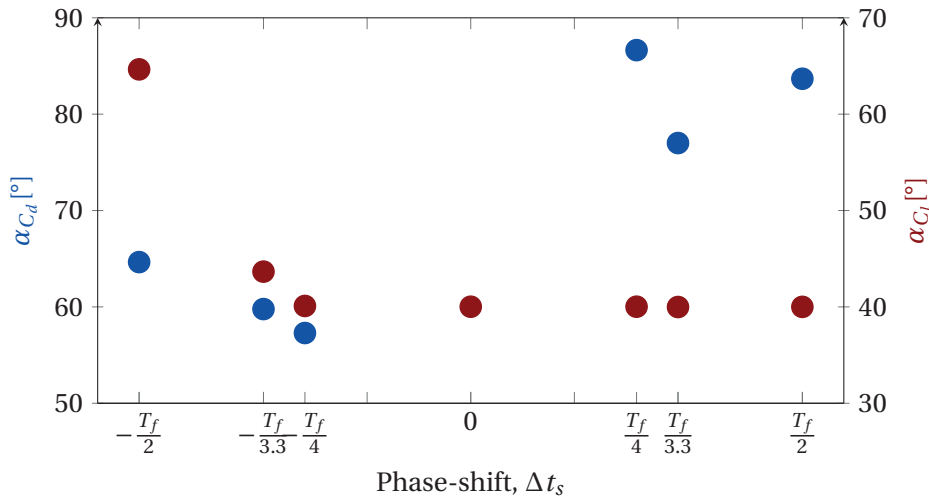


Figure 3.73 – The geometric angle of attack ( $\alpha^\circ$ ) at which maximum lift and maximum drag occurs for the slow rotation

In the delayed rotations, the clockwise vorticity concentrations are very small and close to the top of the wing (figure 3.72(e)  $\odot$ , (f)  $\odot$ , (g)  $\bullet$ ). The flow features are unbound and appears like a band of vorticity attached to the leading edge. This band of vorticity is longer for increased delay in rotational phases. Evidently, the  $\alpha$  at which maximum drag occurs in the delayed rotations are nearly the same. The wing behaves like a bluff body due to the early  $90^\circ$  angle of the wing combined with an increasing stroke velocity. All three cases show a rotating starting vortex at the trailing edge that lowers in strength and moves away from the wing with increase in rotational delay. This causes the wing to reach maximum drag values before the maximum stroke velocity is reached in the delayed rotation. The stroke velocity at which maximum drag occurs in the delayed rotation cases increases with increase in rotational delay.

### Effect of angle-of-attack

The angle of attack at which maximum lift and drag occur during slow flip are summarised in figure 3.73. Maroon symbols represent  $\alpha$  at maximum lift and blue symbols represent  $\alpha$  at maximum drag. This suggests that the aerodynamic forces in case of slow rotation are dependent on the rotational phase, which determines the angle of attack and not just on the stroke velocity as seen in the fast rotation.

Maximum lift in most cases is observed at  $\alpha \approx 40^\circ$ . The exceptions are partly advanced and fully advanced rotations, when the influence of rotation is clearly observed. In these cases, the mostly undisrupted flows in the first stage results in high lift at the start of the half-stroke. The lift production is interrupted due to rotation, observed by the larger  $\alpha \approx 65^\circ - 85^\circ$ . In all other cases where the wing rotates at the beginning of the half-stroke, the maximum lift is delayed.

The maximum drag in delayed rotation is produced when the wing behaves like a bluff body

### **3.4. Influence of rotational timing for slow wing rotation**

---

at large  $\alpha \approx 60^\circ - 70^\circ$ , earlier in the half-stroke when the wing moves with an increasing stroke velocity. Maximum drag in the advanced rotation occurs when the wing just begins to rotate after the initial surge like motion is completed, after the maximum stroke velocity has passed. The surge like motion creates a favourable condition delaying the drag production in advanced cases. The maximum drag occurs after the maximum stroke velocity has passed, which suggests that the drag production in the slow flip is not dependent only on the stroke velocity but also the rotation.





## 4 Summary and conclusions

Biological locomotion in fluids is dominated by the formation and shedding of organized vorticity, which is correlated with the aerodynamic forces produced. In-depth knowledge of the vortex dynamics in unsteady flows will help create better designs of flow control surfaces for unsteady environments. This bio-inspired study deals with hovering flight in insects. Wing rotation is one of the key kinematic features in hovering flight and is classified into advanced, delayed and symmetric rotation based on the phase relation with the stroke. This phase relation, quantified by phase-shift ( $\Delta t_s$ ), and the duration of rotation ( $T_f$ ) are together referred to as rotational timing. The objective is to study the effect of rotational timing on the flow and force characteristics of a hovering flat plate wing.

The investigation was carried out experimentally. Planar particle image velocimetry was conducted on a model flat plate wing for a Reynolds number of  $Re = 220$  and reduced frequency  $k = 0.32$ . The experimental set-up was built from ground up as a part of this study and included a flapping mechanism that was programmed to mimic hoverfly kinematics. A load cell was added to obtain direct force measurements of the flapping cycle. The flapping apparatus was synchronised with the image acquisition system via a trigger mechanism to obtain phase-locked particle images. The acquired images were then phase-averaged.

A Lagrangian approach was used to analyse the phase-averaged flow fields, which has provided detailed insight into the vortex dynamics during hover. Codes were adapted to calculate the finite time Lyapunov exponent (FTLE), which were capable of using data that was not collected at uniformly spaced time steps. It has been shown that FTLE is a useful tool in analysing unsteady experimental flow fields by identifying dynamically relevant flow features such as the primary leading edge vortex (LEV), secondary vortices, topological saddles and their evolution in a flapping cycle.

The measured aerodynamic forces were correlated with the kinematics and the flow features to elaborate the effect of rotational timing on the hover characteristics.

### 4.1 Flow and force characterisation of a flapping cycle

To understand the effect of rotational timing on the flapping cycle, it is desirable to understand a typical flapping cycle. The symmetric rotation ( $\Delta t_s = 0$ ) with a "fast" rotation ( $T_f = T/6$ ) was taken as the base case, and is mainly characterised by a single large LEV that evolves throughout the entire half-stroke. The stages of flow evolution in a flapping cycle are differentiated as LEV emergence, growth, lift-off, and breakdown and decay. The bound LEV develops in the chord-wise direction, and then in the chord-normal direction before breaking down into multiple vortical features. The saddle lift-off from the trailing edge at maximum stroke velocity is the mechanism responsible for the LEV lift-off and onset of reverse flow over the wing. The LEV circulation increases during approximately 3.8 convective time scales before splitting into multiple vorticity concentrations. The end of the first rotation stimulates a change in the direction of the LEV growth while the second rotation triggers a complete breakdown of the LEV into multiple connected vorticity concentrations. The pure translation phase is characterised by a LEV that grows in size. The vorticity magnitude of the LEV is dependent on the stroke velocity. Two trailing edge vortices are observed in the flapping cycle: one when the pure translation phase starts and the other at the start of the rotation near the end of the half-stroke.

The aerodynamic forces generated by a hovering wing correlate with the vorticity production which is in turn dependent on the stroke velocity. The maximum lift and drag are observed when the LEV is bound and fully grown over the wing, just before the lift-off. The most prominent contribution to the lift comes from the bound LEV in the growth stage. The effect of wing rotation on the forces, especially on drag, is seen as a change in the gradient at the end of rotation in the first stage and beginning of rotation in the last stage. During these stages, the angle of attack is large and the wing behaves like a bluff body.

### 4.2 Effect of rotational phase on the flow and forces

The variations in the phase-shift for a fast rotation duration show similar flow development and thereby aerodynamic forces as the base case. The flow is characterised by a single LEV that goes through four stages of evolution as in the case of symmetric rotation. The major differences in the flow fields are seen in the first stage: LEV emergence, due to the history effects. The vorticity and thereby circulation of the LEV is highest in the advanced rotation and lowest in the delayed rotation. This is caused by the initial angle of attack of the wing. The advanced rotation starts with a positive and smaller geometric angle of attack and behaves like a surging wing. The delayed rotation starts with a negative rotational angle, which results in a delay in the generation of strong vorticity. The LEV emergence stage ends slightly earlier in the advanced rotation and ends later in the delayed rotation. The LEV growth and lift-off stages, occur at almost the same time for both advanced and delayed cases as for the symmetric case. This is substantiated by the saddle distance curves and the tangential velocity plots for the half-stroke. It coincides with the fact that during the growth and lift-off stages, the wing is in

pure translation, and thus with similar stroke velocities, the flow fields are very similar to each other. The end of the flapping cycle is characterised by the breakdown and decay. In the fully advanced and fully delayed cases, the vorticity is stronger at the end of the half-stroke despite the low stroke velocities. This is due to the decreased disruption by wing rotation. The lift and drag produced are similar in trend and magnitude. The maximum lift and drag in a cycle occur close to the maximum stroke velocity, similar to the symmetric rotation. This substantiates that the force generation is dependent on the LEV growth which, in turn, is mainly dependent on the stroke velocity.

Thus, for a fast wing rotation, the same overall flow development stages are observed but differences in the timing of stages are quantified. The aerodynamic forces are nearly the same and only slightly affected by the wing rotation if the rotation is fast.

### 4.3 Effect of rotational duration on the flapping cycle

The influence of rotational duration in a flapping cycle is investigated by comparing the flow and force development for a basic case of symmetric rotation during a fast wing rotation ( $T_f = T/6$ ) and slow wing rotation ( $T_f = T/3$ ). A similar LEV emergence stage is noticed in both cases, which is characterised by a chord-normal growth of the unbound LEV. When the rotational duration is doubled, the LEV emergence stage lasts about 60% longer but the LEV growth stage ends sooner and is characterised by a more compact LEV. The LEV breakdown occurs at nearly the same instant in both cases exhibiting nearly the same behaviour.

The force evolution in the slow and fast rotations are largely similar. However, the fast rotation produces higher maximum lift and drag compared to the slow rotation. The LEV growth stage is important for the generation of lift as observed by the large gradients present in both cases. The rate at which lift increases in the LEV growth stage is higher in the slow rotation compared to the fast rotation. The LEV lifts-off close to the maximum stroke velocity, beyond which lift and drag decrease, corresponding to a decrease in the stroke velocity. The duration of rotation thus influences the rate at which lift increases and the drag produced during wing acceleration.

### 4.4 Effect of rotational phase during slow wing rotation

The slow wing rotation exhibits distinct flow evolution patterns for varying rotational phase unlike the fast wing rotation. At different intervals during the half-stroke, the slow rotation alters the formation, evolution and breakdown of the flow structures. This is summarised in figure 4.1. In the advanced rotation, the LEV emerges and grows as a bound LEV along the chord at the start of the stroke. The advanced rotations show higher vorticity flux and LEV circulation due to the favourable and constant angle of attack at the start of the half-stroke when the stroke velocity is increasing. The most notable characteristic of this case is the large unbound LEV that grows in the chord-normal direction during wing rotation.

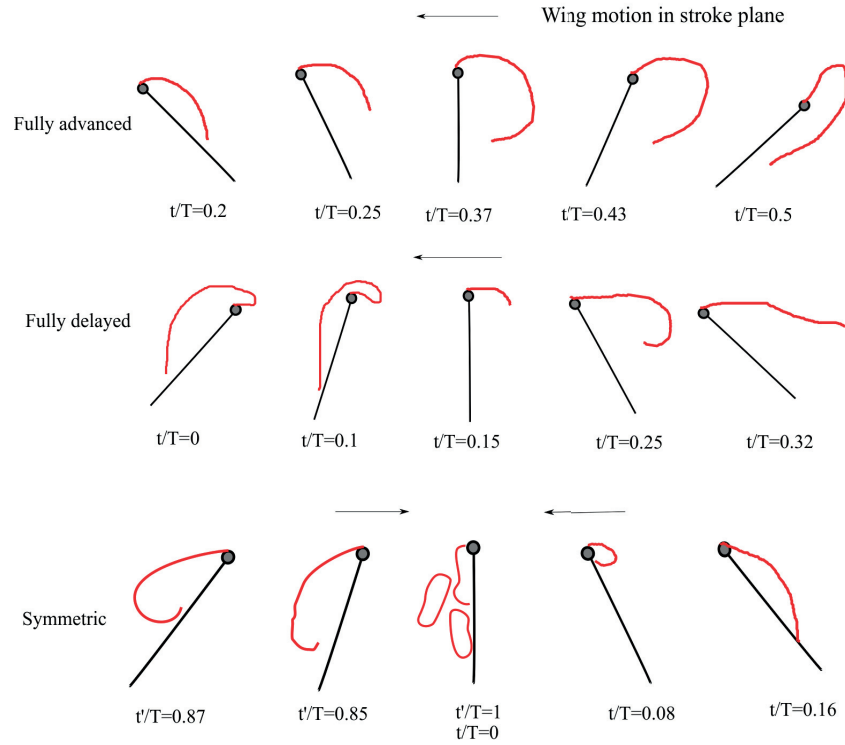


Figure 4.1 – Schematic of differences in LEV evolution based on the nFTLE ridges during slow wing rotation

In the delayed rotation, the wing rotates at the beginning of the half-stroke from a negative angle of attack. This means that the wing pushes through a strong region of remnant vorticity. The delayed rotation is characterised most notably by the unbound LEV that grows in the chord normal direction for most of the half-stroke. The last stage is characterised by the emergence of multiple, compact LEV at the leading edge instead of the breakdown of the existing LEV noticed in advanced and symmetric cases.

The maximum lift and drag characteristics for the three representative cases of the slow rotation is summarised in figure 4.2. The maximum lift decreases linearly for phase-shifts varying from fully advanced to fully delayed rotation, i.e from complete phase-lead to phase-lag. The maximum lift in the advanced rotations occurs when the wing starts to rotate after the initial surge-like motion that dominated the flapping cycle, causing the enlargement and breakdown of structures. The maximum lift in the delayed rotations occurs when the wing has almost completely rotated, just before the translation starts when the LEV breaks into multiple connected concentrations. In general, the maximum lift occurs close to the maximum stroke velocity. The differences in the timing and magnitude is due to the difference in the rotational phases.

The highest maximum drag occurs in the fully advanced rotation and the lowest is produced in symmetric rotation. The maximum drag decreases from fully advanced to least advanced

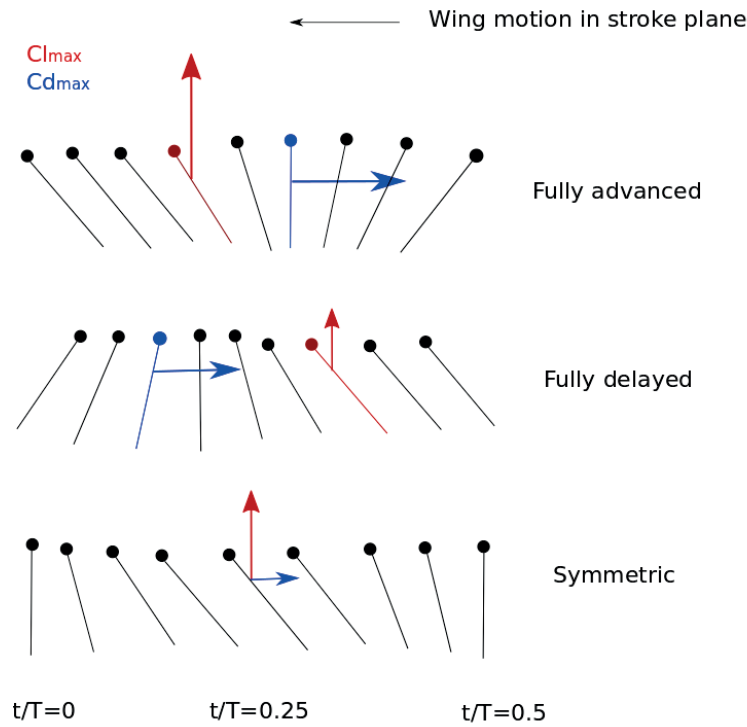


Figure 4.2 – General schematic representation of the wing rotation cases for a half-stroke. Maroon arrows indicate the magnitude and timing of the maximum lift in the half-stroke. Blue arrows indicate the magnitude and timing of the maximum drag coefficients for three representative cases.

rotation, and from fully delayed to least delayed rotation. In advanced and delayed rotations, the maximum drag produced is highest when there is a complete phase lead or lag with respect to the stroke, respectively. The maximum drag is produced when the wing behaves like a bluff body at large  $\alpha$  in the delayed rotations. The maximum drag in the advanced rotation occurs when the wing just begins to rotate after the initial surge-like motion is completed.

Changing the rotational phase during slow rotation results in distinct changes in how the flow field evolves, and the aerodynamic forces generated.

## 4.5 Potential applications

The current study could find potential applications in designing advanced flow control surfaces and kinematic controls in order to enhance the hover performance of mechanical devices. The variations in forces and the correlation with kinematics and flow fields for changes in rotational phases, especially in slow rotation, can prove valuable for the flight scenarios where different maneuvers are required. For example, if a certain flight envelope required large lift and less drag, the symmetric, slow rotation can be chosen as it is a reasonable trade-off. The maximum lift produced is lower than the advanced rotations but the maximum drag is

## Chapter 4. Summary and conclusions

---

the small in symmetric rotation. To enhance the performance during a symmetric rotation, the rotational duration can be decreased, to produce higher lift overall, and low drag at the beginning of the stroke. If delaying the occurrence of maximum lift in a stroke was the goal, a fully delayed rotation would be the optimal solution. Several similar kinematic configurations for mechanical flapping flight can be deduced based on the data presented in this study.

On the other hand, the extensive discussion on the flow stages of the hovering cycle is intended to shed light on the relevant topological characteristics that are found during a normal hovering cycle that assist in manipulation of the flow. For example, in the fully delayed rotation, multiple strong but small LEVs emerge at the end of the cycle that are quickly shed into the wake. An appropriate flow control device could be devised to keep the LEVs closer to the wing, thus enhancing lift even at the end of the stroke. This way the favourable  $\alpha$  at the end of the cycle in the delayed rotations can be utilised to its full potential. The LEV -lift off in the symmetric rotation occurs at maximum stroke velocity. Perhaps, this can be prolonged with appropriate flow control techniques, thus keeping the LEV bound to the wing. Recently, a study showed the importance of trailing edge vortices in insect flight [8]. Perhaps, the multiple mesmerising TEVs shed in the fully advanced rotation in this study can be leveraged using additional surfaces at the trailing edge.

## A Force rotation matrix

The reference frame for the force sensor was aligned to the lab frame prior to the experiment. As the wing moved in the fluid, the force sensor rotated with the wing. To calculate the lift and drag, the forces obtained from the sensor had to be rotated and the weight of the wing in each frame had to be deducted. This section gives details about the rotation matrix for the forces.

Before beginning every single measurement, the fluid in the tank was allowed to reach a quiescent state. The force acting on the sensor at this stage was the sum of the weight of the wing, wing holder and fluid around the apparatus. This weight is denoted by  $W$  acts downwards (figure A.1). This bias was removed before beginning the measurements in order to capture only the aerodynamic forces. However, since the force sensor rotated with the wing during measurements, the weight of the wing at angles other than  $\beta = 0^\circ$  had to be subtracted from the measured forces along with the initially adjusted weight. For the symmetric rotation case, the wing is vertical at the start of the stroke as depicted by the gray rectangle in figure A.1(a). The y axis of the force sensor aligns with the vertical angle. And the x axis is horizontal to the right as shown in the figure. The forces measured in x and y directions are  $F_{x_0}$  and  $F_{y_0}$  respectively. The weight component in the y direction are  $W_{y_0} = W$  as indicated (figure A.1(a)). In this case, there is no horizontal weight component. However, for advanced and delayed rotation cases, the pitch angle of the wing at the start of the stroke is at an angle  $\beta_0$  from the vertical. This can be calculated based on the phase-shift,  $\Delta t_s$ . This shifts the orientation of the starting forces at rest ( $F_{x_0}, F_{y_0}$ ) as indicated on the black rectangle, which have to be resolved taking the weights into account ( $W_{x_0}, W_{y_0}$ ).

Following this, the weight of the wing at every pitch angle is removed, taking into account that the weight of the wing at the starting angle was also removed. The weight of the wing is found to be  $W = 10.5 \text{ g} = 0.11 \text{ N}$ .

Resolving the weight of the wing at an angle  $\beta_0$  that we have zeroed before the start of the experiments, we get -

## Appendix A. Force rotation matrix

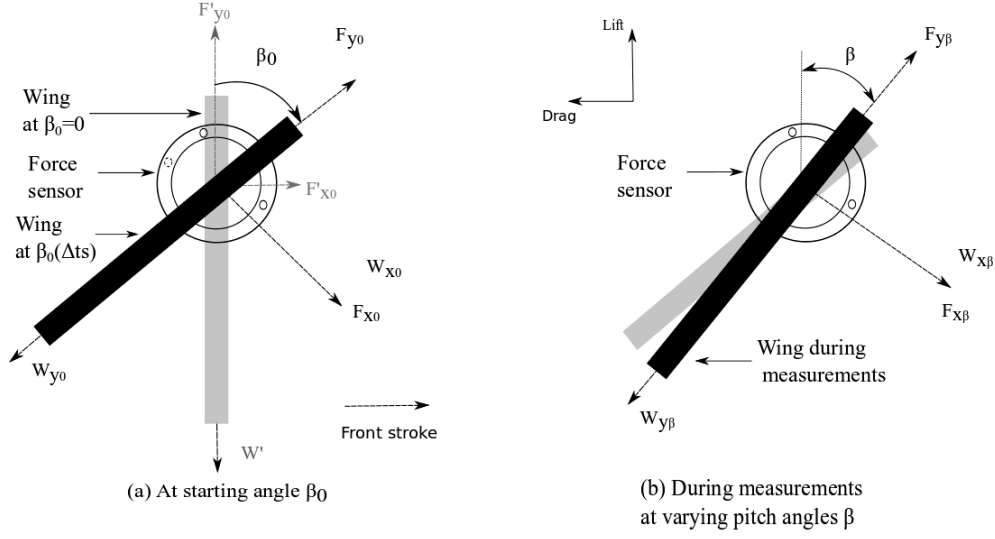


Figure A.1 – Resolution of forces

$$W_{y0} = -W * \cos\beta_0 \quad (A.1)$$

$$W_{x0} = W * \sin\beta_0 \quad (A.2)$$

Similarly, the orientation of forces when the wing makes an angle  $\beta$  with the vertical, during the wing motion in the experiment, is shown in figure A.1(b).  $F_{y\beta}$  and  $F_{x\beta}$  are the instantaneous forces measured in y and x directions during the flapping cycle which includes a part of the weight of the wing at every angle  $\beta$ . The weight components corresponding to the pitch angle  $\beta$  are  $W_{y\beta}$  and  $W_{x\beta}$  in y and x directions. Resolving the weight at this angle, we get-

$$W_{y\beta} = -W * \cos\beta \quad (A.3)$$

$$W_{x\beta} = W * \sin\beta \quad (A.4)$$

But the actual weight acting on the sensor because of the earlier zeroing of the forces at  $\beta_0$  is given by  $W_{\beta}$ -

$$W_{y\beta'} = -W * \cos\beta + W * \cos\beta_0 \quad (A.5)$$

$$W_{x\beta'} = W * \sin\beta - W * \sin\beta_0 \quad (A.6)$$



---

To get only the aerodynamic forces acting on the sensor at  $\beta$ , this calculated weight :  $W_{x_{\beta'}}$  and  $W_{y_{\beta'}}$ , has to be subtracted from the instantaneous force measured -

$$Fy1 = F_{y_{\beta}} - W_{y_{\beta'}} = F_{y_{\beta}} + W * \cos\beta - W * \cos\beta_0 \quad (A.7)$$

$$Fx1 = F_{x_{\beta}} - W_{x_{\beta'}} = F_{x_{\beta}} - W * \sin\beta + W * \sin\beta_0 \quad (A.8)$$

Lift  $L$ , and drag  $D$  act vertically and horizontally as shown in figure A.1. For a given angle  $\beta$ , the lift and drag can be resolved as-

$$L = Fy1 * \cos\beta - Fx1 * \sin\beta \quad (A.9)$$

$$D = Fy1 * \sin\beta + Fx1 * \cos\beta \quad (A.10)$$

The lift and drag curves presented in the sections 3.2, 3.3, and 3.4 are corrected as above.



## B Circulation sensitivity analysis

Circulation is computed to show the strength of the LEV. There is no clear definition of the region that should be used to determine the correct area for all circulation calculations. Therefore, a sensitivity analysis is conducted. In this study, a threshold of 20% of the maximum vorticity is considered. The computation of the circulation as a function of maximum percentage vorticity taken as the threshold is indicated in figure B.1. This is done for the flow field at  $t/T = 0.04$ , as this frame is at the beginning of the stroke where the vorticity just starts to accumulate and the remnant vorticity from the previous stroke is visibly spread. For a vorticity threshold of less than 20%, the circulation increases rather steeply, mostly due to the trailing edge vorticity that remains from the previous stroke. For a threshold more than 20%, the difference in circulation with respect to the baseline threshold is lower and becomes relatively constant. Therefore, a 20% vorticity threshold is used for calculating the circulation.

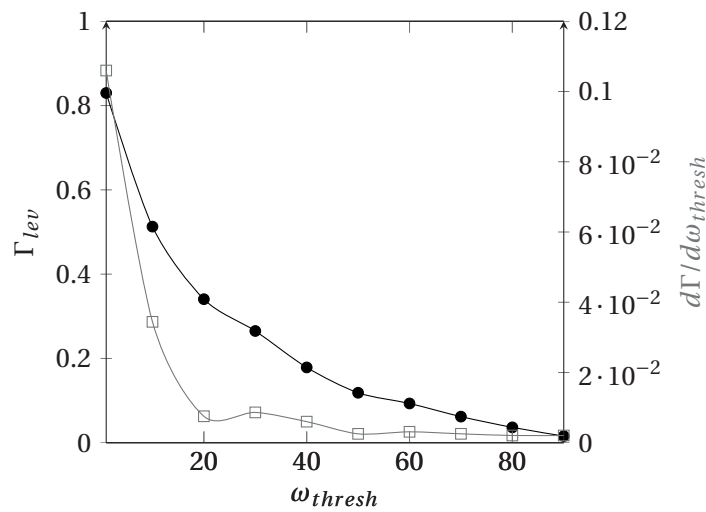


Figure B.1 – Circulation sensitivity analysis



# Bibliography

- [1] Salman a. Ansari, Kevin Knowles, and Rafal Zbikowski. Insectlike Flapping Wings in the Hover Part II: Effect of Wing Geometry. *Journal of Aircraft*, 45(6):1976–1990, nov 2008.
- [2] Salman a. Ansari, Nathan Phillips, Graham Stabler, Peter C Wilkins, Rafał Żbikowski, and Kevin Knowles. Experimental investigation of some aspects of insect-like flapping flight aerodynamics for application to micro air vehicles. *Exp. Fluids*, 46(5):777–798, apr 2009.
- [3] L Bennett. Clap and fling aerodynamics - experimental evaluation. *Journal of Experimental Biology*, 69(AUG):261–272, 1977.
- [4] Leon Bennett. Insect Flight : Lift and Rate of Change of Incidence. *Science*, 167(3915):177–179, 1970.
- [5] J. M. Birch. The influence of wing-wake interactions on the production of aerodynamic forces in flapping flight. *Journal of Experimental Biology*, 206(13):2257–2272, 2003.
- [6] James M Birch, William B Dickson, and Michael H Dickinson. Force production and flow structure of the leading edge vortex on flapping wings at high and low Reynolds numbers. *The Journal of experimental biology*, 207(Pt 7):1063–1072, 2004.
- [7] Richard J Bomphrey, Nicholas J Lawson, Nicholas J Harding, Graham K Taylor, and Adrian L R Thomas. The aerodynamics of *Manduca sexta*: digital particle image velocimetry analysis of the leading-edge vortex. *The Journal of experimental biology*, 208(Pt 6):1079–94, 2005.
- [8] Richard J. Bomphrey, Toshiyuki Nakata, Nathan Phillips, and Simon M. Walker. Smart wing rotation and trailing-edge vortices enable high frequency mosquito flight. *Nature*, 2017.
- [9] E.M. Bos, D. Lentink, B.W. Van Oudheusden, and H. Bijl. Influence of wing kinematics on performance in hovering insect flight. *Journal of Biomechanics*, 39:S358, 2006.
- [10] James H. J. Buchholz, Melissa a. Green, and Alexander J. Smits. Scaling the circulation shed by a pitching panel. *Journal of Fluid Mechanics*, 688:591–601, 2011.

## Bibliography

---

- [11] James H. J. Buchholz and Alexander J. Smits. On the evolution of the wake structure produced by a low-aspect-ratio pitching panel. *Journal of Fluid Mechanics*, 546(-1):433, dec 2005.
- [12] N A Buchmann, C Willert, and J Soria. Tomographic particle image velocimetry using pulsed, high power LED volume illumination 9th Int. *9th International symposium on particle image velocimetry PIV11, Japan.*, Ill, 2011.
- [13] Abel-john Buchner, Nicolas Buchmann, Kareem Kilany, Callum Atkinson, and Julio Soria. Stereoscopic and tomographic PIV of a pitching plate. *Experiments in Fluids*, 52(2):299–314, nov 2011.
- [14] John O. Dabiri. Optimal Vortex Formation as a Unifying Principle in Biological Propulsion. *Annual Review of Fluid Mechanics*, 41(1):17–33, jan 2009.
- [15] M Dickinson. Effects of Wing Rotation on Unsteady Aerodynamic Performance At Low Reynolds Numbers. *The Journal of experimental biology*, 192(1):179–206, 1994.
- [16] M. H. Dickinson. Wing Rotation and the Aerodynamic Basis of Insect Flight. *Science*, 284(5422):1954–1960, 1999.
- [17] Michael H. Dickinson and Karl Götz. Unsteady aerodynamic performance of model wings at low reynolds numbers. *J. exp. Biol.*, 174:45–64, 1993.
- [18] R. Dudley and C. P. Ellington. Mechanics of forward flight in bumblebees. II. Quasi-steady lift and power requirements. *Journal of Experimental Biology*, 148(1):53–88, 1990.
- [19] Jeff D. Eldredge and Kwitae Chong. Fluid transport and coherent structures of translating and flapping wings. *Chaos*, 20(1), 2010.
- [20] C. P. Ellington. The Aerodynamics of Hovering Insect Flight. I. The Quasi-Steady Analysis. *Philosophical Transactions of the Royal Society B: Biological Sciences*, 305(1122):1–15, 1984.
- [21] C P Ellington. The Aerodynamics of Hovering Insect Flight. II. Morphological Parameters. *Philosophical Transactions of the Royal Society of London. B, Biological Sciences*, 305(1122):17 LP – 40, feb 1984.
- [22] C. P. Ellington. The Aerodynamics of Hovering Insect Flight. III. Kinematics. *Philosophical Transactions of the Royal Society B: Biological Sciences*, 305(February):41–78, 1984.
- [23] C. P. Ellington. The Aerodynamics of Hovering Insect Flight. IV. Aeorodynamic Mechanisms. *Philosophical Transactions of the Royal Society B: Biological Sciences*, 305(1122):79–113, 1984.
- [24] C P Ellington. The aerodynamics of hovering insect flight. V. A vortex theory. *Philosophical Transactions of the Royal Society of London. Series B, Biological Sciences*, 305(1122):115–144, 1984.

- 
- [25] C. P. Ellington. The Aerodynamics of Hovering Insect Flight. VI. Lift and Power Requirements. *Philosophical Transactions of the Royal Society B: Biological Sciences*, 305(1122):145–181, feb 1984.
- [26] Charles P Ellington, Coen van den Berg, Alexander P Willmott, and Adrian L. R. Thomas. Leading-edge vortices in insect flight. *Nature*, 384(6610):626–630, 1996.
- [27] A. Roland Ennos. The kinematics and aerodynamics of the Free Flight of some Diptera. *The Journal of Experimental Biology*, 142(1):49–85, 1989.
- [28] Ryan B George. *Design and Analysis of a Flapping Wing Mechanism for Optimization* - M.Sc. Masterthesis, Brigham Young University, 2011.
- [29] M Gharib, E Rambod, and K Shariff. A universal time scale for vortex ring formation. *Journal of Fluid Mechanics*, 360:121–140, 1998.
- [30] Laurent Graftieaux, Marc Michard, and Nathalie Grosjean. Combining PIV, POD and vortex identification algorithms for the study of unsteady turbulent swirling flows. *Measurement Science and Technology*, 12(9):1422–1429, 2001.
- [31] Kenneth O. Granlund, Michael V. Ol, and Luis P. Bernal. Unsteady pitching flat plates. *Journal of Fluid Mechanics*, 733:R5, 2013.
- [32] Melissa A Green. *Analysis of Bio-Inspired Propulsors*. PhD thesis, Princeton University, 2009.
- [33] Melissa a. Green, Clarence W. Rowley, and Alexander J. Smits. The unsteady three-dimensional wake produced by a trapezoidal pitching panel. *Journal of Fluid Mechanics*, 685:117–145, 2011.
- [34] Melissa a. GREEN and Alexander J. SMITS. Effects of three-dimensionality on thrust production by a pitching panel. *Journal of Fluid Mechanics*, 615:211, 2008.
- [35] G. Haller. An objective definition of a vortex. *Journal of Fluid Mechanics*, 525:1–26, 2005.
- [36] G. Haller and G. Yuan. Lagrangian coherent structures and mixing in two-dimensional turbulence. *Physica D: Nonlinear Phenomena*, 147(3-4):352–370, dec 2000.
- [37] George Haller and Themistoklis Sapsis. Lagrangian coherent structures and the smallest finite-time Lyapunov exponent. *Chaos*, 21(2):1–7, 2011.
- [38] Elliot W Hawkes and David Lentink. Fruit fly scale robots can hover longer with flapping wings than with spinning wings. *Journal of the Royal Society Interface*, 13:20160730, 2016.
- [39] E. G. Hernandez-Martinez, G. Fernandez-Anaya, E. D. Ferreira, J. J. Flores-Godoy, and A. Lopez-Gonzalez. Trajectory Tracking of a Quadcopter UAV with Optimal Translational Control. *IFAC-PapersOnLine*, 48(19):226–231, 2015.

## Bibliography

---

- [40] Yangzi Huang and Melissa A. Green. Detection and tracking of vortex phenomena using Lagrangian coherent structures. *Experiments in Fluids*, 56(7):147, 2015.
- [41] Nanyaporn Intaratep, William N. Alexander, William J. Devenport, Sheryl M. Grace, and Amanda Dropkin. Experimental Study of Quadcopter Acoustics and Performance at Static Thrust Conditions. *22nd AIAA/CEAS Aeroacoustics Conference*, pages 1–14, 2016.
- [42] Ryan T. Jantzen, Kunihiro Taira, Kenneth O. Granlund, and Michael V. Ol. Vortex dynamics around pitching plates. *Physics of Fluids*, 26(5), 2014.
- [43] T. Jardin, Laurent David, and a. Farcy. Characterization of vortical structures and loads based on time-resolved PIV for asymmetric hovering flapping flight. *Animal Locomotion*, 46(1984):285–295, 2010.
- [44] Jinhee Jeong and Fazle Hussain. On the identification of a vortex. *Journal of Fluid Mechanics*, 285(-1):69, 1995.
- [45] D. F. Kurtulus, L. David, a. Farcy, and N. Alemdaroglu. Aerodynamic characteristics of flapping motion in hover. *Experiments in Fluids*, 44(1):23–36, 2008.
- [46] Fo Lehmann and M. The control of wing kinematics and flight forces in fruit flies (*Drosophila* spp.). *The Journal of experimental biology*, 201(3):385–401, 1998.
- [47] Fritz Olaf Lehmann. The mechanisms of lift enhancement in insect flight. *Naturwissenschaften*, 91(3):101–122, 2004.
- [48] Fritz-Olaf Lehmann and Simon Pick. The aerodynamic benefit of wing-wing interaction depends on stroke trajectory in flapping insect wings. *The Journal of experimental biology*, 208(Pt 16):3075–92, 2007.
- [49] David Lentink. *Exploring the Biofluidynamics of Swimming and Flight*. 2008.
- [50] H Liu, C Ellington, K Kawachi, and C. A computational fluid dynamic study of hawkmoth hovering. *The Journal of experimental biology*, 201 (Pt 4):461–77, 1998.
- [51] YanPeng Liu and Mao Sun. Wing kinematics measurement and aerodynamic force and moments computation of hovering hoverfly. In *Bioinformatics and Biomedical Engineering, 2007. ICBBE 2007. The 1st International Conference on*, number August 2006, pages 452–455, 2007.
- [52] T. Maxworthy. Experiments on the Weis-Fogh mechanism of lift generation by insects in hovering flight. Part 1. Dynamics of the ‘fling’. *Journal of Fluid Mechanics*, 93(01):47, 1979.
- [53] David B. Mayo and J. Gordon Leishman. Comparison of the Hovering Efficiency of Rotating Wing and Flapping Wing Micro Air Vehicles. *Journal of the American Helicopter Society*, 55(2), 2010.



- 
- [54] Karen Mulleners and Markus Raffel. The onset of dynamic stall revisited. *Experiments in Fluids*, 52(3):779–793, may 2012.
- [55] Karen Mulleners and Markus Raffel. Dynamic Stall Development. *Experiments in Fluids*, 54(2):1469, 2013.
- [56] Werner Nachtigall. *Insects in flight*. New York:McGraw-Hill, 1974.
- [57] R Ake Norberg. Hovering flight of the Dragonfly *Aeschna Juncea* L., Kinematics and Aerodynamics. *Swimming and Flying in Nature*, 2:763–764, 1975.
- [58] Cem a. Ozen and D. Rockwell. Three-dimensional vortex structure on a rotating wing. *Journal of Fluid Mechanics*, 707:541–550, 2012.
- [59] M. Percin and B. W. van Oudheusden. Three-dimensional flow structures and unsteady forces on pitching and surging revolving flat plates. *Exp Fluids*, page 56:47, 2015.
- [60] Simon Pick and Fritz Olaf Lehmann. Stereoscopic PIV on multiple color-coded light sheets and its application to axial flow in flapping robotic insect wings. *Experiments in Fluids*, 47(6):1009–1023, jun 2009.
- [61] C. Poelma, W. B. Dickson, and M. H. Dickinson. Time-resolved reconstruction of the full velocity field around a dynamically-scaled flapping wing. *Experiments in Fluids*, 41(2):213–225, jul 2006.
- [62] Ravi Ramamurti and William C Sandberg. A three-dimensional computational study of the aerodynamic mechanisms of insect flight. *The Journal of experimental biology*, 205(Pt 10):1507–1518, may 2002.
- [63] D. Rival and C. Tropea. Characteristics of Pitching and Plunging Airfoils Under Dynamic-Stall Conditions. *Journal of Aircraft*, 47(1):80–86, jan 2010.
- [64] David Rival, Tim Prangemeier, and Cameron Tropea. The influence of airfoil kinematics on the formation of leading-edge vortices in bio-inspired flight. *Experiments in Fluids*, 46(5):823–833, nov 2009.
- [65] David E. Rival, Jochen Kriegseis, Pascal Schaub, Alexander Widmann, and Cameron Tropea. Characteristic length scales for vortex detachment on plunging profiles with varying leading-edge geometry. *Experiments in Fluids*, 55(1):1–8, 2014.
- [66] Matthew P. Rockwood and Melissa A. Green. An Analysis of the Unsteady Wake Behind a Circular Cylinder using Lagrangian Coherent Structures. In *53rd AIAA Aerospace Sciences Meeting*, number January, pages 1–9, 2015.
- [67] Matthew P. Rockwood, Kunihiro Taira, and Melissa A. Green. Detecting Vortex Formation and Shedding in Cylinder Wakes Using Lagrangian Coherent Structures. *AIAA Journal*, 55(1):15–23, 2017.

## Bibliography

---

- [68] Filip Sadlo, Alessandro Rigazzi, and Ronald Peikert. Topological Methods in Data Analysis and Visualization. *Topological Methods in Data Analysis and Visualization Mathematics and Visualization, 2011, 151-165, DOI: 10.1007/978-3-642-15014-2\_13*, pages 151–165, 2011.
- [69] S P Sane and M H Dickinson. The control of flight force by a flapping wing: lift and drag production. *The Journal of Experimental Biology*, 204(204):2607–2626, 2001.
- [70] Sanjay P Sane and Michael H Dickinson. The aerodynamic effects of wing rotation and a revised quasi-steady model of flapping flight. *The Journal of experimental biology*, 205(Pt 8):1087–1096, apr 2002.
- [71] Sb Savage. The role of vortices and unsteady effects during the hovering flight of dragonflies. *The Journal of experimental biology*, pages 59–77, 1979.
- [72] Shawn C. Shadden, John O. Dabiri, and Jerrold E. Marsden. Lagrangian analysis of fluid transport in empirical vortex ring flows. *Physics of Fluids*, 18(4):1–11, 2006.
- [73] W. Shyy, H. Aono, S. K. Chimakurthi, P. Trizila, C. K. Kang, C. E S Cesnik, and H. Liu. Recent progress in flapping wing aerodynamics and aeroelasticity. *Progress in Aerospace Sciences*, 46(7):284–327, 2010.
- [74] R B Srygley and a L R Thomas. Unconventional lift-generating mechanisms in free-flying butterflies. *Nature*, 420(6916):660–664, 2002.
- [75] Mao Sun and Jian Tang. Unsteady aerodynamic force generation by a model fruit fly wing in flapping motion. *The Journal of experimental biology*, 205(Pt 1):55–70, 2002.
- [76] Graham K Taylor, Robert L Nudds, Adrian L R Thomas, Alexander Widmann, and Cameron Tropea. Flying and swimming animals cruise at a Strouhal number tuned for high power efficiency. *Letters To Nature*, 425:707–711, 2003.
- [77] Martin Jensen T.Wei-Fogh, T Weis-Fogh, and M Jensen. Biology and Physics of Locust Flight. I. Basic Principles in In-sect Flight. A Critical Review. *Philosophical Transactions of the Royal Society B Biological Sciences*, 239(667):415–458, 1965.
- [78] C VandenBerg and C P Ellington. The vortex wake of a ‘hovering’ model hawkmoth. *Philosophical Transactions of the Royal Society of London Series B-Biological Sciences*, 352(1351):317–328, 1997.
- [79] K. D. Von Ellenrieder, K. Parker, and J. Soria. Flow structures behind a heaving and pitching finite-span wing. *Journal of Fluid Mechanics*, 490:S0022112003005408, sep 2003.
- [80] Jeffrey a Walker. Rotational lift: something different or more of the same? *The Journal of experimental biology*, 205(Pt 24):3783–3792, 2002.

- [81] Simon M Walker, Adrian L R Thomas, and Graham K Taylor. Photogrammetric reconstruction of high-resolution surface topographies and deformable wing kinematics of tethered locusts and free-flying hoverflies. *Journal of the Royal Society, Interface / the Royal Society*, 6(33):351–66, apr 2009.
- [82] Z J Wang. Two dimensional mechanism for insect hovering. *Physical Review Letters*, 85(10):2216–2219, sep 2000.
- [83] Z. J. Wang. The role of drag in insect hovering. *Journal of Experimental Biology*, 207(23):4147–4155, 2004.
- [84] Z J Wang, J M Birch, and M H Dickinson. Unsteady forces and flows in low Reynolds number hovering flight: two-dimensional computations vs robotic wing experiments. *The Journal of Experimental Biology*, 207, 2004.
- [85] Z. Jane Wang. Vortex shedding and frequency selection in flapping flight. *Journal of Fluid Mechanics*, 410:323–341, 2000.
- [86] Z Jane Wang. Dissecting Insect Flight. *Annual Review of Fluid Mechanics*, 37(1):183–210, jan 2005.
- [87] Torkel Weis-fogh. Energetics of hovering flight in hummingbirds and in drosophila. *Journal of Experimental Biology*, 56:79–104, 1972.
- [88] Torkel Weis-fogh. Quick estimates of flight fitness in hovering animals, including novel mechanisms for lift production. *Journal of Experimental Biology*, 59:169–230, 1973.
- [89] C Willert, B Stasicki, J Klinner, and S Moessner. Pulsed operation of high-power light emitting diodes for imaging flow velocimetry. *Measurement Science and Technology*, 21(7):075402, jul 2010.
- [90] C. E. Willert and M. Gharib. Digital particle image velocimetry. *Experiments in Fluids*, 10(4):181–193, 1991.
- [91] L Zheng, T Hedrick, and R Mittal. A comparative study of the hovering efficiency of flapping and revolving wings. *Bioinspiration & biomimetics*, 8(3):036001, 2013.



# Swathi Krishna

---

## Education

- Oct 2012 – Dec 2017 **PhD (Fluid mechanics)**  
Lausanne, Switzerland *École polytechnique fédérale de Lausanne (EPFL).*  
title Unsteady fluid dynamics around a hovering flat plate wing  
supervisor Dr. Karen Mulleners, EPFL  
co-supervisor Dr. Melissa Green, Syracuse University
- Sep 2009 – July 2012 **MSc (Aerospace engineering)**  
Delft, Netherlands *Delft University of Technology.*  
title Characterisation of the flow field in circular subsonic impinging jets  
supervisor Prof. Dr. Fulvio Scarano
- Sep 2005 – July 2009 **BE (Mechanical engineering)**  
Bengaluru, India *Visvesvaraya Technological University.*  
title Design, fabrication, and test flight of a micro air vehicle  
supervisor Prof. S. Tryambaka Murthy

---

## Research experience

- Apr 2015 – Mar 2016 **Visiting researcher**  
New York, USA *Syracuse University.*  
Worked on the application of a lagrangian method to investigate the flow topology around a flapping wing
- Oct 2012 – Mar 2015 **Research associate**  
Hannover, Germany *Institute for Turbomachinery and Fluid Dynamics.*  
Conducted aerodynamic force measurements on an insect-like flapping wing along with particle image velocimetry
- Sep 2010 – Jan 2011 **Research intern**  
Arnhem, Netherlands *Microflow Technologies.*  
Worked on acoustic source localisation of transient signals from micro air vehicles using a particle velocity sensor (Microflow)
- Dec 2008 – May 2009 **Research intern**  
Bengaluru, India *Indian Institute of Science.*  
Worked on design, development and testing of a micro air vehicle

---

## Teaching experience

Spring 2013, 2014  
Hannover, Germany

### Teaching assistant

*Leibniz University of Hannover.*

Duties included tutoring, grading, preparation of assignments/exams for the course, fluid dynamics 2

Winter 2009  
Delft, Netherlands

### Student assistant

*Delft University of Technology.*

Duties included coordination, scheduling, assistance in experiments, and grading for low speed wind tunnel course

---

## Journal Publications

- 2017 Flow field and force evolution for a symmetric hovering flat plate wing, AIAA journal, submitted for review, June 27th
- 2017 Effect of rotational timing on the flow and forces around a hovering wing, in preparation

---

## International conference presentations

Nov 2016, Portland, USA

**Potential flow model predictions of a flapping wing in hover**  
*69<sup>th</sup> Annual meeting of American Physical Society.*

Jan 2016, San Diego, USA

**Effect of rotational phase on the flow topology of a flapping wing in hover**

*American Institute of Aeronautics and Astronautics, SciTech.*

Nov 2015, Boston, USA

**A Lagrangian approach to study the flow topology around a flapping wing in hover**

*68<sup>th</sup> Annual meeting of American Physical Society.*

Jul 2014, Lisbon, Portugal

**Effect of pitch rate variation on the evolution of the leading edge vortex**

*17th International symposium on applications of laser techniques to fluid mechanics.*

---

## Linguistic skills

English : full working proficiency, expert

Hindi, Kannada, Telugu : native, fluent

German : basic conversational, informal practice

